博士論文

The Electrochemical Transport Properties and Defect Chemistry of Methylammonium Lead Halide Perovskite Materials

（メチルアンモニウム鉛ハライド系ペロブスカイトの電気化学輸送特性と欠陥化学）

王 恺

Table of Contents

CHAPTER 1

Introduction

1.1 Research Background

1.1.1 Hybrid Perovskite Solar Cells

Organic-inorganic hybrid halide perovskite materials have recently draw extraordinary attentions as a promising photovoltaic materials benefit from the excellent photo-electrical properties, such as, high optical absorption coefficients, tunable band gaps, outstanding electrical transport properties as well as low fabrication cost, although the materials are facing stability issues when exposed to moisture atmosphere or solar radiation [1-3].

The hybrid halide perovskite was reported a 3.8% photo-electrical conversion efficiency (PCE) firstly acted as a sensitizer that replaced the dye pigment in dye sensitized solar cells (DSSC) [4]. The PCE has a significant increase to above 9% [5] when liquid electrolyte which contains redox couple in DSSC was replaced by a more stable solid state hole transport layer (e.g. 2,2',7,7'-Tetrakis [N,N-di (4-methoxyphenyl) amino]-9,9'-spirobifluorene, Spiro-OMeTAD). This breakthrough led to a new research upsurge of halide-perovskite-based solid-state solar cells, and recently, the conversion efficiency of above 21% has been achieved [6].

The most popular architecture of perovskite-based solar cells reported in the literature mesoscopic n-i-p structure mainly due to the strong absorption of incident light and effective charge collection [5, 7]. The schematic diagram of this architecture is shown in Fig. 1-1 (a), which consists of a transparent cathode (fluorine doped tin oxide, FTO), a thin compact ETM layer (TiO_2), a thick porous metal oxide (mp-TiO_2) that penetrates into perovskite, a perovskite capping layer, a hole conduct layer (spiro-MeOTAD), and a metal anode (Au). Later, a planar n-i-p structure without porous layer was developed (Fig 1-2 (b)), and the best efficiency achieved was 19.3% [8]. However, this structure might exhibit severe photocurrent density-voltage ($J-V$) hysteresis. The architectures described in Fig. 1-1 (c) and (d) could be fabrication by changing the deposition order,

and if HTM layer is deposited first, the device will form so-called inverted p-i-n structure. The HTM layer usually use conduct polymer (poly(3,4-ethylene dioxythiophene): poly(styrene sulfonic acid, PEDOT: PPS) or inorganic materials like NiO. The best efficiency of this device has been achieved 18.9% [9].

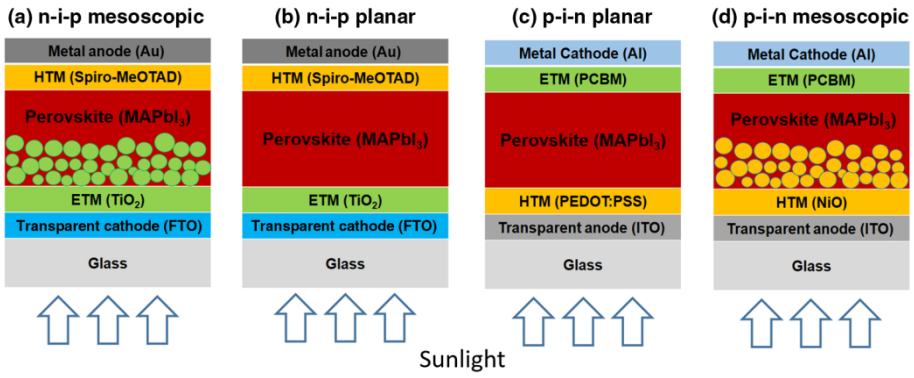

Fig. 1-1 Schematic diagrams of perovskite solar cells in the (a) n-i-p mesoscopic, (b) n-i-p planar, (c) p-i-n planar, and (d) p-i-n mesoscopic structures [10].

1.1.2 Crystal Structure of Hybrid Perovskites

The typical halide perovskite structure, ABX_3, is comprised of an extend framework of corner-sharing BX_6 octahedrons surrounding the center A-site, where A-site is occupied by monovalent organic cations, such as methylammonium ($CH_3NH_3^+$ or MA^+) and formamidinium ($NH_2CH{=}NH_2^+$ or FA^+), or inorganic alkali metal cation (Cs^+), and B-site is occupied by large divalent metal ion, such as Pb^{2+} Sn^{2+} and Ge^{2+}, while X-site is occupied by halogen anions or their mixtures which will significantly affect their chemical stability and photoelectrical properties. To form a high-symmetry cubic phase, the tolerance factor, t, should be close to 1 (in ideal condition), which can be expressed as,

$$t = \frac{r_A + r_X}{\sqrt{2}(r_B + r_X)}, \tag{1-1}$$

where r_A, r_B, and r_X are the ionic radii of the corresponding anions and cations. Large deviations of tolerance factor from 1 will cause severe distortion of crystal structure and form a low symmetry phase. In general, if t lies between 0.89 and 1, a cubic phase (α) is usually formed, and smaller t (<0.89) will lead to a low-symmetry tetragonal phase (β phase) or orthorhombic phase (γ phase) [11]. In general, as large Pb atom occupies B-site in hybrid perovskites, to satisfy $t\approx1$, the A-site ions must be extremely large.

Therefore, halide perovskites with organic A-sites that have relatively larger radii ($r(\mathrm{MA}^+)$ =0.18 nm [12] and $r(\mathrm{FA}^+)$ =0.19~0.22 nm [1]), compared with the inorganic groups (such as, $r(\mathrm{Cs}^+)$ =0.167 nm), can draw t close to 1 and can stabilize the perovskite structure [13]. Fig. 1-2 shows three typical crystal structures of halide perovskites, and calculated t of a series halide perovskites in the range of 0.8~1. It is worth noting that t is not the only predominant factor that determines the stability, for example, t will increase if Pb^{2+} is replaced by Sn^{2+}, but lead to relatively poor stability because Sn^{2+} can be easily oxidized to Sn^{4+} when exposed to ambient atmosphere [13].

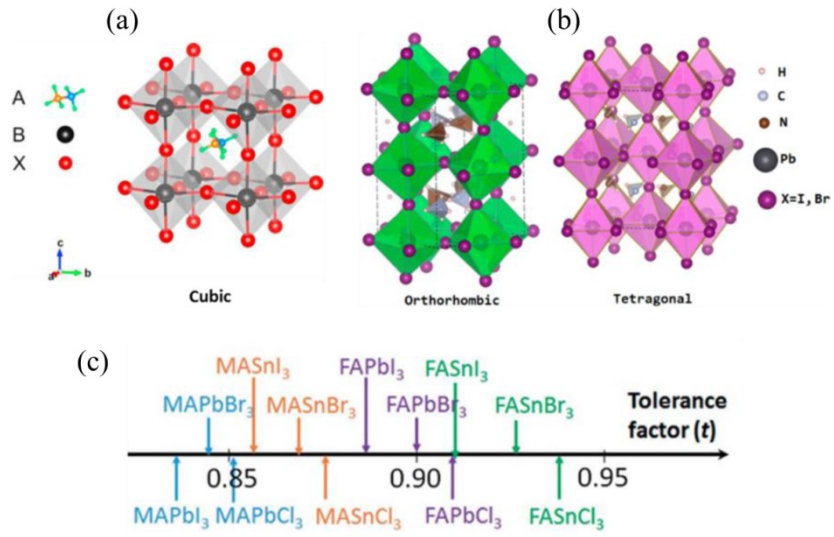

Fig. 1-2 (a) Crystal structure of cubic phase (α phase); (b) crystal structure of tetragonal phase (β phase) and orthorhombic phase (γ phase) of $MAPbX_3$ perovskites; (c) calculated tolerance factor of a series halide perovskites [11].

The halide perovskites undergoes reversible phase transitions with temperature. For $MAPbI_3$ materials, the phase transition of $MAPbI_3$ is driven by order-disorder transition of MA^+ ions [14-16]. Above 327 K~330 K, the MA^+ ions are randomly oriented thus the cubic phase with *pm*3*m* symmetry (α phase) is formed. In the temperature range of 161 K~327 K, the MA^+ ions become less disorder and form tetragonal *I*4/*mcm* symmetry (β phase). While below 161 K, the MA^+ ions are totally frozen thus form a low-symmetry orthorhombic phase (γ phase) with non-centrosymmetric $Pna2_1$ [17] or controsymmetric *Pnma* [14] symmetry. A similar phase transition in $FAPbI_3$ perovskites from hexagonal structure (δ phase) to trigonal structure (α phase) could also be

observed at about 125ºC [15], indicating higher stability of $FAPbI_3$ compared with $MAPbI_3$.

1.1.3 Electronic Structure

A wide range of approaches including both calculation and experimental methods have been used to investigate the electronic structure of the hybrid halide perovskites, which highly depends on the distortions of crystal lattice, such as the tilting of BX_6 octahedra. Density functional theory (DFT) is the favorite method to simulate band structures, band gaps, theoretical absorption spectra, carrier mobility as well as effective mass of electrons and holes.

Yin *et al*. [18, 19] reported the electronic structure of (pseudo)-cubic $MAPbI_3$ materials by DFT-GGA calculation, and showed the superior optical properties benefits from the unique intrinsic properties of the material including extremely high optical absorption, small effective masses of electrons and holes, and the shallow trap level by dominant ionic defects. The band structure of $MAPbI_3$, the total and partial DOS, as well as the transition energy levels of point defects and formation energies are shown in Fig. 1-3. $MAPbI_3$ exhibits a direct band gap of 1.5 eV at R point indicating a direct-gap *p-p* transition semiconductor of the material (Fig. 1-3 (a)). The conduction band minimum (CBM) of $MAPbI_3$ is mainly determined by Pb *p* orbital where coupling effect with I could be neglected, and the fully occupied Pb *s* orbital has strong antibonding coupling with I *p* orbital contributed to the valence band maximum (VBM) [18]. Furthermore, the strong *s-p* coupling enhance the dispersion of upper valence band (Fig. 1-3 (a)), and results in a small effective mass of holes which is comparable with the electron effective mass [19]. The calculated effective masses of electrons and holes are $0.35m_0$ and $0.31\ m_0$, respectively, with spin-orbit coupling (SOC) effects, and significantly decrease to $0.18m_0$ and $0.21\ m_0$ after SOC was taken into account [19]. A similar result reported by Giorgi *et al.* [20] suggested the effective masses of electrons and holes are $0.32m_0$ and $0.36\ m_0$, respectively, and decrease to $0.23m_0$ and $0.29\ m_0$ with SOC.

In hybrid perovskites, energy levels of defects have a strong influence on optical properties. Generally, shallow donors (or acceptors) are responsible for *n*-type (or *p*-type) doping, while defects with deep energy levels will act as non-radiative

recombination centers that significantly decrease the diffusion length of carriers. Fig. 1-3 (f) shows the energy levels of all the possible intrinsic point defects in $MAPbI_3$, and only shallow energy levels are formed from predominant point defects. While defects with very high formation energy, such as I atoms at MA sites (I_{MA}), I atoms at Pb sites (I_{Pb}), and Pb atoms at I sites (Pb_I) form deep energy levels.

Different from the common *p*-type solar-absorbers, $MAPbX_3$ perovskites can be tuned to *p*-type/*n*-type by controlling the chemical potentials of MAX and Pb source under different growth conditions [18, 19]. Stoumpos *et al*. [15] reported a simple carrier-type transformations in various perovskite compounds (including inorganic and organic/inorganic hybrid perovskites) depending on synthetic methods, and obtained *n*-type semiconductor from solution method, and *p*-type through solid state reactions in a controllable manner, which means the defect chemical properties could be modified by controlling the chemical potentials of each components.

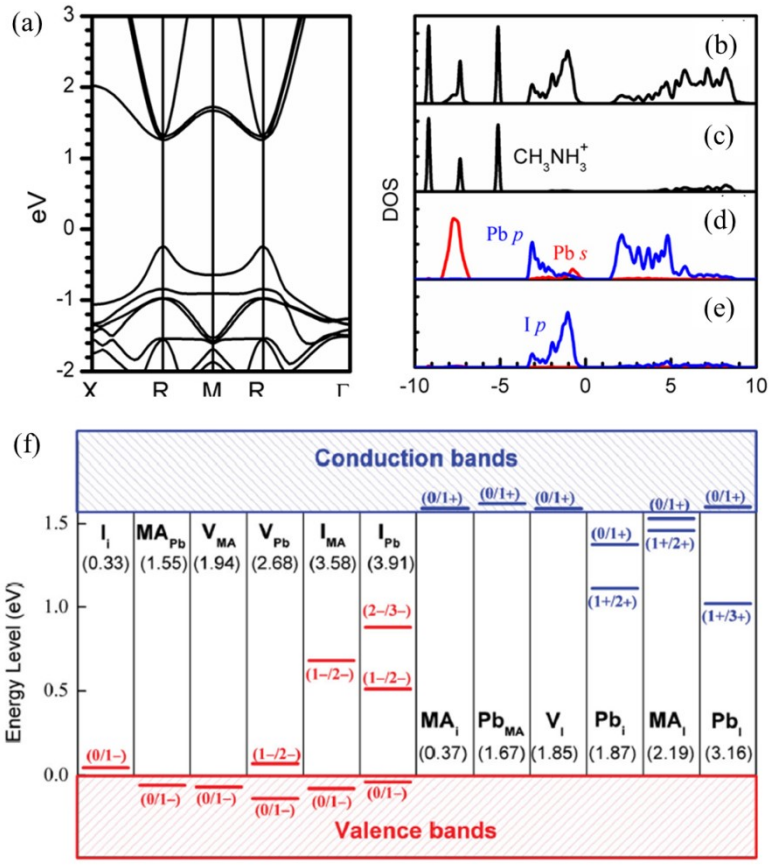

Fig. 1-3 (a) The band structure of $MAPbI_3$; (b) is the total DOS; (c) (d) and (e) are partial DOS of $CH_3NH_3^+$, Pb and I, respectively (the zero in DOS is referred to VBM);

(f) calculated transition energy levels and the formation energy (in parentheses) of point defects [18, 19].

1.1.4 Ionic Conduction

Diffusion of intrinsic ionic defects in hybrid pervoskite materials has important influence to the long-term stability and the comprehensive properties of perovskite-based solar cells. However, the ion migration behavior in these materials has not drawn strong attentions before the anomalous *J*−*V* hysteresis has been reported [21, 22]. Until now, there is still controversial about the exact nature of the mobile species and the transport mechanisms of ionic defects.

Dualeh *et al*. [23] investigated the impedance spectra of $MAPbI_3$ perovskites and suggested the materials might exhibit ionic transport in addition to electronic conduction. Eames *et al*. [24] reported that the ionic carriers transport mechanisms in $MAPbI_3$ perovskites, and showed the ions will migrate by hopping to neighboring positions. The schematic illustration of transport mechanisms in $MAPbI_3$ were shown in Fig. 1-4. Iodine ions exhibited a lower activation energy of 0.58 eV compared with MA^+ (0.84 eV) and Pb^{2+} (2.31 eV). The diffusion coefficient of I^- (10^{-12} cm^2/s) was estimated to be four orders of magnitude higher than MA^+ (10^{-16} cm^2/s) by assuming a Boltzmann-like barrier-hopping process, which suggested the diffusion of MA^+ is negligible [24].

More recently, Haruyama *et al*. [25] reported a comparable activation energy of I^- in both $MAPbI_3$ and $FAPbI_3$ of 0.45 eV consistent with that observed in pure ion-conducting materials. Azpiroz *et al*. [26] demonstrated that iodine vacancies (interstitials) might easily diffuse with the activation energy of 0.1 eV and should be the fast mobile species, meanwhile, the activation barriers for MA^+ and Pb^{2+} were suggested to be 0.46 eV and 0.80 eV, respectively. These results clearly exhibit that hybrid halide perovskites are mixed ionic/electronic conductors with halogen ions as the majority ionic carries.

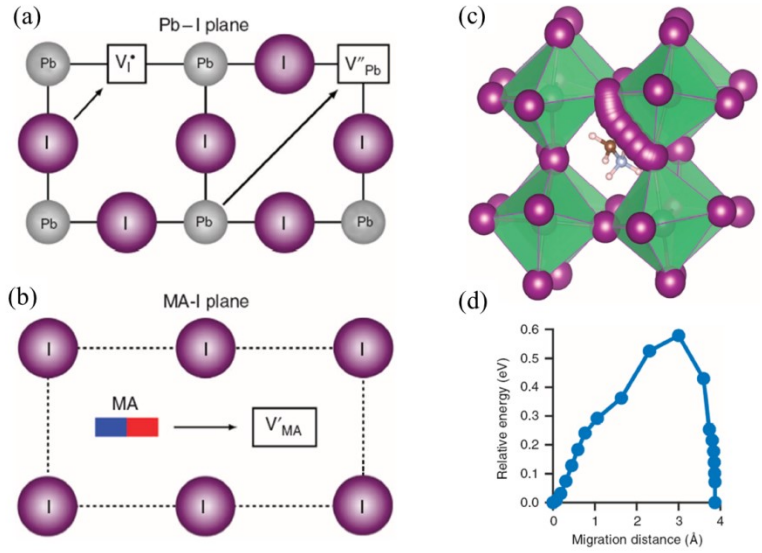

Fig. 1-4 Transport mechanisms in $MAPbI_3$ perovskite structure, (a) I^- migrates along octahedron edge, Pb^{2+} migrates along <110> direction; (b) MA^+ migrates into a neighbouring vacant A-site cage; (c) calculated migration path of I^-; (d) corresponding energy profile in (c) [24].

Considering full and partial Schottky disorder in $MAPbX_3$ materials, the defect equations could be expressed with Kröger-Vink notation,

$$\text{nil} \rightarrow V'_{MA} + V''_{Pb} + 3V^{\cdot}_{X} + MAPbX_3, \quad (1\text{-}1)$$

$$\text{nil} \rightarrow V'_{MA} + V^{\cdot}_{X} + MAX, \quad (1\text{-}2)$$

$$\text{nil} \rightarrow V''_{Pb} + 2V^{\cdot}_{X} + PbX_2. \quad (1\text{-}3)$$

Walsh *et al*. [27] calculated the defect formation energies of eq. (1-1) ~ (1-3) with 0.14 eV, 0.08 eV and 0.22 eV per defect, respectively, corresponding to a remarkable high equilibrium vacancy concentration of 0.4% at room temperature. This defect formation energy is significantly lower compared with inorganic halide perovskites, such as, $CsPbBr_3$ and $CsPbCl_3$, which exhibited formation energies above 2 eV [28, 29]. It is worth noting that these vacancy defects were suggested to form only shallow defect states, and will effectively inhibit the non-radiative recombination [27, 30]. Therefore, to modify the carrier density of hybrid perovksites by extrinsic doping is very difficult since carriers are heavily compensated by ionic defects in $MAPbX_3$ materials [31].

Several approaches have been reported that can be used to estimate the ionic conduction in $MAPbI_3$ materials. By DC polarization method with ion blocking electrode configuration, Yang *et al*. [32] reported a significant higher ionic conduction, σ_{ion} compared with electronic conduction, σ_e, as $\sigma_{ion} \approx 3\sigma_e$ in dark condition. Besides DC galvanostatic polarization, the contributions from σ_{ion} and σ_e can be determined by equilibrium *emf* measurements of an iodine concentration cell [33] as shown in Fig. 1-5 (a). The open circuit voltage (OCV) is measured to be close to full Nernst voltage ($t_{ion} \approx 1$) indicating the ionic conductivity is predominant when exposed to the atmosphere with relatively higher I_2 vapor pressure. Faradaic reaction cells, such as $\oplus\ Cu \mid MAPbI_3 \mid AgI \mid Ag\ \ominus$, can be used to identify the major mobile ionic species [32, 33]. By applying current for a given time, the formation of CuI at B interface (as shown in Fig. 1-5 (b)) could be observed, which excludes significant contributions from Pb^{2+} or MA^+ migration, however, since possible reactions at the interface of metal/$MAPbI_3$ have been neglected because of the instability of $MAPbI_3$ perovskites, this method might draw a rather vague conclusion compared with the former two methods.

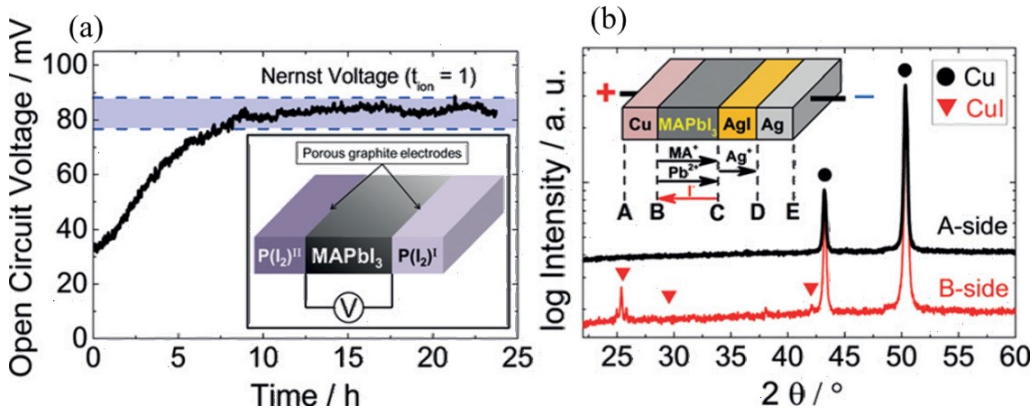

Fig. 1-5 (a) Equilibrium *emf* across a $MAPbI_3$ pellet with two faces exposed to different iodine partial pressures (1.7×10^{-7} bar and 1.5×10^{-5} bar) at 403 K, (b) XRD patterns of surfaces A and B of Cu foil, showing formation of CuI on B side [33].

In summary, both electrochemical analysis [23, 32-35] and theoretical calculations [23-26] conclude that the predominant charge carriers contributed to the bulk conduction of $MAPbI_3$ materials, at least under dark condition, is I vacancies, while MA vacancies are less mobile, which is also in well agreement with the newly reported ionic conductivity under the influence of iodine partial pressure by Kim *et al*. [36].

1.1.5 Thermodynamic Instability

The conversion efficiency of halide-hybrid-perovskite-based solar cells has rapidly increased to over 21% recent years, however, compared with the conventional photovoltaic materials, the major challenge obstructing the development of economic value is that the materials lack stability to external factors, such as, humility, oxygen, temperature and solar irradiation [37-38]. Zhao *et al*. [37] demonstrated several aspects of $MAPbI_3$ degradation in ambient atmosphere. In presence of H_2O/O_2, the $MAPbI_3$ will degrade into PbI_2 and MAI, and MAI will further decompose into CH_3NH_2 (aq) and HI (aq), and then HI (aq) will further react with O_2 to form I_2 (s) and H_2O (l). The decomposition proceeds by consuming HI, which gradually reduce the efficiency of solar cells. These degradation can be partially inhibited by using moisture-resistant hole transport layers, as reported by Niu *et al*. [38], a Al_2O_3 resistant layer was deposited to protect $MAPbI_3$ film from ambient atmosphere, which can effectively prevent the degradation of PCE.

For $MAPbI_3$ materials, the enthalpy change, ΔH_{d}, reported in the literature for the decomposition into MAI and PbI_2 secondary phase dispersed in a wide range. Yin *et al*. [18] reported a large ΔH_{d} of 0.27 eV/f.u., however, the overestimation of the value was speculated may because of the choosing of a hypothetical cubic phase instead of equilibrium tetragonal phase at RT [39]. And later, smaller values of ΔH_{d} have been suggested based on DFT calculation, such as -0.025 eV/f.u. by Agiorgousis *et al*. [40], -0.06 eV/f.u. by Zhang *et al*. [41], and -0.09 eV/f.u. by Ganose *et al*. [42]. The negative decomposition enthalpy indicated the intrinsic thermal instability of $MAPbI_3$ materials, thus, the decomposition will proceed spontaneously even in the absence of air, moisture, heat and solar irradiation.

More recently, Nagabhushana *et al*. [43] estimated the formation enthalpy, ΔH_{f}, of $MAPbX_3$ (X=I, Br and Cl) materials by direct calorimetric measurements, and found the value is 34.50±1.01, 6.69±1.41 and -9.03±0.68 KJ for $MAPbI_3$, $MAPbBr_3$, and $MAPbCl_3$, respectively. The thermodynamic stability of these materials decreases in the order $MAPbCl_3$, $MAPbBr_3$, and $MAPbI_3$, and this phenomenon provides a path to improve the thermodynamic stability of $MAPbI_3$ by substitutions, as shown in Fig. 1-6.

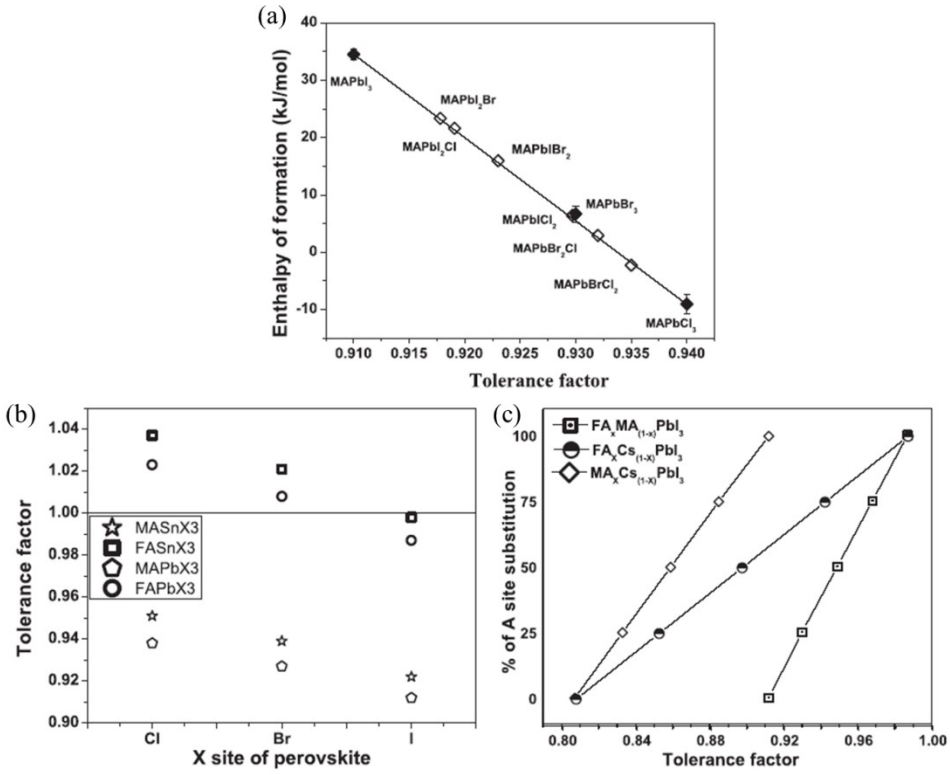

Fig. 1-6 (a) Linear fit of measured (filled symbols) and calculated (open symbols) enthalpy of formation vs. tolerance factor of $MAPbX_3$ materials; Tolerance factor as a function of (b) A-site and B-site substitution of MAPbX3, and (c) A-site substitution of $FAPbI_3$ [43].

The stability of $MAPbI_3$ can be significant improved by mixing with Br and I. I/Br mixing can maintain a high efficiency at Br content of 0.2, 0.29 [44]. I/Cl mixing was reported to exhibit remarkable stability to moisture, light and temperature [45]. Moreover, Br/Cl mixing also exhibit less sensitive to ambient atmosphere, and no obvious degradation was observed after exposed for 30 days [44, 46].

$MA_{(1-x)}FA_xI_3$ materials were reported to exhibit better long-term stability than $MAPbI_3$, which can function continuously for thousands of hours under illumination [45, 47, 48]. Considering B-site mixng in Fig. 1-6 (b), Pb^{2+} can be substituted by Sn^{2+}, however, since Sn^{2+} can be easily oxidized to Sn^{4+} when exposed to ambient atmosphere [15, 49], Sn-based perovskite is less promising for the application in photovoltaic device. Although the mechanism behind has not yet been fully understood,

the thermodynamic activity of halides might be significantly reduced by A-site, B-site, and anionic substitutions, thus, enhance the stability of perovskite materials.

1.2 Objectives and Experimental Methods

In present work, we investigated the electrochemical transport properties and defect chemistry of single crystalline $MAPbX_3$ hybrid perovskite materials, which exhibit ionic charge transport in addition to electronic conduction.

Firstly, high quality $MAPbBr_3$ and $MAPbI_3$ perovskite single crystals were prepared by solution-process technology. The thermal stability and total conductivities were characterized in both Ar and Ar/H_2 atmosphere, and based on these analysis we confirmed the effect of H_2 on different perovskite materials. To understand the defect chemistry of $MAPbX_3$ materials, both A/B ratio and X nonstoichiometry have to be controlled, which can be modified by compositional parameters of the materials. Based on the discussion on phase relations, $MAPbX_3$ material is a typical quaternary system, three chemical potentials of components, μ_{PbX_2}, μ_{H_2} and μ_{X_2} should be fixed to completely described the entire system.

Under the conditions as we mentioned above, the partial conductivities of electrons and holes of $MAPbX_3$ perovskite single crystals have been measured by Hebb-Wagner dc polarization with the variation of a_{X_2} using an asymmetric cell with an ion blocking electrode and reversible electrode, which can provide a fixed a_{X_2} during the polarization. In present work, we used two methods to measure the transference number of ions: 1) current interruption technique after the steady-state was attained during polarization; 2) *emf* measurement of the X_2 concentration cell controlled by the polarization of a X^- ion conductor under steady-state. An annealing method was used to modify a_{X_2} of single crystals under PbX_2-rich condition, and the total conductivities of these crystals were measured by ac impedance method. The total conductivity at a certain a_{X_2} could also be estimated by the cells with symmetric reversible electrodes with a fixed a_{X_2}, and the variation of the total conductivity could be observed during annealing at different temperatures due to the variation of a_{X_2} in perovskite materials.

The possible defect chemicstry model was discussed employing partial Schottky disorder with frozen vacancies of A-site and B-site and the presence of electron trapping

by X vacancies at low a_{X_2} domain. The band gap of $MAPbX_3$ was estimated from *p/n* switching point on partial conductivity curves, and compared with the band gap measured by UV-visible spectra, the data can used to confirm the existence of possible in-gap defect states. A p to n transition upon variation of a_{X_2} was observed during polarization, and also confirmed that the partial ionic conductivity is dominate in a wide range of stability domain, especially for $MAPbBr_3$ materials, which can be considered as a pure ionic conductor. Therefore, as an electrochemical system, its stability under bias voltage or photo-generated voltage is governed by the electrochemical window, which was estimated to be 1.36~1.46 V based on an approximation calculation of the thermodynamic properties of $MAPbBr_3$, a similar estimation in $MAPbI_3$ system is 0.90~0.95 V, leading to the stability domains of the system narrower than the intrinsic band gap.

The photo-induced charge-discharge curves of Au|$CH_3NH_3PbBr_3$|Pb cell was used to confirm the influence of ions migration on photo-electrochemical properties, based on the electronic band structure modification by photo-polarization.

Finally, prospect of $MAPbX_3$ perovskites used in novel photo-electrical conversion devices was discussed, such as photo-rechargeable capacitors and photo-intercalation devices, because of its good photoelectric properties combined with the significant ionic conduction. Some possible choices for devices designing were discussed and the simple working mechanisms of these devices were analyzed.

Present work will be helpful for understanding the defect chemistry and electrochemical transport of $MAPbX_3$ perovskite materials, and provide possible methods to regulate the concentration of electrons and defect vacancies, which could widen the applications of these materials for novel photo-electrochemical energy conversion devices.

1.3 Innovation of This Work

Although previous studies suggested the hybrid perovskites exhibit ionic charge transport in addition to electronic conduction, however, the details of partial conductivity of holes and electrons have never been established. It is because, to understand its defect chemistry, both A/B ratio and halogen nonstoichiometry have to

be controlled by regulating chemical potential of components, since the system is a quaternary one. Different from earlier reports, the electrochemical properties of single crystalline $MAPbX_3$ were examined by Hebb-Wagner DC polarization using a cell with asymmetric electrode configuration which can distinguish the electronic and ionic contributions, especially in the case when ions are dominant but electrons are just minority carriers. Based on Gibbs phase rule, three independent compositional parameters, the chemical potential of PbX_2, X_2 and H_2, were controlled to fix the state of entire system. During dc polarization, the A- and B-site vacancies were considered as "frozen" defects, and then partial electronic conductivity varied with X_2 activity could be measured under different applied voltages. Meanwhile, a current interruption technique was used to estimate the transference number of electronic charge carriers as a function of the chemical potential of X_2, μ_{X_2}. At the same time, we introduced a method to modify the carrier density and ionic defects concentration by annealing the single crystals in organic solutions with controllable chemical potentials of components.

A *p* to *n* transition was observed and a wide range of ionic dominant domain due to electrons trapping was confirmed by polarization. It is worth noting $MAPbBr_3$ materials is almost a pure electrochemical system since ions are majority carriers, different the prevailing opinion, the chemical stability under applied bias voltage or generated photo-voltage is governed by the electrochemical window rather than the band gap, which was estimated to be 1.36~1.46 V in $MAPbBr_3$ system and 0.90~0.95 V in $MAPbI_3$ system. The electrochemical window confirmed the stability domains of these systems are much narrower than the intrinsic band gap.

Present work will be helpful for a full understanding of the charge carrier chemistry and its transport properties in $MAPbX_3$ perovskites, which is an essential prerequisite for further investigation on the electrical behavior of the materials and more importantly, enhancement of the solar cells performance.

1.4. Reference

[1] Green MA, Ho-Baillie A. *et al*. The emergence of perovskite solar cells. *Nat. Photon.*, 8, 506–514 (2014).

[2] Snaith HJ. Perovskites: the emergence of a new era for low-cost, high-efficiency solar cells. *J. Phys. Chem. Lett*., 4, 3623-3630 (2013).

[3] Nazeeruddin MK, Snaith H. Methylammonium lead triiodide perovskite solar cells: A new paradigm in photovoltaics. *MRS Bull.*, 40, 641–645 (2015).

[4] Kojima A, Teshima K, Shirai Y, *et al*. Organometal halide perovskites as visible-light sensitizers for photovoltaic cells. *J. Am. Chem. Soc.*, 131(17): 6050-6051 (2009).

[5] Kim HS, Lee CR, Im JH, *et al*. Lead iodide perovskite sensitized all-solid-state submicron thin film mesoscopic solar cell with efficiency exceeding 9%. *Sci. Rep.*, 2: 591 (2012).

[6] Saliba M, Matsui T, Seo JY, *et al*. Cesium-containing triple cation perovskite solar cells: improved stability, reproducibility and high efficiency. *Energ. Environ. Sci.*, 9(6): 1989-1997 (2016).

[7] Heo JH, Im SH, Noh JH, *et al*. Efficient inorganic–organic hybrid heterojunction solar cells containing perovskite compound and polymeric hole conductors. *Nat. Photon.*, 7(6): 486 (2013).

[8] Zhou H, Chen Q, Li G, *et al*. Interface engineering of highly efficient perovskite solar cells. *Science*, 345(6196): 542-546 (2014).

[9] Dong Q, Yuan Y, Shao Y, *et al*. Abnormal crystal growth in $CH_3NH_3PbI_{3-x}Cl_x$ using a multi-cycle solution coating process. *Energ. Environ. Sci.*, 8(8): 2464-2470 (2015).

[10] Song Z, Watthage SC, Phillips AB, *et al*. Pathways toward high-performance perovskite solar cells: review of recent advances in organo-metal halide perovskites for photovoltaic applications. *J. Photon. Energ.*, 6(2): 022001 (2016).

[11] Elumalai NK, Mahmud MA, Wang D, *et al*. Perovskite solar cells: progress and advancements. *Energies*, 9(11): 861 (2016).

[12] McKinnon NK, Reeves DC, Akabas MH. 5-HT3 receptor ion size selectivity is a property of the transmembrane channel, not the cytoplasmic vestibule portals. *J. Gen.*

Physio., 138(4): 453-466 (2011).

[13] Fan Z, Sun K, Wang J. Perovskites for photovoltaics: a combined review of organic-inorganic halide perovskites and ferroelectric oxide perovskites. *J. Mater. Chem. A*, 3(37): 18809-18828 (2015).

[14] Baikie T, Fang Y, Kadro JM, *et al*. Synthesis and crystal chemistry of the hybrid perovskite $(CH_3NH_3)PbI_3$ for solid-state sensitized solar cell applications. *J. Mater. Chem. A,* 1(18): 5628-5641 (2013).

[15] Stoumpos CC, Malliakas CD, *et al*. Semiconducting tin and lead iodide perovskites with organic cations: phase transitions, high mobilities, and near-infrared photoluminescent properties. *Inorg. Chem.*, 52, 9019–9038 (2013).

[16] Kawamura Y, Mashiyama H, Hasebe K. Structural study on cubic-tetragonal transition of $CH_3NH_3PbI_3$. *J. Phys. Soc. Jpn.*, 71(7): 1694-1697 (2002).

[17] Poglitsch A, Weber D. Dynamic disorder in methylammoniumtrihalogenoplumbates (II) observed by millimeter-wave spectroscopy. *J. chem. Phys.* 87(11): 6373-6378 (1987).

[18] Yin W J, Shi T, Yan Y. Unusual defect physics in $CH_3NH_3PbI_3$ perovskite solar cell absorber. *Appl. Phys. Lett.,* 104(6): 063903 (2014).

[19] Yin W J, Shi T, Yan Y. Unique properties of halide perovskites as possible origins of the superior solar cell performance. *Adv. Mat.,* 26(27): 4653-4658 (2014).

[20] Giorgi G, Fujisawa J I, Segawa H, *et al*. Small photocarrier effective masses featuring ambipolar transport in methylammonium lead iodide perovskite: a density functional analysis. *J. Phys. Chem. Lett.* 4(24): 4213-4216 (2013).

[21] Unger EL, Hoke ET, Bailie CD, *et al*. Hysteresis and transient behavior in current–voltage measurements of hybrid-perovskite absorber solar cells. *Energ. Environ. Sci.,* 7(11): 3690-3698 (2014).

[22] Snaith HJ, Abate A, Ball JM, *et al*. Anomalous hysteresis in perovskite solar cells. *J. Phys. Chem. Lett.*, 5(9): 1511-1515 (2014).

[23] Dualeh A, Moehl T, Tétreault N, *et al*. Impedance spectroscopic analysis of lead iodide perovskite-sensitized solid-state solar cells. *ACS nano*, 8(1): 362-373 (2013).

[24] Eames C, Frost JM, *et al*. Ionic transport in hybrid lead iodide perovskite solar cells.

Nat. Commun., 6, 7497 (2015).

[25] Haruyama J, Sodeyama K, Han L, *et al*. First-principles study of ion diffusion in perovskite solar cell sensitizers. *J Am. Chem. Soc.*, 137(32): 10048-10051 (2015).

[26] Azpiroz JM, Mosconi E, Bisquert J, *et al*. Defect migration in methylammonium lead iodide and its role in perovskite solar cell operation. *Energ. Environ. Sci.*, 8(7): 2118-2127 (2015).

[27] Walsh A, Scanlon DO, Chen S, *et al*. Self-regulation mechanism for charged point defects in hybrid halide perovskites. *Angew. Chem. Int. Edit.*, 54(6): 1791-1794 (2015).

[28] Mizusaki J, Arai K, Fueki K. Ionic conduction of the perovskite-type halides. *Solid State Ionics*, 11(3): 203-211 (1983).

[29] Narayan RL, Sarma MVS, Suryanarayana SV. Ionic conductivity of $CsPbCl_3$ and $CsPbBr_3$. *J. Mater. Sci. Lett*., 6(1): 93-9 (1987).

[30] Kim J, Lee SH, Lee JH, *et al*. The role of intrinsic defects in methylammonium lead iodide perovskite. *J. Phys. Chem. Lett*., 5(8), 1312–1317 (2014).

[31] Gregori G, Yang TY, Senocrate A, *et al*. Ionic conductivity of organic-inorganic perovskites: relevance for long-time and low frequency behavior. Organic-Inorganic Halide Perovskite Photovoltaics. Springer, Cham, pp107-135 (2016).

[32] Yang TY, Gregori G, Pellet N, *et al*. The significance of ion conduction in a hybrid organic-inorganic lead-iodide-based perovskite photosensitizer. *Angew. Chem.*, 127(27): 8016-8021 (2015).

[33] Senocrate A, Moudrakovski I, Kim GY, *et al*. The nature of ion conduction in methylammonium lead iodide: a multimethod approach. *Angew. Chem.,* 129(27): 7863-7867 (2017).

[34] Yuan, Y, Wang, Q, Shao, Y, *et al*. Electric-field-driven reversible conversion between Methylammonium lead triiodide perovskites and lead iodide at elevated temperatures. *Adv. Energ. Mater.*, 6(2): 1501803 (2016).

[35] Yuan, Y, Chae, J, Shao, Y, *et al*. Photovoltaic switching mechanism in lateral structure hybrid perovskite solar cells. *Adv. Energ. Mater.*, 5(15): 1500615 (2015).

[36] Kim GY, Senocrate A, Yang TY, *et al*. Large tunable photoeffect on ion conduction in

halide perovskites and implications for photodecomposition. *Nat. mater.*, 17(5): 445 (2018).

[37] Zhao X, Park NG. Stability issues on perovskite solar cells. *Photonics*, 2(4): 1139-1151 (2015).

[38] Niu G, Li W, Meng F, *et al*. Study on the stability of $CH_3NH_3PbI_3$ films and the effect of post-modification by aluminum oxide in all-solid-state hybrid solar cells. *J. Mater. Chem. A*, 2(3): 705-710 (2014).

[39] Xiao Z, Meng W, Wang J, *et al*. Thermodynamic stability and defect chemistry of bismuth-based lead-free double perovskites. *ChemSusChem*, 9(18): 2628-2633 (2016).

[40] Agiorgousis ML, Sun YY, Zeng H, *et al*. Strong covalency-induced recombination centers in perovskite solar cell material $CH_3NH_3PbI_3$. *J. Am. Chem. Soc*., 136(41): 14570-14575 (2014).

[41] Zhang YY, Chen S, Xu P, *et al*. Intrinsic instability of the hybrid halide perovskite semiconductor $CH_3NH_3PbI_3$. *Chin. Phys. Lett*., 35(3): 036104 (2018).

[42] Ganose AM, Savory CN, Scanlon DO. $(CH_3NH_3)_2Pb(SCN)_2I_2$: a more stable structural motif for hybrid halide photovoltaics. *J. Phys. Chem. Lett.*, 6(22): 4594-4598 (2015).

[43] Nagabhushana GP, Shivaramaiah R, Navrotsky A. Direct calorimetric verification of thermodynamic instability of lead halide hybrid perovskites. *P. Natl. Acad. Sci.*, 113(28): 7717-7721 (2016).

[44] Noh JH, Im SH, *et al*. Chemical management for colorful, efficient, and stable inorganic–organic hybrid nanostructured solar cells. *Nano lett.*, 13, 1764-1769 (2013).

[45] Leijtens T, Eperon GE, Pathak S, *et al*. Overcoming ultraviolet light instability of sensitized TiO_2 with meso-superstructured organometal tri-halide perovskite solar cells. *Nat. commun*., 4: 2885 (2013).

[46] Lee MM, Teuscher J, Miyasaka T, *et al*. Efficient hybrid solar cells based on meso-superstructured organometal halide perovskites. *Science*, 1228604 (2012).

[47] Eperon GE, Stranks SD, Menelaou C, *et al*. Formamidinium lead trihalide: a broadly tunable perovskite for efficient planar heterojunction solar cells. *Energ. Environ, Sci*.,

7(3): 982-988 (2014).

[48] Burschka J, Pellet N, Moon SJ, *et al*. Sequential deposition as a route to high-performance perovskite-sensitized solar cells. *Nature*, 499(7458): 316 (2013).

[49] Hao F, Stoumpos CC, Chang RPH, *et al*. Anomalous band gap behavior in mixed Sn and Pb perovskites enables broadening of absorption spectrum in solar cells. *J Am. Chem. Soc.*, 136(22): 8094-8099 (2014).

CHAPTER 2

Synthesis and Characterization of $MAPbX_3$ Single Crystals

2.1 Introduction

Solution-processed methylammonium lead trihalide ($MAPbX_3$) hybrid perovskite solar cells have now achieved above 22% power conversion efficiencies, and urgent request for further improvements prompted our exploration of synthesis single crystal $MAPbX_3$ perovskites with large dimensions enough for the deposition of electrode and the practical characterization of electrical properties [1], however, the growth of high-quality single crystals is a time-consuming process. Past efforts suggested some solution-processed technologies for synthesis $MAPbX_3$ single crystals, including solvent evaporation crystallization, inverse temperature crystallization and anti-solvent vapor-assisted crystallization [2, 3]. The substantial decrease of $MAPbX_3$ solubility, in certain solvents, at elevated temperatures has been reported. This inverse solubility phenomenon can be used to crystallize $MAPbX_3$ crystals in hot solutions within a few minutes, and through balancing both temperature and concentration of precursors in organic solvent, the size and shape of crystals can be well controlled [2]. The diffusion of an appropriate anti-solvent into the crystal precursors in solutions will also lead to the growth of sizable crystals with high quality [3]. The single crystals prepared by solution-processed technology exhibit clear bulk transparency, smooth surface, large scale, crack-free, and also can be both size and shape controlled by manipulating different crystallization parameters [2, 3].

In this chapter, the fabrication of both $MAPbBr_3$ and $MAPbI_3$ single crystals with millimeter dimensions used solvent evaporation crystallization combined with inverse temperature crystallization. The solubility of $MAPbBr_3$ in *N*,*N*-Dimethylformamide (DMF) and $MAPbI_3$ in γ-Butyrolactone (GBL) at different temperatures have been confirmed by Saidaminov *et al*. [4] and was used to crystallize $MAPbX_3$ from hot solution, and then, carefully removed the crystal to a fresh solution of the precursors for further growth by slowly evaporating the solvent.

The phase purity of as-grown single crystals was characterized by X-ray diffraction patterns. Thermal stability was analysis by TG/DTA profiles in different gas

atmosphere. The phase stability at high temperature, especially the phase transition of $MAPbI_3$ from tetragonal to cubic at ~55° was also confirmed by high temperature XRD patterns. The total conductivities of perovksite single crystals were measured by ac impedance method with the variation of temperature. The phase relations and chemical stability of $MAPbBr_3$ and $MAPbI_3$ materials have been discussed, and compositional parameters that need to be controlled have been determined to fix the state of the entire system.

2.2 Experimental

2.2.1 Synthesis of $MAPbX_3$ Single Crystals

$MAPbBr_3$ and $MAPbI_3$ single crystals were prepared using solvent evaporation crystallization and inverse temperature crystallization method.

Purified lead bromide ($PbBr_2$, Tokyo Chemical Industry, Co., Ltd., 99%) (3.67g, 0.01mol) and methylammonium bromide (MABr, Tokyo Chemical Industry, Co., Ltd., >98%) (1.12g, 0.01mol) were dissolved in dry N, N-dimethylformamide (DMF, Wako Pure Chemical Industries, Ltd.) (10 mL) at room temperature by stirring until a clear liquid formed. And then the precursor was transferred to a reactor vessel. The vessel was settled in an oil bath with a constant temperature of 80°C. Since the solubility of $MAPbBr_3$ in DMF decreases significantly from 0.8 g/mL at RT to 0.3 g/mL 80°C [4], crystallization occurred in a very short time in hot solution. The new generated crystals were carefully removed and placed in a fresh solution with the precursor concentration of 1 mol/L for further growth with a constant temperature of 60°C, and the organic solvent was slowly evaporated for crystallization. Ar gas was used to remove organic gas from the vessel, and also avoid the possible degradation due to the contact with air atmosphere.

After a few days, the highly transparent crystals with orange color could be obtained with typical dimensions of 8 × 8 × 3 mm^3. The growth rate of crystals should be carefully controlled with evaporation temperatures, and rapid deposition may affect the quality of as-grown crystals. The shape of as-grown single crystals was changed with the geometry of the reactor vessel, and in present work, a depression on the surface of as-grown crystals was observed because of the curvature of the vessel bottom. The as-grown crystals were kept in a vacuum oven for a night to remove organic residue. With

carefully grinding and polishing, the visible defects on the surface (such as depression, micropores, microcracks, etc.) were removed, the then carefully cleaned with dichloromethane (CH_2Cl_2) solution.

To prepare $MAPbI_3$ single crystals, purified lead iodide (PbI_2, Tokyo Chemical Industry, Co., Ltd., 99.99%) (4.61g, 0.01mol) and methylammonium iodide (MAI, Tokyo Chemical Industry, Co., Ltd., >98%) (1.59g, 0.01mol) were dissolved in γ-butyrolactone (GBL, Wako Pure Chemical Industries, Ltd.) (10 mL) at 60 °C by stirring until formed a bright yellow liquid, and then transferred to a reactor vessel settled in an oil bath with a constant temperature of 110 °C. The solubility of $MAPbI_3$ in γ-butyrolactone reveals a maximum value of 1.15 g/mL at 60 °C and then significantly decreased to 0.55 g/mL at 110 °C [4]. This inverse solubility phenomenon was used to crystallize $MAPbI_3$ from the hot precursor solution rapidly. The new crystallized $MAPbI_3$ was carefully removed and placed in a fresh solution with the precursor concentration of 1 mol/L for further growth with a constant temperature of 110 °C. After a few days, the shiny crystals with black color could be obtained with typical dimensions of 9 × 9 × 2.5 mm^3, and the dimensions could be carefully controlled by changing the crystallization temperature. The as-grown crystals were kept in a vacuum oven for a night to remove organic residue.

It is worthwhile to note that after the crystal was removed from the hot solution to a fresh precursor solution for further grow, its surface would change into yellow in a short time if solvent residue was not removed. This phenomenon can be explained by the solubility curve reported by Saidaminov *et al*. [4]. The crystal is cooled down once taking out from the saturated solution at 110 °C, and the solution remained on the surface becomes unsaturated that will cause the dissolution of crystal surface, and the crystal surface may become roughened and less shiny. If the crystal is used as a new seed without proper treatment, the disintegrated surface would cause Russian-doll-like structure which has been reported by Liu *et al*. [5]. In order to eliminate the formation of this structure, the organic residue should be removed into a fresh solution immediately without any delay.

2.2.2 Characterization

Phase purity of $MAPbBr_3$ and $MAPbI_3$ samples were characterized by X-ray diffraction (XRD) using an X-ray diffractometer (RINT-UltimaIII, Rigaku Corp., Japan)

equipped with a Cu Kα X-ray tube working at 40 kV and 40 mA. The X-ray data was carried out from diffraction angles 10°~70° with the scan speed of 3°/min. In-situ XRD data was also collected as the temperature increased to the decomposition temperature of samples under the mixed gas atmosphere of 5% H_2 and 95% Ar (in volume percent). The materials were mounted on a quartz holder and measured within the diffraction angles from 10° to 70° with a scan speed of 3°/min. The temperature during the measurements was controlled using a programmable temperature controller (PTC-30, Rigaku, Japan), and the samples were hold at each temperature for 10 min before the measurement.

Simultaneous thermogravimetry and differential thermal analysis (TG/DTA, EXSTAR 6000, Hitachi Corp., Japan) was performed from RT to 700 °C with a heating rate of 5 °C/min. Both pure Ar gas and the mixed gas of 5% H_2 and 95% Ar (in volume percent) atmosphere were used for measurement in present experiment with a flow rate of 30 cc/min. Ar gas was used to protect the inner structure of the analyzer during the measurements.

The total conductivities of the single crystals was measured by ac impedance method using solarton 1255B frequency response analyzer (solarton Inc,, England) coupled with solarton 1296 dielectric interface (solarton Inc,, England) within the frequency range from 1 MHz to 0.1 Hz performed from 35°C to above 200°C. The experiment was conducted under pure Ar gas and the mixed gas of 5% H_2 and 95% Ar (in volume fraction) atmosphere.

The measurements above were conducted with several different single crystals under the same condition to guarantee the reproducibility of the results. The total conductivities were measured under dark condition.

2.3 Results and Discussion

2.3.1 Morphology of Single Crystals

The highly transparent $MAPbBr_3$ crystals exhibit orange color grown at 60 °C, and the morphology is shown in Fig. 2-1. The as-grown crystals have a typical dimension of $8 \times 8 \times 3$ mm^3 with smooth and crack-free surface (Fig. 2-1 (a)). Fig. 2-1 (b) shows a lamellar growth structure during crystallization. The surface of the as-grown crystals was etched by DMF solvent for 10 min, many pyramid-shape etch pits appeared on the

surface under optical microscope after etching (Fig. 2-1 (c)). The partial enlargement of the pyramid-shapes was shown in Fig. 2-1 (d), and the dimension of etch pits (0.15 mm) is related to the dislocation density on surface.

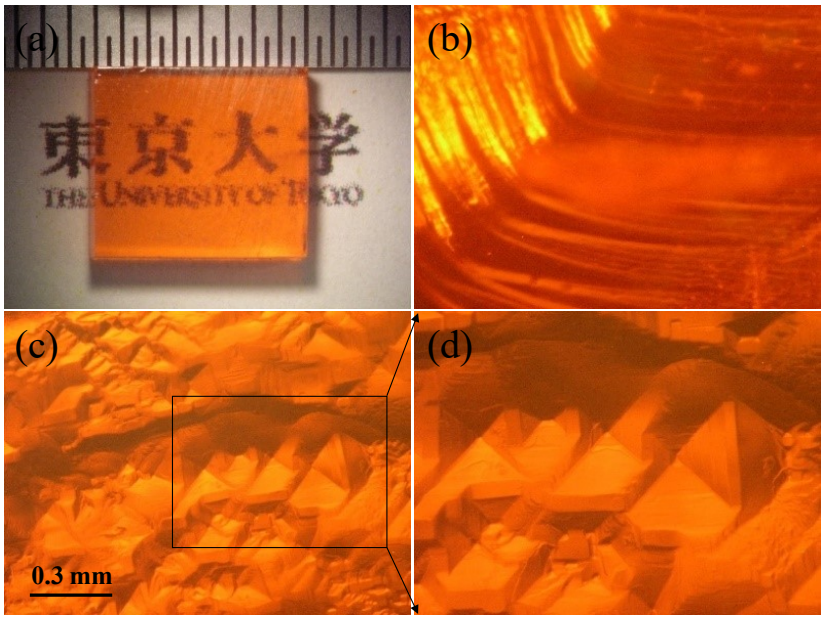

Fig. 2-1 Morphology of as-grown $MAPbBr_3$ perovskite single crystals

The as-grown $MAPbI_3$ single crystals generally formed as dodecahedra (Fig. 2-2 (a)), and some may exhibit rhombo-hexagonal dodecahedra consistent with a typical habit of body centered lattice (space group *I*4/*mcm*). The as-grown crystals were all black color but will gradually turn to yellowish when exposed to air atmosphere. The crystals have a typical dimension of 9 × 9 × 2.5 mm^3, and some samples may contains Russian-doll-like structure because of the mismatch between seed and new crystallization, and this layer should be carefully removed in order not to affect the following measurements. The surface of the as-grown crystals was etched by GBL solvent for 10 min at RT, etch pits with pyramid-shape could be observed under optical microscope after etching (Fig. 2-2 (b)), and the dimension of the etch pits was relatively smaller than $MAPbBr_3$ single crystals.

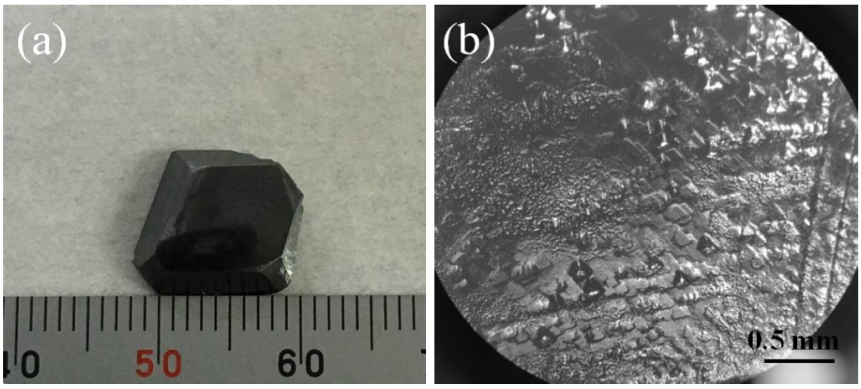

Fig. 2-2 Morphology of as-grown $MAPbI_3$ perovskite single crystals

2.3.2 Phase Purity and High Temperature Stability

The phase purity of samples was confirmed by X-ray diffraction patterns which show a cubic symmetry of $MAPbBr_3$ and a tetragonal symmetry of $MAPbI_3$ materials at room temperature.

As shown in Fig. 2-3, the XRD patterns of ground powder confirmed pure single-phase of cubic $MAPbBr_3$ perovskite, and the pattern of single crystals indicate only {001} diffraction peaks could be detected from the surface of the as-grown crystals. The corresponding lattice parameter was calculated to be 5.906 Å, which is consistent with the previously reported value by Sydney *et al*. [6].

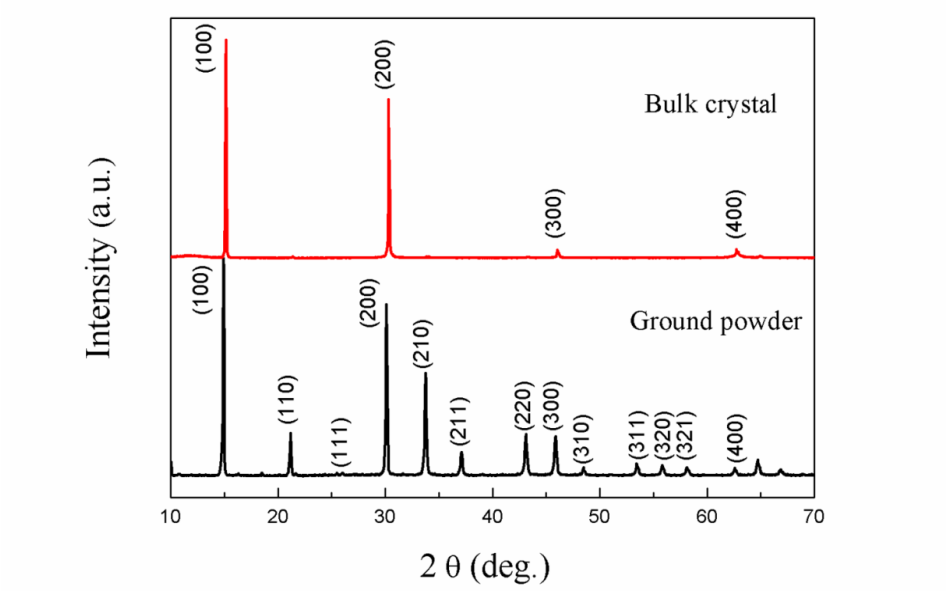

Fig. 2-3 The XRD patterns of $MAPbBr_3$ single crystals and ground powders.

$MAPbI_3$ single crystals have a tetragonal perovskite phase at room temperature as shown in Fig. 2-4, however, a phase transition from tetragonal to cubic phase has been reported at about 54°C~57°C. By monitoring the intensity of {211} and {213} reflections which can be separated from Bragg reflections expected in cubic symmetry, we could easily distinguish the tetragonal and cubic phase. The XRD pattern of ground powders indicates the presence of tetragonal symmetry, and the pattern of single crystalline $MAPbI_3$ confirmed only {211} diffraction peaks could be detected from the surface of as-grown crystals. The lattice parameter of $MAPbI_3$ materials at room temperature in tetragonal symmetry was calculated to be a_{tet}=8.868 Å, and c_{tet}=12.659 Å basically consistent with previous report [7].

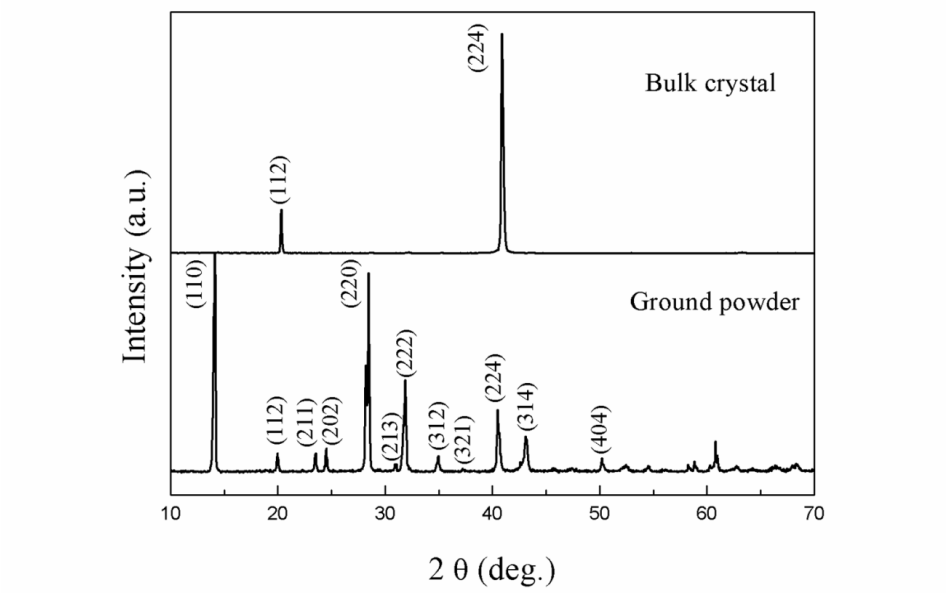

Fig. 2-4 The XRD patterns of $MAPbI_3$ single crystals and ground powders.

Phase stability at elevated temperatures of $MAPbBr_3$ and $MAPbI_3$ materials was investigated by high temperature X-ray diffraction measured in mixed atmosphere of 5% H_2 and 95% Ar (in volume fraction).

$MAPbBr_3$ materials maintained a cubic perovskite phase until the temperature up to 250°C, above that, the diffraction peaks corresponding to $PbBr_2$ was detected on XRD patterns as shown in Fig. 2-5. Compared with pure cubic perovskite phase, the pattern indicated the $MAPbBr_3$ perovskite materials start to undergo decomposition by gradually releasing CH_3NH_2 gas and HBr materials. The decomposition temperature is in good agreement with the results of TG/DTA measurements under the same gas

atmosphere (H_2/Ar), which exhibits no mass loss that could be detected until the temperature up to 240°C.

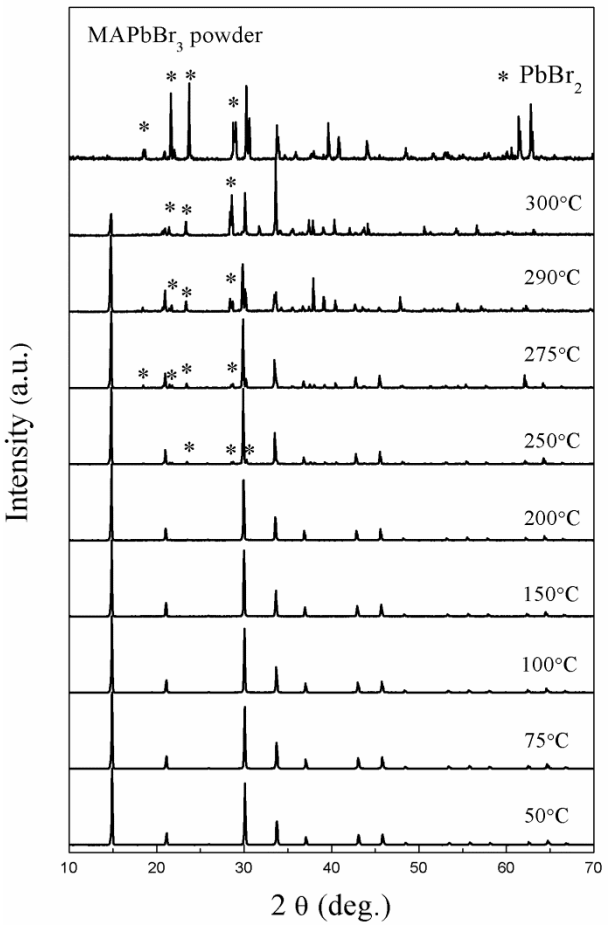

Fig. 2-5 High temperature XRD patterns of $MAPbBr_3$ powders

At high temperatures (≈54°C-57°C), the tetragonal phase of $MAPbI_3$ was reported to transform into cubic phase. To detect this transition, we focused on the diffraction peak of {211} and {213} reflections as they are sufficiently separated from Bragg reflections expected in cubic symmetry. Since the {211} reflection has a higher calculated intensity compared with {213} reflection, the change in symmetry would be detected more easily by monitoring this reflection. In the partial enlargement of {211} reflection within the diffraction angle 22°~26°, the intensity of {211} reflection significantly reduced by half compared with {202} reflection at 55°C, and totally disappeared at 75°C that means the complete phase transition from tetragonal to cubic. As the temperature increased, $MAPbI_3$ materials maintained cubic perovskite phase until 250°C, above which the diffraction patterns of PbI_2 gradually appeared. This temperature is relatively lower than

decomposition temperature of 265°C measured by TG/DTA in the mixed atmosphere of 5% H_2 and 95% Ar. The high temperature XRD patterns and the partial enlargement were shown in Fig. 2-6.

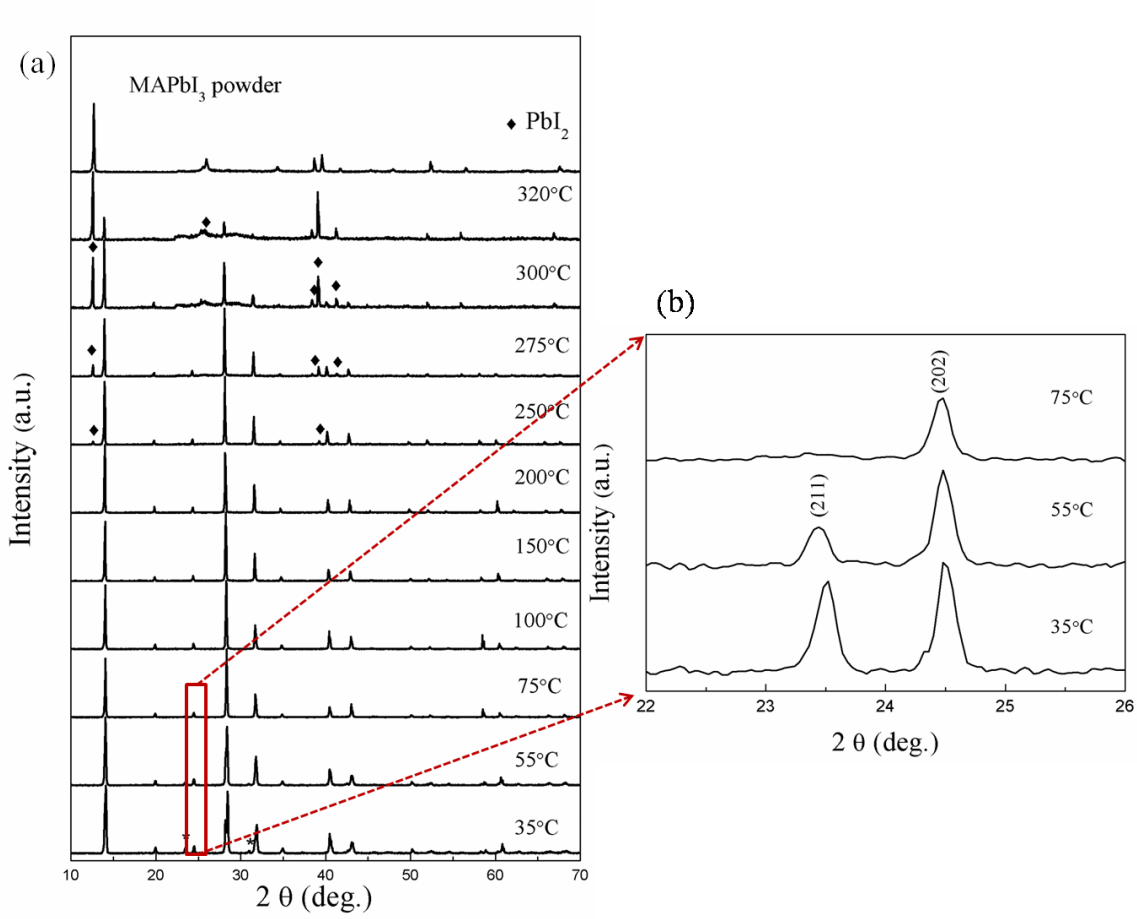

Fig. 2-6 The high temperature XRD patterns of $MAPbI_3$ materials (a), and the enlargement of 22°~26° diffraction angle which exhibits the variation of (211) reflection (b).

2.3.3 Thermal Stability

To investigate the thermal stability of the $MAPbBr_3$ and $MAPbI_3$ single crystal perovskites, TG/DTA measurements have been carried out in Ar atmosphere and the mixed atmosphere of 95% Ar and 5% H_2 as shown in Figs. 2-7 and 2-8.

The thermal profiles in Fig. 2-7 reveal a high thermal stability of as-grown $MAPbBr_3$ single crystals in both Ar and Ar/H_2 atmosphere, and almost no mass loss could be detected on TG curves below 240 °C, after which followed by a abrupt mass loss which corresponds to the decomposition of samples, and then rapidly evaporated above 400 °C.

Since the volatilization of MABr would cause approximately 23.4% weight loss which is in good agreement with the abrupt mass loss of 22.9% on TG profile measured in Ar atmosphere, and the decomposition be expressed with both type of reactions; chemical formation and defects formation expression,

$$CH_3NH_3PbBr_3(s) = CH_3NH_2(g) + HPbBr_3(s), \quad (2\text{-}1)$$

$$HPbBr_3(s) = HBr(g) + PbBr_2(s). \quad (2\text{-}2)$$

$$(CH_3NH_2 \cdot H)^{\times}_{MA} \rightarrow H^{\times}_{MA} + CH_3NH_2(g), \quad (2\text{-}3)$$

$$H^{\times}_{MA} + Br^{\times}_{Br} \rightarrow V'_{MA} + V^{\cdot}_{Br} + HBr(g). \quad (2\text{-}4)$$

Meanwhile, a significant endothermic peak at T ≈ 334°C was observed on DTA curve which can be related to the evaporation of methylamine and dehalogenation during the decomposition of $MAPbBr_3$. For the sample measured in Ar/H_2 atmosphere, the corresponding endothermic peak showed a slight increase to T ≈ 344°C which may be due to the reducing atmosphere that inhibits the decomposition of perovskites. It is worth noting that the mass loss of the first thermodynamic process measured in Ar/H_2 is 19.7% slightly smaller than that in Ar atmosphere. It may be because part of A-site vacancies, V'_{MA}, were occupied by proton that offset the mass loss, and the concentration of A-site vacancy in perovskite single crystals should be very significant in this case. The second endothermic peak at T ≈ 372°C was observed on DTA curve measured in Ar/H_2 was related to melting process of the newly generated $PbBr_2$ which exhibited almost no mass loss on TG curve. In addition, DTG curve also showed a significant peak representing the maximum mass loss rate during decomposition of $MAPbBr_3$ corresponding to the endothermic peak on DTA curves under different atmosphere. Above 400°C, the residual mass sharply decreased to 0% indicating the complete evaporation of $PbBr_2$, and in the same temperature range, mass loss rate gradually increased as shown on DTG curves.

The TG/DTA profiles of $MAPbI_3$ single crystals measured in the different atmospheres were shown in Fig. 2-8. In Ar atmosphere, there is no mass loss on TG curve below 230°C, and a slow reduction of 4.6% followed by an abrupt mass loss of 21.1% until the temperature up to 400°C. The decomposition can be expressed with both type of reactions: chemical formation and defect vacancies expression,

$$CH_3NH_3PbI_3(s) = CH_3NH_2(g) + HPbI_3(s), \quad (2\text{-}5)$$

$$2HI(g) = I_2(g) + H_2(g). \quad (2\text{-}6)$$

$$(CH_3NH_3 \cdot H)^{\times}_{MA} \rightarrow H^{\times}_{MA} + CH_3NH_2(g), \quad (2\text{-}7)$$

$$H_{MA}^{\times} + I_I^{\times} \rightarrow V'_{MA} + V_I^{\cdot} + HI(g). \quad (2\text{-}8)$$

The DTA curve exhibited two significant endothermic peak at T ≈ 353°C and T ≈ 398°C, which could be related to the volatilization of CH_3NH_2 gas with a mass loss of 5%, and the melting of PbI_2 after the decomposition of $MAPbI_3$ sample, respectively. The thermal behavior above has been confirmed by corresponding mass loss rate on DTG curve. The peak at T ≈ 353°C suggests the endothermic behavior is related to mass change, however, no peak at 398 °C could be detected, which indicates the second endothermic process is not accompanied by the mass change. Above the decomposition temperature, the residue mass of samples rapidly dropped, and was completely evaporated at 700°C. The $MAPbI_3$ shows higher thermal stability in Ar/H_2 atmosphere. There is no mass loss on TG curve below 265°C, and then showed an abrupt mass loss of 17.7 % which is significantly smaller than 25.3% measured in Ar atmosphere. The reduction in mass loss could be explained by enhancement of the thermal stability of intermediate $HPbI_3$ phase because of the presence of H_2 that restrains the decomposition reactions in eq. (2-6). Compared with $MAPbBr_3$ single crystals, $MAPbI_3$ materials suggest a relatively higher thermal stability, and the decomposition of $MAPbI_3$ is very sensitive to H_2 which could significantly improve the thermal stability of $MAPbI_3$ material at temperatures below the decomposition.

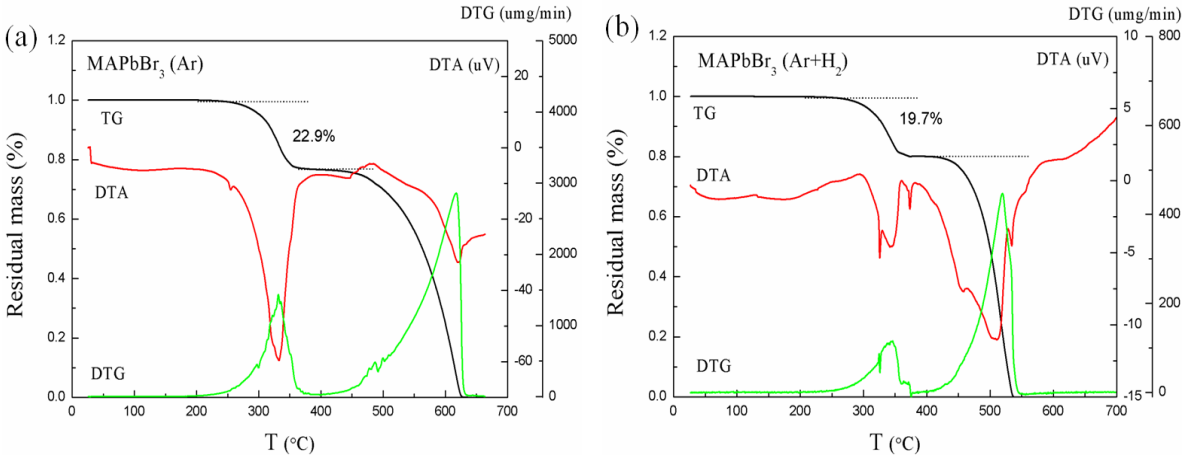

Fig. 2-7 The TG/DTA profiles of $MAPbBr_3$ single crystals measured in Ar atmosphere (a), and in 5% H_2 and 95% Ar atmosphere (b).

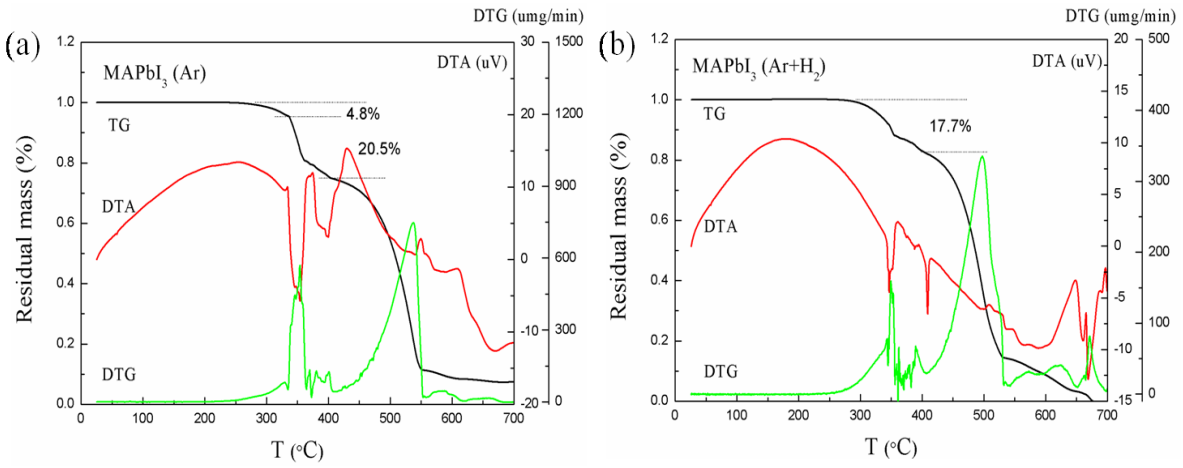

Fig. 2-8 The TG/DTA profiles of $MAPbI_3$ single crystals measured in Ar atmosphere (a), and in 5% H_2 and 95% Ar atmosphere (b).

2.3.4 Total Conductivities

The total conductivities of $MAPbBr_3$ and $MAPbI_3$ single crystals were measured by ac impedance method using ion blocking electrode (Au). The single crystals for measurements were gradually heated to 220°C for $MAPbBr_3$ and 180°C for $MAPbI_3$, after holding for a period, the samples were slowly cooled down to RT in Ar atmosphere (H_2/Ar atmosphere was used for $MAPbI_3$ on cooling). The total conductivities were calculated during the heat cycle, the Arrhenius plots were shown in Fig. 2-9.

In the plots of $\ln(\sigma T)$ against $1000/T$, the total conductivity curves on heating can be clearly distinguished into two regions, a straight line in low temperature range, and then gradually curved upward as the temperature increased. The transition might occur at relatively low temperature (below 100°C) for both $MAPbBr_3$ and $MAPbI_3$ materials. The total conductivity of $CsPbBr_3$ single crystals on heating was also measured for comparison. The bending occurred at ~130°C should due to the phase transition from tetragonal system to a cubic phase [8]. Similar to $MAPbX_3$, as the temperature increased, the conductivity curve exhibited a straight region followed by a sharp bending above 300°C as shown in Fig. 2-9.

The straight portion would represent as an extrinsic region, and the curved part should be the transition from extrinsic to intrinsic region. In the extrinsic region, the concentration of predominant ionic defects can be considered as constant corresponding

to a "frozen" state, and the activation energy for ion migration was determined by the slope of $\ln(\sigma T)$ against 1000/T. The activation energy of extrinsic region is 0.236 eV for $CsPbBr_3$, 0.135 eV for $MAPbBr_3$ and 0.132 eV for $MAPbI_3$ materials. In the intrinsic region, the apparent activation energy includes E_a as well as the enthalpy of vacancy defects formation, ΔH_S. The full Schottky disorder can be expressed in the following reaction using Kröger-Vink notation.

$$\text{nil} \rightarrow V'_{MA} + V''_{Pb} + 3V^{\cdot}_{X} + MAPbX_3, \quad (2\text{-}9)$$

where nil represents the perfect lattice of perovskite. And from this equation,

$$K_s = K_S^0 \exp\left(-\frac{\Delta H_S}{RT}\right) = [V'_{MA}][V''_{Pb}][V^{\cdot}_{X}]^3, \quad (2\text{-}10)$$

where K_S is the equilibrium constant and ΔH_S is the enthalpy change of eq. (2-9), K_S^0 is a constant. Since the number of lattice points maintains constant in $MAPbX_3$,

$$[V'_{MA}] = [V''_{Pb}] = 1/3[V^{\cdot}_{X}]. \quad (2\text{-}11)$$

Thus, Eq. (2-10) can be rewritten as,

$$[V^{\cdot}_{X}] = (9K_S^0)^{1/5} = K_S^0 \exp\left(-\frac{\Delta H_S}{5RT}\right). \quad (2\text{-}12)$$

The activation energy calculated from Arrhenius plot in the intrinsic region corresponds to $\Delta H_S/5 + E_a$.

At higher temperature range (above 175 ºC), because of the instability of $MAPbX_3$ materials, the following reaction might become major factor that govern the decomposition process,

$$(MA \cdot H)^{X}_{A} \rightarrow MA(g) + 1/2\, H_2(g) + V'_{MA} + h^{\cdot}. \quad (2\text{-}13)$$

If the perovskite structure can be maintained at high temperature, as the evaporation of CH_3NH_2 gas, the concentration of V'_{MA} increases, compensated by $h^{\cdot}$, leading to significant enhancement of the total conductivity of $MAPbBr_3$ and $MAPbI_3$ during cooling process. For $MAPbBr_3$ materials, the E_a on cooling process was estimated as 0.422 eV, much larger than the E_a of singlecrystalline $MAPbBr_3$ along [100] orientation (0.132 eV) [9], which should due to the holes conduction. For $MAPbI_3$ materials, the E_a on cooling process is 0.421 eV, comparable with the previous literature [10, 11], indicating there is no contribution from holes. It is because, the presence of H_2 will effectively inhibit the proceeding of eq. (2-13) since σ_{tot} of $MAPbI_3$ on cooling was measured in the mixed H_2/Ar gas.

Similar phenomenon has been reported in perovskite-type halides by earlier researches. Mizusaki *et al*. [12] reported activation energy of 0.69 eV for $CsPbCl_3$ and

0.72 eV for $CsPbBr_3$ in intrinsic region, and 0.25 eV for $CsPbBr_3$ in extrinsic region as shown in Fig. 2-9. Narayan *et al*. [13] reported comparable activation energies as 0.17 eV and 0.70 eV for $CsPbCl_3$ materials. According to the variation of activation energy estimated in this work, the $MAPbX_3$ materials might be in a "frozen" state with a constant concentration of defects vacancies at low temperature, and above the transition point, the high conductivity should due to the formation of full Schottky disorder with apparent activation energy corresponding to $\Delta H_S/5 + E_a$. The enthalpy change, ΔH_S, that could be estimated in $MAPbBr_3$ in present experiment is much smaller than the reported inorganic perovskites, such as, $CsPbCl_3$ and $CsPbBr_3$, which may be due to the strong volatility of organic molecules at higher temperatures, in other words, owing to the low chemical stability. Based on the discussion about total conductivities of $MAPbI_3$ in different atmosphere, it may conclude that the presence of H_2 will effectively inhibit the evaporation of CH_3NH_2, indicating H_2 should be one of the important compositional parameters that control the defect chemistry in $MAPbX_3$ materials.

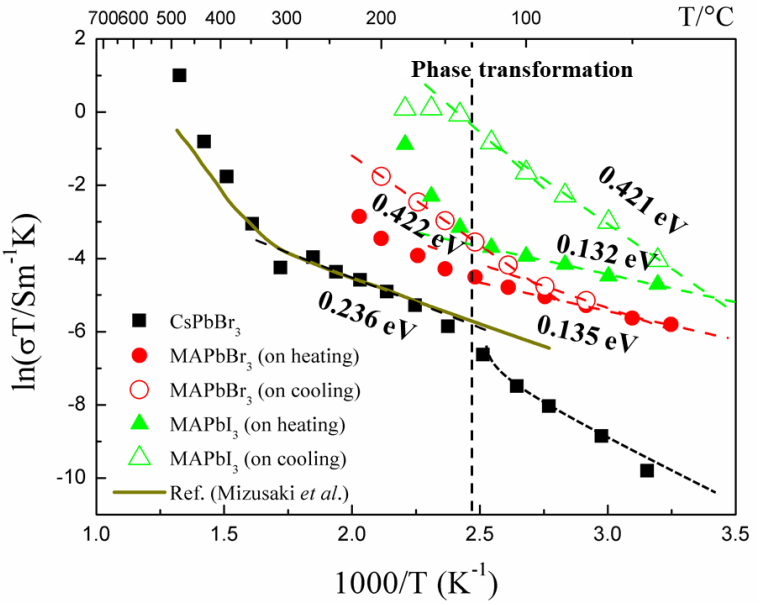

Fig. 2-9 Total conductivities of perovskite single crystals measured in a thermal cycle.

2.3.5 Phase Relations and Chemical stability

As the $(MA{\cdot}H)PbX_3$ contains four independent components, the system has to be treated as a quaternary system. To confirm the phase relations, a series samples with different components have been prepared, and after long-term annealing, the

equilibrium state could be achieved. The phase compositions under equilibrium state were analyzed and the phase relations of $MAPbX_3$ could be confirmed as shown in Fig. 2-10 (a).

As Gibbs phase rule predicted in equilibrium state, $f = c - p + 2 = 6 - p$, thus, at a certain temperature and pressure, f=3, which means, three independent variables should be fixed in order to completely describe the state of the system. In phase relations, any three chemical potentials among the components, Pb (s), MA (g), H_2 (g) and Br_2 (l) (or the compounds between them) could be used to control the state of the system. In present work, for convenience, μ_{PbX_2}, μ_{X_2} and μ_{H_2} were used to fix the state in entire region. Under this condition, the A/B ratio and X nonstoichiometry have been totally fixed, and the defect chemistry of $MAPbBr_3$ could be systematically investigated.

The solubility of MABr and $PbBr_2$ in DMF solvent was shown in Fig. 2-10 (b). From the phase diagram of DMF-MABr-$PbBr_2$, the solubility of MABr is almost three times of $PbBr_2$, which means that the A/B ratio can be modified in a relatively wide range, which provides a new path to modify the defect chemistry during fabrication process. If the precursor with different proportions of MABr and $PbBr_2$ in DMF could be prepared, there is high possible that A/B nonstoichiometry in as-prepared perovskite samples could be controlled under the controllable vapor pressure of H_2.

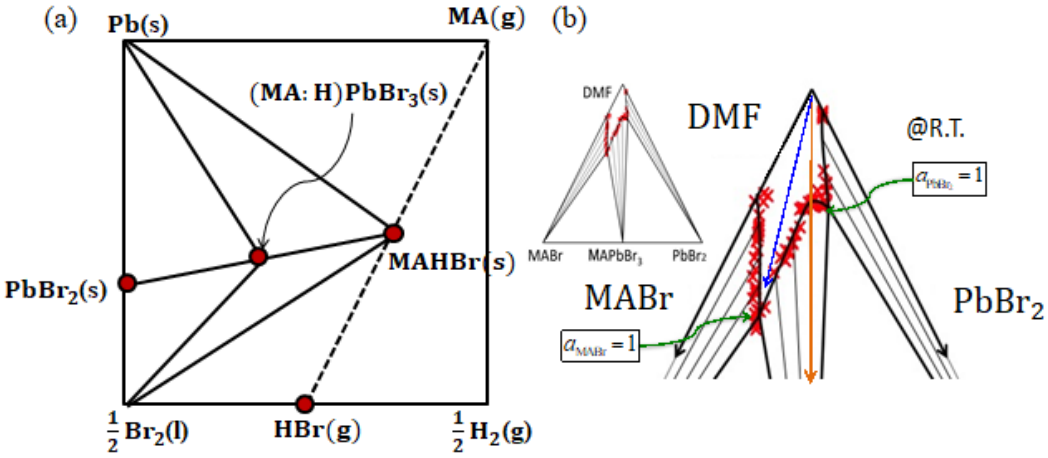

Fig. 2-10 The phase relation of $MAPbBr_3$ (a) and its solubility in DMF solvent (b).

Since the Gibbs formation energy of hybrid peroskites was estimated to be small negative value for both $MAPbBr_3$ and $MAPbI_3$ at room temperature, the materials exhibit intrinsic thermodynamic instability even though without moisture, oxygen or

solar irradiation in the environment. To discuss the stability of $MAPbX_3$ materials, the following reactions should be considered,

$$2(\mathrm{MA}\cdot\mathrm{H})\mathrm{X(s)} \rightarrow 2\mathrm{MA(g)} + \mathrm{H_2(g)} + \mathrm{X_2(s\ or\ l)}, \quad (2\text{-}14)$$

$$\ln K_1 = ({P_{\mathrm{MA}}}^2 \cdot P_{\mathrm{H_2}} \cdot a_{\mathrm{X_2}})/{a_{(\mathrm{MA}\cdot\mathrm{H})\mathrm{X}}}^2 = -\Delta_{\mathrm{r}}G_1/RT, \quad (2\text{-}15)$$

$$2\mathrm{HX(g)} \rightarrow \mathrm{H_2(g)} + \mathrm{X_2(g)}, \quad (2\text{-}16)$$

$$\ln K_2 = (P_{\mathrm{H_2}} \cdot a_{\mathrm{X_2}})/{P_{\mathrm{HX}}}^2 = -\Delta_{\mathrm{r}}G_2/RT, \quad (2\text{-}17)$$

where K_1 and K_2 are the equilibrium constant, $\Delta_{\mathrm{r}}G_1$ and $\Delta_{\mathrm{r}}G_2$ are the Gibbs energy for the reaction expressed in eq. (2-14) and (2-16), respectively, P_{MA}, $P_{\mathrm{H_2}}$and P_{HX} represent the vapor pressure of MA, H_2 and HX gas under equilibrium state, respectively, and $a_{\mathrm{X_2}}$ represents the activity of halogen. The thermodynamic data in eq. (2-15) and (2-17) could be found in previous literature [14] as well as HSC chemistry 6 (Outotec). The vapor pressure of MA (g) and HX (g) under equilibrium condition, P_{MA} and P_{HX}, can be expressed as a function of the vapor pressure of H_2 (g) and the activity of X_2(s or l), $P_{\mathrm{H_2}}$ and $a_{\mathrm{X_2}}$. The stability domain in $MAPbX_2$ under equilibrium state was shown in Fig. 2-11. The chemical potential of HX is an important factor to evaluate the chemical stability of these perovskites, and the consumption of HX governs the whole decomposition process. The P_{HBr} in $MAPbBr_3$ system is 10 orders magnitude higher compared with the P_{HI} in $MAPbI_3$ system in the same range of $P_{\mathrm{H_2}}$ and $a_{\mathrm{X_2}}$, corresponding to a much lower P_{MA} in $MAPbI_3$ system. Therefore, in $MAPbBr_3$ materials, due to the high P_{HBr}, the $P_{\mathrm{H_2}}$should be low enough to inhibit the evaporation of HBr, especially in high $a_{\mathrm{Br_2}}$ range, thus extending the stability domain of the materials. As shown in Fig. 2-11 (a) and (b), at $\log P_{\mathrm{H_2}}$=-15, the stability domain is $\log a_{\mathrm{Br_2}}$=-4~-44, corresponding to the limitation of the evaporation of HBr and MA, while at $\log P_{\mathrm{H_2}}$=0, the stability domain is $\log a_{\mathrm{Br_2}}$=-19~-46. However, in $MAPbI_3$ materials, since the P_{HI}≤0 in a wide $a_{\mathrm{I_2}}$ range, the stability domain was determined by the P_{MA} which will increase with the decreasing $a_{\mathrm{I_2}}$ under a certain $P_{\mathrm{H_2}}$, and that means, to extend the stability domain, the $P_{\mathrm{H_2}}$ in the system should be controlled in a high value as shown in Fig. 2-11 (c) and (d). The calculation results suggested the chemical stability of $MAPbI_3$ is very sensitive to $P_{\mathrm{H_2}}$ compared with $MAPbBr_3$ system, therefore, for $MAPbI_3$, three compositional parameters, $\mu_{\mathrm{PbI_2}}$, $\mu_{\mathrm{I_2}}$ and $\mu_{\mathrm{H_2}}$should be controlled to fix the state in entire region. But for $MAPbBr_3$, in contrast, only two parameters, $\mu_{\mathrm{PbBr_2}}$and $\mu_{\mathrm{Br_2}}$ need to be controlled in subsequent experiments.

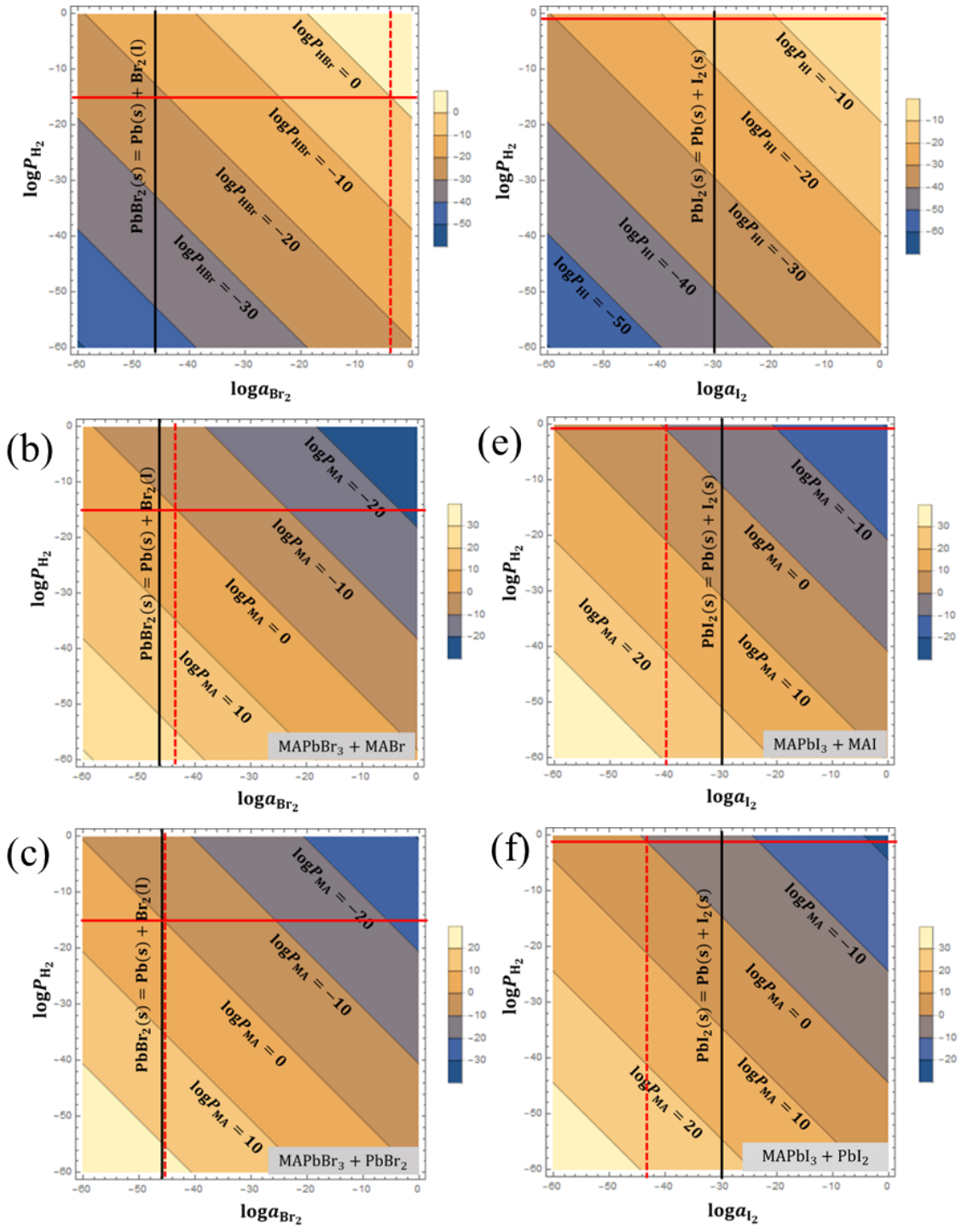

Fig. 2-11 The calculated equilibrium vapor pressure of HX (g) and MA (g) in $MAPbBr_3$ and $MAPbI_3$ materials. (a), (b) and (c) represent the $\boldsymbol{P_{HBr}}$, $\boldsymbol{P_{MA}}$ in MABr-rich condition, and $\boldsymbol{P_{MA}}$ in $PbBr_2$-rich condition, respectively; (d), (e) and (f) represent the $\boldsymbol{P_{HI}}$, $\boldsymbol{P_{MA}}$ in MAI-rich condition, and $\boldsymbol{P_{MA}}$ in PbI_2-rich condition, respectively. (black lines represent the limitation of Pb precipitation, red dashed line represent the boundary of stability domain at the certain $\boldsymbol{P_{H_2}}$).

The TG/DTA curves and total conductivities measured in both Ar and Ar/H_2 atmosphere also support that the $MAPbI_3$ material is significantly sensitive to H_2, especially under the situation at high temperatures.

According to the analysis of the phase relations in hybrid perovksites, the number of chemical potential of components that should be fixed to completely describe the state of the system was confirmed, which will be helpful to control the A/B ratio and X nonstoichiometry during the measurements of partial and total conductivities with the variation of halogens activity.

2.4 Summary

High quality single crystals of $MAPbBr_3$ and $MAPbI_3$ perovskites were prepared by solution-process technology with clear transparency and well-controlled shapes. XRD patterns of single crystals showed that $MAPbBr_3$ is in cubic phase with {001} orientation, while $MAPbI_3$ showed tetragonal symmetry with {112} orientation at room temperature. The TG/DTA analysis revealed a high thermal stability of single crystals above 240°C in both Ar and Ar/H_2 atmosphere. For $MAPbBr_3$ materials, the presence of H_2 almost had no effect on the decomposition temperature, however, $MAPbI_3$ single crystals exhibited an improvement of thermal stability in Ar/H_2 atmosphere. The phase stability was also confirmed by high temperature XRD, which exhibited a phase decomposition of samples at 250°C in well agreement with the TG/DTA profiles, and the phase transition of $MAPbI_3$ from tetragonal to cubic symmetry at ~55° was also observed on XRD patterns. The total conductivities of single crystals were measured by ac impedance method varied with temperature. The activation energy of $MAPbBr_3$ and $MAPbI_3$ single crystals was estimated to be 0.13 eV at low temperature, followed by a sharp bending as the temperature increased. A transition from intrinsic to extrinsic region was observed at the temperature below 100°C on Arrhenius plots in both $MAPbBr_3$ and $MAPbI_3$ materials, which indicated the material is in a “frozen” state with a fixed defects concentration at lower temperatures, above the transition temperature, the abrupt increase of apparent activation energy should contributed by the enthalpy of the vacancy formation. The phase relations of perovskites were also discussed in this chapter. $MAPbX_3$ materials should be considered as a quaternary system, three independent variables, μ_{PbX_2}, μ_{X_2} and μ_{H_2} should be fixed to completely

describe the state of the system. The thermodynamic stability of $MAPbX_3$ system was also discussed, and under equilibrium state, μ_{HBr} was found much higher than μ_{HI}, thus $MAPbBr_3$ is less sensitive to the vapor pressure of H_2. The analysis in this chapter is helpful for understanding the chemical stability and the defect chemistry of $MAPbX_3$ materials, and confirmed the method to control A/B ratio and X nonstoichiometry in following dc polarization.

2.5 Reference

[1] Mitzi DB. Synthesis, structure, and properties of organic-inorganic perovskites and related materials. *Prog. Inorg. Chem.,* 48, 1–121 (1999).

[2] Saidaminov MI, Abdelhady AL, Murali B, *et al*. High-quality bulk hybrid perovskite single crystals within minutes by inverse temperature crystallization. *Nat. commun.,* 6: 7586 (2015).

[3] Shi D, Adinolfi V, Comin R, *et al*. Low trap-state density and long carrier diffusion in organolead trihalide perovskite single crystals. *Science,* 347 (6221): 519-522 (2015).

[4] Saidaminov MI, Abdelhady AL, Maculan G, *et al*. Retrograde solubility of formamidinium and methylammonium lead halide perovskites enabling rapid single crystal growth. *Chem. Commun .,* 51(100): 17658-17661 (2015).

[5] Liu Y, Sun J, Yang Z, *et al*. 20-mm-large single-crystalline formamidinium-perovskite wafer for mass production of integrated photodetectors. *Adv. Opt. Mater.,* 4(11): 1829-1837 (2016).

[6] Sydney U, Wang Q. Composition-dependent photoluminescence intensity and prolonged recombination lifetime of perovskite $CH_3NH_3PbBr_{3-x}Cl_x$ films. *Chem. Commun.,* 50**,** 11727–11730 (2014).

[7] Baikie T, Fang Y, Kadro JM, *et al*. Synthesis and crystal chemistry of the hybrid perovskite $(CH_3NH_3)PbI_3$ for solid-state sensitised solar cell applications. *J Mater. Chem., A*, 1(18): 5628-5641 (2013).

[8] Hirotsu S, Harada J, Iizumi M, *et al*. Structural phase transitions in $CsPbBr_3$. *J. Phys. Soc. Jpn.*, 37(5): 1393-1398 (1974).

[9] Maeda M, Hattori M, Hotta A, *et al*. Dielectric studies on $CH_3NH_3PbX_3$ (X= Cl and Br) single crystals. *J. Phys. Soc. Jpn.*, 66(5): 1508-1511 (1997).

[10] Yang TY, Gregori G, Pellet N, *et al*. The significance of ion conduction in a hybrid organic-inorganic lead-iodide-based perovskite photosensitizer. *Angew. Chem*., 127(27): 8016-8021 (2015).

[11] Knop O, Wasylishen RE, White MA, *et al*. Alkylammonium lead halides. Part 2. $CH_3NH_3PbX_3$ (X= Cl, Br, I) perovskites: cuboctahedral halide cages with isotropic cation reorientation. *Can. J. Chem*., 68(3): 412-422 (1990).

[12] Mizusaki J, Arai K, Fueki K. Ionic conduction of the perovskite-type halides. *Solid State Ionics*, 11(3): 203-211 (1983).

[13] Narayan RL, Sarma MVS, Suryanarayana SV. Ionic conductivity of $CsPbCl_3$ and $CsPbBr_3$. *J mater. Sci. lett*., 6(1): 93-94 (1987).

[14] Ivanov IL, Steparuk AS, Bolyachkina MS, *et al*. Thermodynamics of formation of hybrid perovskite-type methylammonium lead halides. *J. Chem. Thermodyn*., 116: 253-258 (2018).

CHAPTER 3

Partial and Total Conductivities of $MAPbBr_3$ Single Crystals

3.1 Introduction

Diffusion of intrinsic ionic defects in $MAPbX_3$ (X=Cl, Br, I) perovskites has important effect on its long-term stability and performance of solar cells, which has drawn strong attention after the anomalous photocurrent density-voltage (*J–V*) hysteresis was reported. The activation energy of the migration of various ionic vacancies in hybrid perovskites was calculated, and the halogen vacancies exhibit a much lower E_a compared with the vacancy of MA and Pb [1-4], indicating the halide ions is the possible dominant carriers in materials. The conduction of halogen ions will be determined by the concentration and mobility of intrinsic ionic vacancies, which is sensitive to the fabrication conditions and thermal history [5, 6]. Stoumpos *et al*. [7] reported a simple carrier-type transformation in various perovskite compounds (including inorganic and hybrid perovskites) depending on synthetic methods, and obtained *n*-type semiconductor from solution method, and *p*-type through solid state reactions in a controllable manner. Impedance spectroscopy studies also suggest the hybrid perovskites exhibit ionic charge transport in addition to electronic conduction, the details of partial conductivity of holes and electrons have never been established.

Present work focused on the investigation of the partial (electronic and ionic) and total conductivity of $MAPbBr_3$ single crystals with controllable bromine activity by assuming a frozen Schottky pair of MA and Pb vacancies. Hebb-Wagner dc polarization was conducted from RT to 95 °C to measure the partial electronic conductivity using an asymmetric cell with an ion blocking electrode as well as a reversible electrode. The transference number of ions was obtained using current interruption technology during polarization. The total conductivity of single crystals with different bromine activity was measured by an ac impedance method. In the ternary system of $MAPbBr_3$ as we have discussed in Chapter 2, two compositional parameters, μ_{PbBr_2} and μ_{Br_2}, have to be fixed to control the whole system in present work. The possible defect chemical model in $MAPbBr_3$ perovskite was also discussed in this chapter.

A *p* to *n* transition upon variation of bromine activity was observed, but it is confirmed that the partial ionic conductivity dominates in a wide range of stability domain, which means the system is electrochemical system. The electrochemical window that governs the chemical stability under applied voltage or generated photo-voltage was estimated and discussed. This work will be helpful for understanding the defect chemistry of $MAPbBr_3$ materials and provide a possible method for regulating carrier density and ionic defects level in the materials.

3.2 Experimental

3.2.1 Asymmetric Cell for Polarization

Hebb-Wagner dc polarization was conducted using an asymmetric cell with a ion blocking electrode as well as a reversible electrode. In present work, we used dense Au film about 500nm as blocking electrode which was deposited on singlecrystalline $MAPbBr_3$ surface after carefully ground and polished. The mixed powders of Pb and $PbBr_2$ were used as reversible electrode. The powders were dispersed in DMF solvent which was saturated by $MAPbBr_3$. The polar organic solvent was used to promote the equilibrium between grains of each component in reversible electrode (see phase relation in Chapter 2). The schematic diagram of the asymmetric cell for polarization was shown in Fig. 3-1, in which cell constant L/A is 1.99 cm^{-1} (L is the thickness of single crystal, and A is the electrode area).

During polarization, bromine ion activity at the blocking electrode is determined by the applied voltage, and in order to eliminate the possible reaction between Au electrode and Br_2 at the interface, the following reaction equation was considered,

$$2Au + Br_2 = 2AuBr, \quad (3\text{-}1)$$

$$K = a_{AuBr}^2 / a_{Au} a_{Br_2} = 1/a_{Br_2}, \quad (3\text{-}2)$$

where K is the equilibrium constant of the reaction (3-1), a_{Br_2} is the activity at the interface. The equilibrium constant was calculated using the software HSC chemistry 6 (Outotec) which compiled Gibbs energy minimization and thermodynamic constants in a database. For example, at 25°C, log$K$=2.337, and at 95°C, log$K$=1.367, the corresponding bromine activity was calculated to be $10^{-2.337}$ and $10^{-1.367}$, respectively, which means, the bromine activity should be carefully controlled below $10^{-2.337}$ during

dc polarization in order not to form AuBr at equilibrium state on the interface between blocking electrode and crystal for measurements.

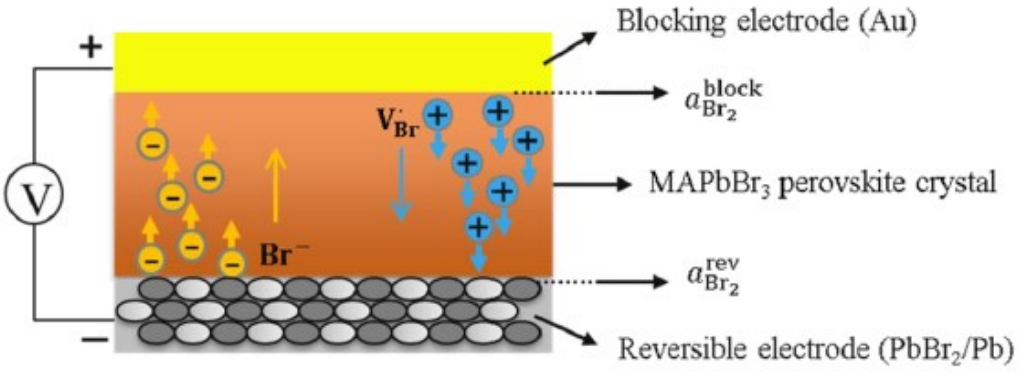

Fig. 3-1 The asymmetric cell used for polarization with an ionic blocking electrode and a reversible electrode.

3.2.2 Hebb-Wagner Dc Polarization

The measurements were performed at RT, 40 °C, 55 °C, 75 °C, 95 °C under controlled Br_2 activity at the reversible electrode, $a_{Br_2}^{rev}$. Considering the following reaction,

$$Pb + Br_2 \rightarrow PbBr_2, \quad (3\text{-}3)$$

Br_2 activity, $a_{Br_2}^{rev}$, is defined by,

$$a_{Br_2}^{rev} = 1/K(a_{PbBr_2}/a_{Pb}) , \quad (3\text{-}4)$$

where K is the equilibrium constant of the reaction (3-3), which was calculated using the software HSC chemistry 6 (Outotec) as, K=$10^{45.683}$, $10^{43.354}$, $10^{41.235}$, $10^{38.690}$, $10^{36.417}$ at the designed temperatures for measurement respectively. The Br_2 activity at the reversible electrode was calculated as, $a_{Br_2}^{rev}$=$10^{-45.683}$, $10^{-43.354}$, $10^{-41.235}$, $10^{-38.690}$, $10^{-36.417}$ respectively.

The potentiostatic dc polarization was conducted using an Ivium station (CompactStat B10060, Ivium Technologies, Netherlands) by applying voltage range from 0.4V to 1.2V, and the value of current i_{ext} under different applied voltage E_{app} was recorded after the steady state was achieved.

All the measurements were conducted under dark condition. Ar gas was used to avoid the possible degradation of samples by exposed to air atmosphere.

3.2.3 Current Interruption Technology

The measurement of ion transference number was conducted using the Ivium station (CompactStat B10060, Ivium Technologies, Netherlands) by a current interruption technique during the dc polarization. The current was interrupted after the steady state was achieved, and the open circuit voltage dropped immediately owing to so-called *IR* loss, and then gradually decayed. The open circuit voltage with time was recorded at the time interval of 40 ms.

3.2.4 Total Conductivity Measurements

The dependence of total conductivity, σ_{tot}, on Br_2 activity was measured by a two-probe ac impedance method with Au electrode.

The defect chemistry of $MAPbBr_3$ system was controlled by both A/B ratio and Br nonstoichiometry which governed by chemical potential of components, since the system is ternary one. In present work, we applied an annealing method to control $\mu_{\mathrm{PbBr_2}}$ and $\mu_{\mathrm{Br_2}}$ of $MAPbBr_3$ single crystals. Samples were placed in a vessel filled with DMF solvent saturated with $MAPbBr_3$ and $PbBr_2$ powders, and a series different concentration of pure Br_2 or Pb powder. According to the discussion of phase relation in Chapter 2, the sample was annealed in two equilibrium triangles consisted of $MAPbBr_3$-$PbBr_2$-Br_2 and $MAPbBr_3$-$PbBr_2$-Pb respectively. The vessel was sealed and annealed for four weeks under Ar atmosphere to reach the chemical equilibrium state. The solution with Br_2 concentration is prepared by infinite dilution, and the Br_2 activities in different solution for annealing were confirmed by the measurements of the electromotive force, *emf*, of a Br_2 concentration cell.

Although pure $PbBr_2$ exhibits a low conductivity, the conductivity is greatly enhanced by KBr doping, and the maximum conductivity in $(1\text{-}x)PbBr_2 \cdot xKBr$ solid electrolytes was obtained at x=0.02 and the transference number of Br^- was reported almost equal to unity [8], thus, $0.98PbBr_2 \cdot 0.02KBr$ materials can be used as a solid electrolyte of the Br_2 concentration cell. The mixture of $0.98PbBr_2 \cdot 0.02KBr$ was dried at 300°C for 1 h, and then melted at 500°C for 1 h to yield a solid solution. The powder was ground and pressed into a pellet under a pressure of 150 MPa. The porosity for the pellet was estimated of ~10%, determined by the ratio of a measured density and a theoretical one.

Pure Br_2 was used to fix the bromine activity at reference electrode side. The Br_2 activities in single crystals after annealing could be obtained from the electromotive force, *emf*. The Br_2 activity of single crystals annealed in $MAPbBr_3$-$PbBr_2$-Pb triangle was determined by eq. (3-4) in which a_{PbBr_2} and a_{Pb} are equal to unity.

The total conductivity of the single crystals was measured using solarton 1255B frequency response analyzer (solarton Inc,, England) coupled with solarton 1296 dielectric interface (solarton Inc,, England) within the frequency range from 1 MHz to 0.1 Hz. The ac impedance measurement was conducted at RT, 40 °C, 55 °C, 75 °C, and 95 °C under Ar atmosphere in dark condition.

3.3 Results

3.3.1 Steady State Current and Partial Conductivities

The steady-state current, i_{ext}, at RT, 40 °C, 55 °C, 75 °C and 95 °C as a function of applied voltage, E_{app}, were shown in Fig. 3-2. The steady-state current exhibits a significant non-linear dependence on E_{app}. On the polarization curves, a limited increase of i_{ext} was observed with applied voltage increasing from 0.45V to intermediate voltage, and then a rapid rise followed as the voltage increasing to 1.2V. The variation of polarization curves reveals a similar tendency at different temperatures under present experimental conditions, and shows an exponential increase relationship within the voltage range of measurement.

To estimate the variation of i_{ext} with E_{app}, the least-squares polynomial fitting was applied in present work as follows,

$$i_{ext} = \sum_{k=0}^{k=5,7 \text{ or } 9} a_k E_{app}^k. \quad (3\text{-}5)$$

The total electronic conductivity, $\sigma_e^{block} = \sigma_n + \sigma_p$, at the interface of blocking electrode, $a_{Br_2}^{block}$, can be calculated from the differentiation of polarization curves with the following equation [9],

$$\sigma_e^{block} = \frac{L}{A}\frac{\partial i_{ext}}{\partial E_{app}}, \quad (3\text{-}6)$$

where A and L are the area of electrode and the thickness of the crystal for measurement, respectively. The values of $a_{Br_2}^{block}$ was defined by Nernst's equation, which can be rearranged to,

$$\log a_{Br_2}^{block} = \frac{2E_{app}F}{2.303RT} + \log a_{Br_2}^{rev}, \quad (3\text{-}7)$$

where F, R and T are Faraday constant, gas constant and temperature, respectively. The results of the total electronic conductivities, σ_e^{block}, as a function of Br_2 activities, $a_{Br_2}^{block}$, were calculated and plotted in Fig. 3-3 by solid symbols.

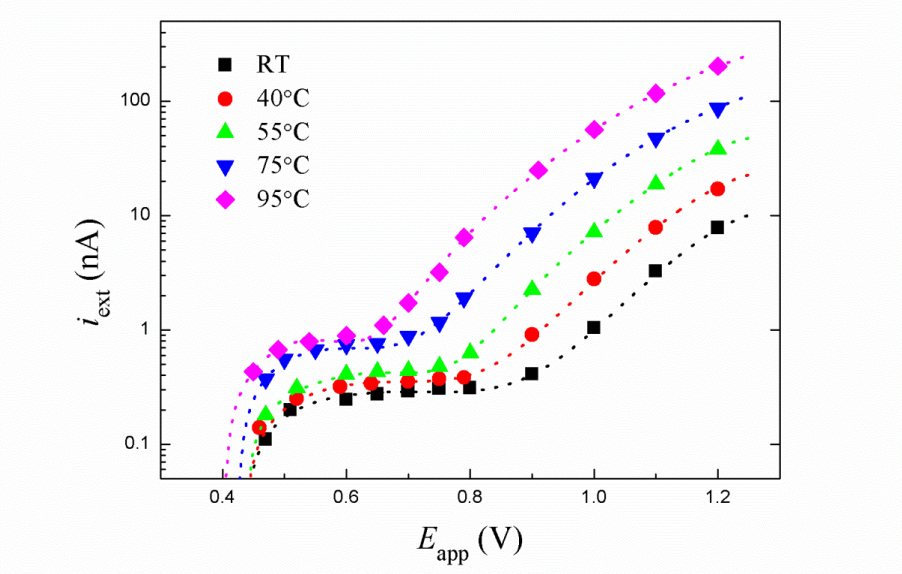

Fig. 3-2 The relationship between steady state current, $\boldsymbol{i_{ext}}$ and applied voltage, $\boldsymbol{E_{app}}$, by the dc polarization measurement performed at RT, 40°C, 55°C, 75°C, 95°C under $\boldsymbol{a_{Br_2}^{rev}}$. Cell constant parameter L/A = 1.99 cm^{-1}.

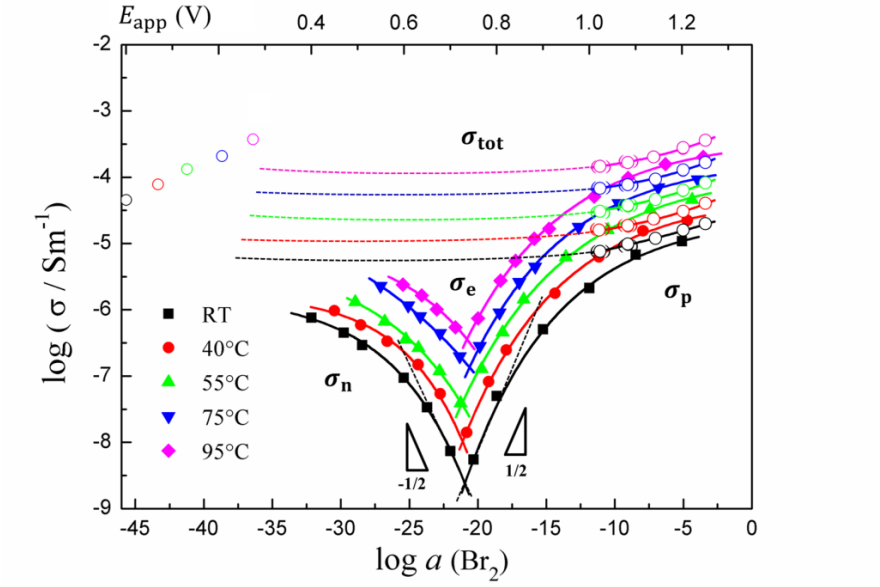

Fig. 3- 3 The variation of $\boldsymbol{\sigma_e}$ (solid symbols) calculated from the slope of polarization curves in Fig. 3-2 as a function of $\boldsymbol{a_{Br_2}}$, and $\boldsymbol{\sigma_{tot}}$ (open symbols) by ac

impedance method measured with the crystals after annealed. The dotted lines show the extrapolation of $\boldsymbol{\sigma_{tot}}$ dependency on $\boldsymbol{a_{Br_2}}$, and the dashed lines indicate $\boldsymbol{a_{Br_2}^{1/2}}$ and $\boldsymbol{a_{Br_2}^{-1/2}}$ dependency to $\boldsymbol{\sigma_p}$ and $\boldsymbol{\sigma_n}$ predicted from the defect model, respectively.

A *p* to *n* transition upon the variation of a_{Br_2} was observed at ~10^{-20}, and the transition point showed a slight shift to high a_{Br_2}region as the temperature increased from RT to 95°C. In the a_{Br_2} range higher than *p*/*n* transition point, σ_e^{block} exhibited approximate a 1/2 power dependency on $a_{Br_2}^{block}$, and then gradually increasing followed the exponential correlation on $a_{Br_2}^{block}$. In very high Br_2 activity range above 10^{-5}, σ_p gradually saturated to a constant value of conductivity. The similar proportionality in the opposite sign of dependence can be observed in low a_{Br_2} region, and the σ_n also gradually saturated at a constant value in low $a_{Br_2}^{block}$ domain. Particularly, in comparison with the saturated conductivity of holes, $\sigma_p^{sat.}$, the saturaed conductivity of electrons, $\sigma_n^{sat.}$, is lower by an order of magnitude, that means, the carrier density of *p* and *n* was asymmetric in present measurement. The total electronic conductivities can be expressed as,

$$\sigma_{et} = n_e e\mu_e + n_p e\mu_p, \tag{3-8}$$

where, σ_{et} is the total electronic conductivity, n_e and n_p represent carrier density, $\mu_e$and μ_p are mobility of electrons and holes, respectively. The carrier mobility of single-crystalline $MAPbBr_3$ was measured of 115 cm^2/Vs with time-of-flight technique [10], and if the mobility of electrons in *n*-type domain and holes in *p*-type domain were assumed comparable, the carrier density of *p* can be estimated as 5×10^9 cm^{-3} under saturation conditions at room temperature, which is in agreement with the values reported by Shi *et al.* [10].

The partial electronic conductivities reveal similar dependency on the a_{Br_2} measured at RT, 40°C, 55°C, 75°C and 95°C, except for a reduction on dependency coefficient of σ_e^{block} on $a_{Br_2}^{block}$ at *p*/*n* transition region from ~0.5 at RT to ~0.35 at 95°C.

3.3.2 Transference Number of Ions

The current was interrupted after the steady state was achieved during polarization, and the open circuit voltage, E_{open}, was immediately recorded as a function of time

under different temperatures after current interruption by opening circuit. The open circuit voltage showed an abrupt *IR* drop at the beginning stage, and then slowly decreased with time extended until the equilibrium state was achieved as shown in Fig. 3-4. The relations between E_{app} and E_{open} obtained under different $a_{\mathrm{Br_2}}^{\mathrm{rev}}$ at reversible electrode at the temperature of RT, 55°C and 95°C were shown in Fig. 3-5. As E_{open} can be expressed as [11],

$$E_{\mathrm{open}} = \frac{1}{2F}\int_{a_{\mathrm{Br_2}}=a_{\mathrm{Br_2}}^{\mathrm{rev}}}^{a_{\mathrm{Br_2}}=a_{\mathrm{Br_2}}^{\mathrm{block}}} t_{\mathrm{ion}} d(RT\ln a_{\mathrm{Br_2}}), \tag{3-9}$$

And the corresponding E_{app} as,

$$E_{\mathrm{app}} = \frac{1}{2F}\ln\left(a_{\mathrm{Br_2}}^{\mathrm{block}}/a_{\mathrm{Br_2}}^{\mathrm{rev}}\right). \tag{3-10}$$

Similar to the calculation of steady-state current curves, the least-squares polynomial fitting was also applied using expression as follows,

$$E_{\mathrm{open}} = \sum_{k=0}^{k=3\ \mathrm{or}\ 5} a_k E_{\mathrm{app}}^{k}. \tag{3-11}$$

The transference number of ions under different $a_{\mathrm{Br_2}}^{\mathrm{block}}$ at the interface of blocking side, can be calculated from the differentiation of each E_{open} as a function of E_{app} as follows,

$$t_{\mathrm{ion}} = dE_{\mathrm{open}}/dE_{\mathrm{app}}. \tag{3-12}$$

The calculation results of ion transference number were plotted in Fig. 3-6 at the temperature of RT, 55°C and 95°C.

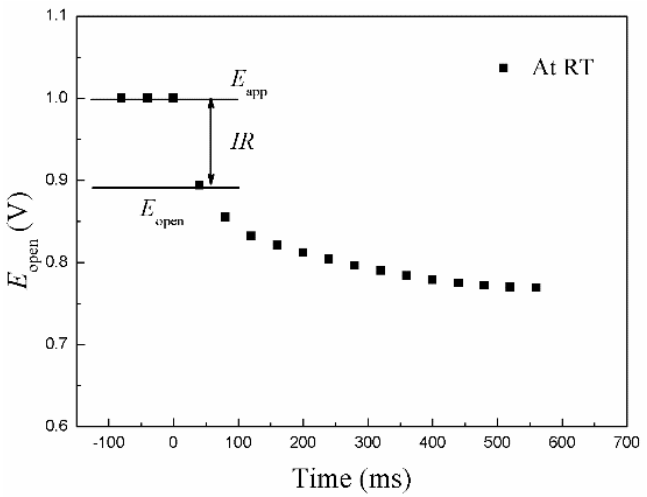

Fig. 3-4 An example of current interruption technology. The E_{open} varied with time.

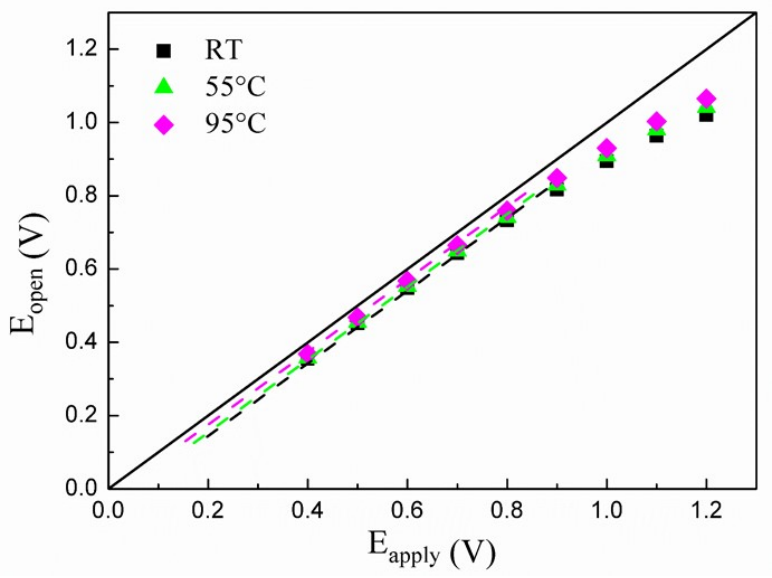

Fig. 3-5 The open circuit voltage, $\boldsymbol{E_{open}}$, as a function of applied voltage, $\boldsymbol{E_{app}}$, at RT, 55°C and 95°C measured by current interruption technology.

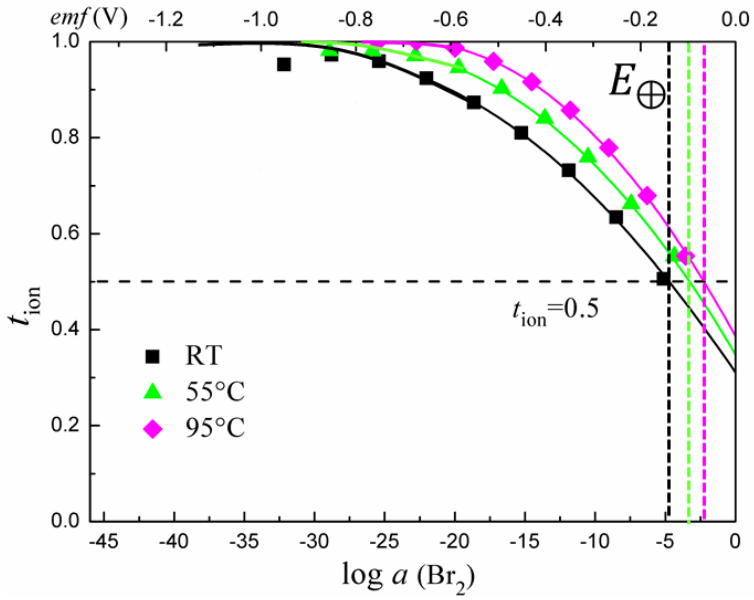

Fig. 3-6 The transference number of ions at different temperatures calculated from the slope of the curves in Fig. 3-5 ($\boldsymbol{E_{\oplus}}$ was defined as the equilibrium *emf* of the transition from ionic dominant domain to *p*-type domain, using pure Br_2 as a reference).

As the a_{Br_2} decrease, the ions transference number, t_{ion}, gradually increase to unity, which is essentially consistent with the a_{Br_2} at the *p*/*n* transition in Fig. 3-3, and the

deviation at low a_{Br_2} range should due to the overpotential caused by the Au/$MAPbBr_3$ interface, as shown in Fig. 3-5 (dashed lines). Meanwhile, t_{ion} exhibits a positive dependency on temperature. The dashed line represents t_{ion}=0.5 as marked in Fig. 3-6, and from the intersections of t_{ion}=0.5 with t_{ion} curves under different temperatures, the switching from ionic conductivity domain to electronic conductivity domain could be obtained as, a_{Br_2}=$10^{-4.6}$, $10^{-3.2}$ and $10^{-2.2}$ at RT, 55°C and 95°C, respectively. And the corresponding equilibrium *emf* was defined as $E_{\oplus}$ (using pure Br_2 as reference), which represents the transition from ionic dominant domain to *p*-type domain. Meanwhile, no *n*-type domain could be observed at the low a_{Br_2} range under present experimental conditions. This work reveals a very high ion transference number that suggests ion is the majority carriers and is predominant in a board range of a_{Br_2} domain, while electrons and holes are just minority carriers.

3.3.3 Total Conductivity

The phase purity of the solid solution was shown in Fig. 3-7, and the total conductivity was in Fig. 3-8. Compared to pure $PbBr_2$ materials, the total conductivity of solid solution increased by more than one order of magnitude, and achieved a maximum conductivity of 2.48×10^{-6} $S\cdot cm^{-1}$ at 298 K in present work, comparable with the values reported by Aono *et al.* [8].

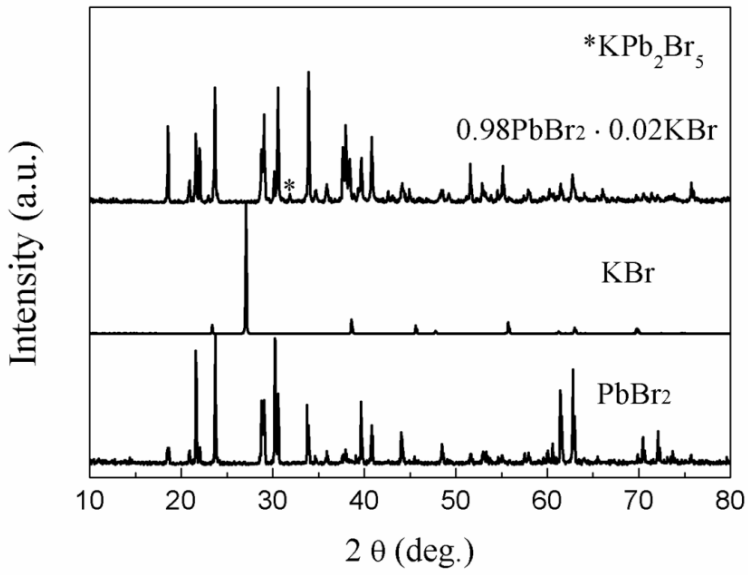

Fig. 3-7 The XRD patterns of $0.98PbBr_2\cdot0.02KBr$ solid solution.

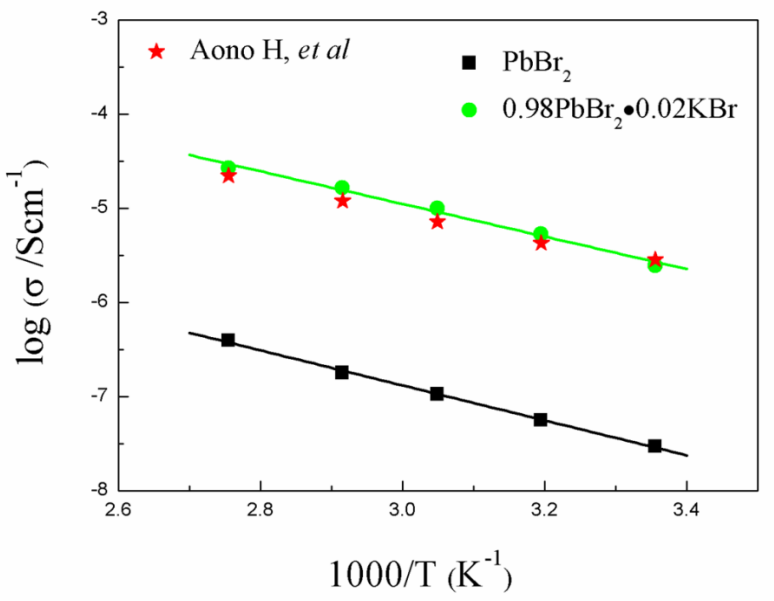

Fig. 3- 8 The total conductivities of pure $PbBr_2$ and $0.98PbBr_2 \cdot 0.02KBr$ solid solution.

The schematic diagram of the Br_2 concentration cell was shown in Fig. 3-9. The *emf* of the concentration cell between Au electrodes obeys the Nernst equation,

$$emf = -\frac{RT}{2F}\ln\frac{a_{Br_2}}{a^{\theta}_{Br_2}}, \tag{3-13}$$

where F, R and T are Faraday constant, gas constant and temperature, respectively, $a^{\theta}_{Br_2}$ represents the Br_2 activity of liquid pure Br_2, and a_{Br_2} represents the Br_2 activities in solutions used for annealing. Since pure Br_2 was used as reference, the reaction between Br_2 and Au should be taken into account, thus, $a_{Br_2} \approx 10^{-2.337}$ at interface of electrolyte/Br_2 using eq. (3-1) and (3-2) if a well-dispersed two-phase mixture is formed under equilibrium state. The a_{Br_2} in DMF-$PbBr_2$-Br_2 solutions can be estimated from the *emf* measurements.

Fig. 3-10 showed the relations between molar fraction of Br_2, x_{Br_2} and Br_2 activity in organic solution for annealing with red solid symbols. Because of the severe deviation of x_{Br_2} by infinite dilution, especially at extremely low Br_2 concentration range, only part of data was plotted in Fig. 3-10. In infinitely diluted solution, the *emf* can be expressed based on Henry's law as follows,

$$emf = -\frac{2.303RT}{2F}(\log x + \log\gamma^{0}_{Br_2}), \tag{3-14}$$

where x represents the concentration of Br_2 in solution, $\gamma^{0}_{Br_2}$ is activity coefficient of ideal solution. The *emf* data basically located following linear dependency on x_{Br_2}, and

the differential is in well agreement with the value of $-\frac{2.303RT}{2F}$ in eq. (3-14). Considering the huge experimental error caused by infinite dilution in low concentration range, only the data in high concentration were used in Fig. 3-10.

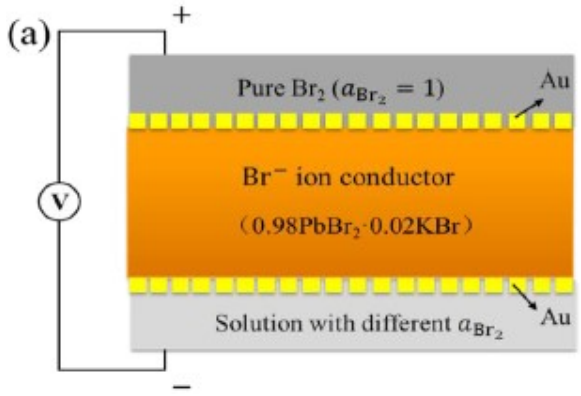

Fig. 3-9 The schematic structure of Br_2 concentration cell used for *emf* measurements.

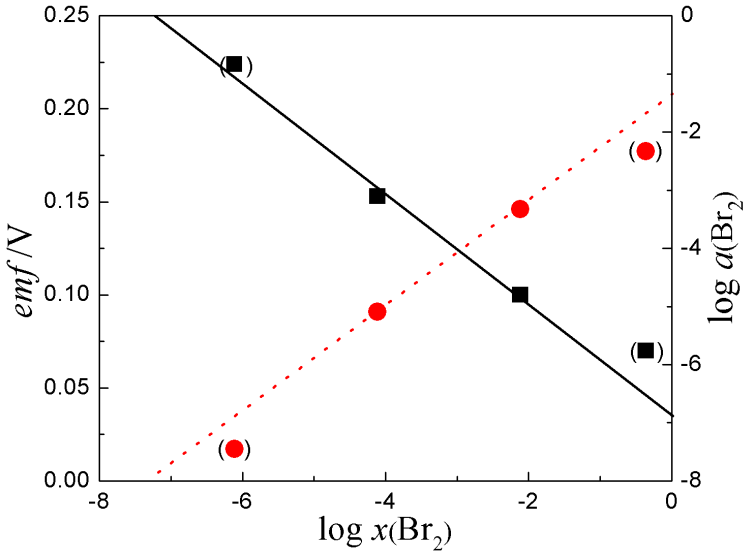

Fig. 3-10 The *emf* of Br_2 concentration cell, and the relations between the molar fraction and activity of Br_2 in organic solution.

After annealing for four weeks, the XRD patterns of annealed samples has been detected, and only {001} diffraction could be observed from XRD patterns in Fig. 3-11 indicating crystal orientation maintain almost the same with the as-grown crystals. The total conductivities, σ_{tot} under different Br_2 activity were measured by an ac impedance method using crystals after annealed in DMF-$PbBr_2$-Br_2 and DMF-$PbBr_2$-Pb solutions. The impedance spectra were shown in Fig. 3-12, and in general, only one semicircle

could be observed in spectra. A very simple equivalent circuit that describes the physical processes taking place in cell is represented in this figure. In this model, the ionic resistance, R_{ion} is coupled to C_d, and then paralleled with the electronic resistance, R_{eon}. The constant phase element QPE is dominated by geometric capacitance, and in some examples may contain components of interface layers responding in a high frequency region.

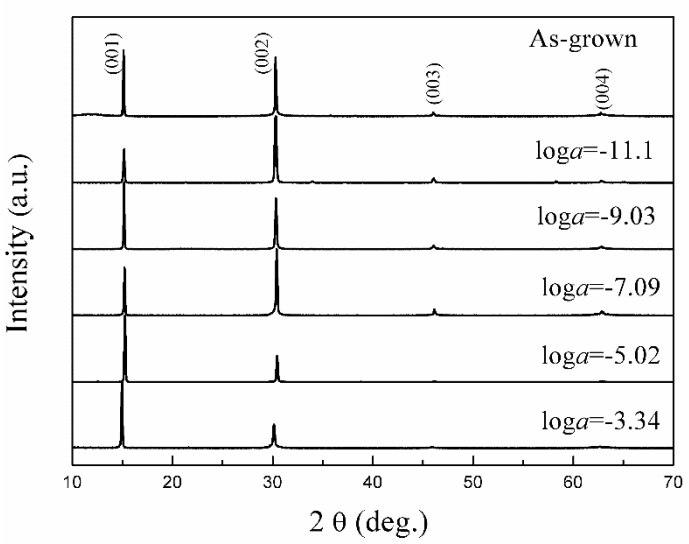

Fig. 3-11 The XRD patterns of single crystals after annealed compared with the as-grown crystals.

An increasing of total conductivity was observed at high a_{Br_2}as well as very low a_{Br_2} domain as shown in Fig. 3-3 with open symbols. At *p*-type domain confirmed by ion transference number, the improvement of the σ_{tot} can be explained by the enhancement contributed by hole conductivity, while the ionic conductivities maintains unchanged compared with the ion dominant region. At extremely low a_{Br_2} domain, the increasing of total conductivity should be related to the enhancemnet of ionic conductivity, since there is no *n*-type domain could be observed and maintains ion dominant in this region. The Arrhenius relations of total conductivities were plotted in Fig. 3-13. The activation energy of ions was estimated in the range of 0.38~0.42 eV, and showed an increase tendency with the increasing of a_{Br_2} which may due to the contribution of holes at high a_{Br_2} domain. The E_a is basically consistent with the value reported by Baikie *et al* [12], and also in good agreement with the discussion in Chapter 2. However, in low a_{Br_2} domain, the activation energy of ions migration exhibited a significant decreas to 0.31 eV contributed by almost pure ionic conduction. Compared with E_a measured in higher

a_{Br_2} domain, the reduction may indicate ionic carriers are predominant, and almost no contribution from electrons because of the electrons trapping at low a_{Br_2} region. The ionic conductivities, σ_{ion}, could be calculated from the total and partial electronic conductivities as, $\sigma_{ion} = \sigma_{tot} - \sigma_e$ with the variation of a_{Br_2}, which is consistent with the variation of ion transference number. The analysis provides an approach to understand the defect chemistry and investigate the defect model of $MAPbBr_3$ system.

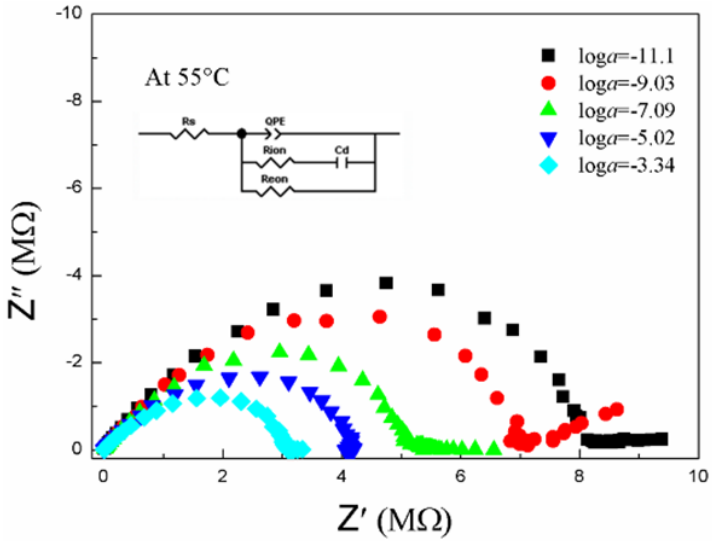

Fig. 3-12 The ac impedance spectra of single crystals after annealed in solution with different Br_2 activity at 55°C.

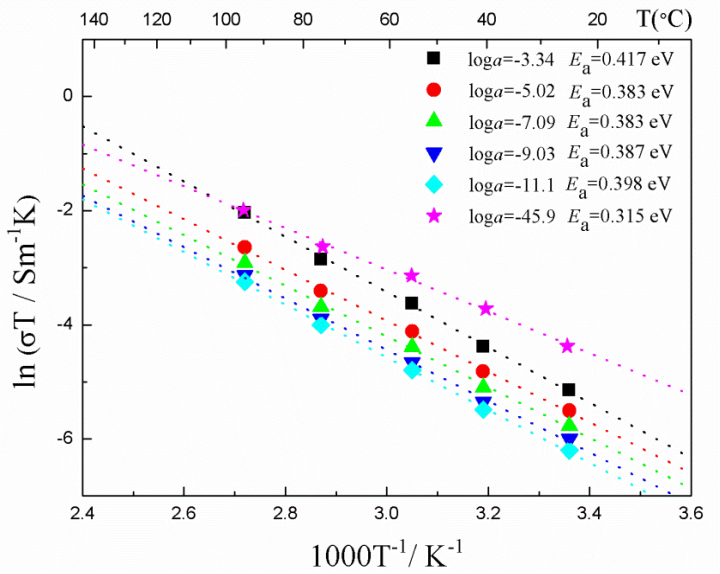

Fig. 3-13 The Arrhenius relations of total conductivities measured from the single crystals after annealed.

3.4 Discussion

3.4.1 Theoretical Foundation of Dc Polarization

The partial electronic and ionic conductivity can be measured by Hebb-Wagner dc polarization to characterize a mixed ionic electronic conductor [13, 14]. The relationship between steady-state current and applied voltage in solid electrolyte was first reported by Wagner [15], and then Choudhury *et al*. [16] investigated the theoretical relation of $i_{\mathrm{ext}} \sim V_{\mathrm{T}}$ in YSZ materials. In the present work, an asymmetric cell for polarization was described as follows,

$$\mathrm{PbBr_2/Pb\ (reversible)}, a_{\mathrm{Br_2}}^{\mathrm{rev}} \ |_{x=0}\ \mathrm{MAPbBr_3}\ |_{x=\mathrm{L}}\ \mathrm{Au\ (blocking)}, a_{\mathrm{Br_2}}^{\mathrm{block}}$$

where, $a_{\mathrm{Br_2}}^{\mathrm{block}}$ represents the Br_2 activity at the interface of $MAPbBr_3$/blocking electrode. Based on Wagner's theory, the partial current, i_j of charge carrier j can be expressed as,

$$i_j = -A\left(\frac{\sigma_j}{Z_j F}\right)\frac{\partial \eta_j}{\partial x}, \tag{3-15}$$

where A and F are electrode area and Faraday constant, σ_j, Z_j, η_j represent the partial conductivity, the valence, and the electrochemical potential of charge carrier j, respectively. In $MAPbBr_3$ materials, bromine ion, electrons and holes are considered as the possible charge carriers, and the partial current contributed by these species were expressed as,

$$i_{\mathrm{Br^-}} = -A\left(-\frac{\sigma_{\mathrm{Br^-}}}{F}\right)\frac{\partial \eta_{\mathrm{Br^-}}}{\partial x}, \tag{3-16}$$

$$i_{\mathrm{n}} = -A\left(-\frac{\sigma_{\mathrm{n}}}{F}\right)\frac{\partial \eta_{\mathrm{n}}}{\partial x}, \tag{3-17}$$

$$i_{\mathrm{p}} = -A\left(\frac{\sigma_{\mathrm{p}}}{F}\right)\frac{\partial \eta_{\mathrm{p}}}{\partial x}, \tag{3-18}$$

where $\mathrm{Br^-}$, n and p represent bromine ion, electrons and holes, respectively. In $MAPbBr_3$ material, the reactions below were considered,

$$\mathrm{Br^-} = \frac{1}{2}\mathrm{Br_2} + \mathrm{e'}, \tag{3-19}$$

$$0 = \mathrm{e'} + \mathrm{h^{\cdot}}. \tag{3-20}$$

The relations between electrochemical potential of bromine ions, electrons and holes can be expressed as,

$$\eta_{\mathrm{Br^-}} = \frac{1}{2}\mu_{\mathrm{Br_2}} + \eta_{\mathrm{n}}, \tag{3-21}$$

$$0 = \eta_{\mathrm{n}} + \eta_{\mathrm{p}}. \tag{3-22}$$

By combining eq. (3-16) and (3-22), the electrochemical potential gradient, $\frac{d\eta_n}{dx}$, can be expressed as follows,

$$\frac{d\eta_n}{dx} = \frac{\sigma_{Br^-}}{2[r(\sigma_n+\sigma_p)-\sigma_{Br^-}]}\frac{d\mu_{Br_2}}{dx}, \tag{3-23}$$

where *r* is the ratio of the partial current contributed by bromide ions to the total current of electrons and holes which is defined as,

$$r = \frac{i_{Br^-}}{i_n+i_p}. \tag{3-24}$$

The partial current of bromide ions, electrons and holes can be rewritten as,

$$i_{Br^-} = \frac{A}{2F}\left(\frac{r(\sigma_n+\sigma_p)\sigma_{Br^-}}{r(\sigma_n+\sigma_p)-\sigma_{Br^-}}\right)\frac{d\mu_{Br_2}}{dx}, \tag{3-25}$$

$$i_n = \frac{A}{2F}\frac{\sigma_n\sigma_{Br^-}}{r(\sigma_n+\sigma_p)-\sigma_{Br^-}}\frac{d\mu_{Br_2}}{dx}, \tag{3-26}$$

$$i_p = \frac{A}{2F}\frac{\sigma_p\sigma_{Br^-}}{r(\sigma_n+\sigma_p)-\sigma_{Br^-}}\frac{d\mu_{Br_2}}{dx}. \tag{3-27}$$

The total current, i_{tot} is expressed as,

$$i_{total} = i_{Br^-} + i_n + i_p, \tag{3-28}$$

Put (3-25), (3-26) and (3-27) into (3-28), the total current can be rearranged as,

$$i_{total} = -\frac{A}{2F}\frac{(r+1)(\sigma_n+\sigma_p)\sigma_{Br^-}}{r(\sigma_n+\sigma_p)-\sigma_{Br^-}}d\mu_{Br_2}, \tag{3-29}$$

When steady-state was achieved during dc polarization in $MAPbBr_3$ materials, integrating from one to the other interface of electrolyte/electrode (from *x*=0 to *x*=L), the following relation could be obtained,

$$i_{total}L = -\frac{A}{2F}\int_{\mu_{Br_2}^{x=0}}^{\mu_{Br_2}^{x=L}}\frac{(r+1)(\sigma_n+\sigma_p)\sigma_{Br^-}}{r(\sigma_n+\sigma_p)-\sigma_{Br^-}}d\mu_{Br_2}, \tag{3-30}$$

The expression could be developed as,

$$\eta_n^{x=L} - \eta_n^{x=0} = -\frac{1}{2}\int_{\mu_{Br_2}^{x=0}}^{\mu_{Br_2}^{x=L}}\frac{\sigma_{Br^-}}{r(\sigma_n+\sigma_p)-\sigma_{Br^-}}d\mu_{Br_2}, \tag{3-31}$$

where $\eta_n^{x=L}$ and $\eta_n^{x=0}$ represent electrochemical potential of electrons at *x*=*L* and *x*=0, respectively. If the same electrode was used at the both side of electrolyte, $\eta_n^{x=L} = \eta_n^{x=0}$, the voltage applied to the cell can be expressed by the electrochemical potential of electrons at the interface of $MAPbBr_3$/electrode as follows.

$$E_{app} = -\frac{1}{F}(\eta_n^{x=L} - \eta_n^{x=0}) = -\frac{1}{2F}\int_{\mu_{Br_2}^{x=0}}^{\mu_{Br_2}^{x=L}}\frac{\sigma_{Br^-}}{r(\sigma_n+\sigma_p)-\sigma_{Br^-}}d\mu_{Br_2} \tag{3-32}$$

If the electrode polarization is neglected, the applied voltage and total current through the cell can be related by the current ratio *r*.

Present research used Hebb-Wagner's asymmetric cell with a reversible electrode, and measured the partial conductivity at the interface of $MAPbBr_3$/blocking electrode. When steady-state was achieved under certain applied voltage, the electrochemical potential gradient of Br_2 through $MAPbBr_3$ should be equal to zero as shown with the following relation (no leakage through blocking electrode was assumed),

$$\frac{\partial \eta_{Br^-}}{\partial x} = 0. \tag{3-33}$$

Under steady-state, $i_{Br^-}=0$, and $r=0$. The total current through the cell can be represented by external current, i_{ext}. The expressions of i_{ext} and E_{app} can be rewritten as,

$$i_{ext} = \frac{A}{2FL}\int_{\mu_{Br_2}^{x=0}}^{\mu_{Br_2}^{x=L}} (\sigma_n + \sigma_p)\, d\mu_{Br_2}, \tag{3-34}$$

$$E = \frac{1}{2F}\int_{\mu_{Br_2}^{x=0}}^{\mu_{Br_2}^{x=L}} d\mu_{Br_2}, \tag{3-35}$$

At the interface of $MAPbBr_3$/blocking electrode, the total electronic conductivity can be expressed as, $\sigma_e^{block} = \sigma_n^{block} + \sigma_p^{block}$ under a certain bromine activity, $a_{Br_2}^{block}$, The partial electronic conductivity can be described as, $\sigma_e^{block} = \frac{L}{A}\frac{di_{ext}}{dE_{app}}$, thus, partial electronic conductivity can be calculated from the differentiation of steady-state current as the calcualtion in section 3.3.1.

The Br_2 activity was expressed by μ_{Br_2} as below,

$$a_{Br_2} = \exp(\frac{\mu_{Br_2} - \mu_{Br_2}^0}{RT}), \tag{3-36}$$

where $\mu_{Br_2}^0$ is the bromine activity under standard state. Thus, E_{app} is rearranged from eq. (3-35) as

$$E_{app} = -\frac{RT}{2F}\ln\frac{a_{Br_2}^{rev}}{a_{Br_2}^{block}}, \tag{3-37}$$

Once the current was interrupted after steady-state was achieved, $i_{tot} = 0$, thus,

$$i_{Br^-} = -(i_n + i_p). \tag{3-38}$$

E_{open} was expressed as,

$$E_{open} = -\frac{1}{2F}\int_{\mu_{Br_2}^{x=0}}^{\mu_{Br_2}^{x=L}} \frac{\sigma_{Br^-}}{\sigma_n+\sigma_p+\sigma_{Br^-}}\, d\mu_{Br_2}, \tag{3-39}$$

The transference number of ions, t_{ion} can be expressed with the ratio of total to partial conductivity as $\sigma_{Br^-}/\sigma_{tot}$, then E_{open} can be rewritten as,

$$E_{open} = \int_{E=0}^{E=E_{app}} t_{Br^-}\, dE, \tag{3-40}$$

Therefore, the ion transference number can be calculated using the equation,

$$t_{\mathrm{Br}^-} = \frac{\partial E_{\mathrm{open}}}{\partial E_{\mathrm{app}}}, \tag{3-41}$$

The relations have been used to estimate the ion transference number in section 3.3.2.

3.4.2 Defect Chemistry Model

In $MAPbBr_3$ materials, the full Schottky disorder can be expressed in the following reaction using Kröger-Vink notation.

$$\mathrm{nil} \rightarrow \mathrm{V}'_{\mathrm{MA}} + \mathrm{V}''_{\mathrm{Pb}} + 3\mathrm{V}^{\cdot}_{\mathrm{Br}} + \mathrm{MAPbBr_3}, \tag{3-42}$$

where nil represents the perfect lattice of perovskite. To explain the variation of partial conductivity with Br_2 activity, present work introduced a simple but practical defect chemical model which can be summarized as follows: The equilibrium constant for the formation of bromine vacancy ($\mathrm{V}^{\cdot}_{\mathrm{Br}}$),

$$\mathrm{Br}^{\times}_{\mathrm{Br}} \rightarrow \mathrm{V}^{\cdot}_{\mathrm{Br}} + \tfrac{1}{2}\mathrm{Br}_2 + \mathrm{e}', \tag{3-43}$$

can be expressed as,

$$K_{\mathrm{V_{Br}}} = [\mathrm{V}^{\cdot}_{\mathrm{Br}}] n a^{1/2}_{\mathrm{Br_2}}. \tag{3-44}$$

For the intrinsic ionization of elelctrons and holes,

$$\mathrm{nil} \rightarrow \mathrm{e}' + \mathrm{h}^{\cdot}, \tag{3-45}$$

The equilibrium constant expressed as,

$$K_{\mathrm{i}} = np, \tag{3-46}$$

where $[\mathrm{V}^{\cdot}_{\mathrm{Br}}]$ is the concentration of $\mathrm{V}^{\cdot}_{\mathrm{Br}}$, and n and p are the concentration of the free electrons (e') and holes ($\mathrm{h}^{\cdot}$), respectively. The overall charge neutrality condition can be expressed as,

$$\mathrm{n} + [\mathrm{V}'_{\mathrm{MA}}] + 2[\mathrm{V}''_{\mathrm{Pb}}] = [\mathrm{V}^{\cdot}_{\mathrm{Br}}] + \mathrm{p}, \tag{3-47}$$

where $[\mathrm{V}'_{\mathrm{MA}}]$ and $[\mathrm{V}''_{\mathrm{Pb}}]$ are the concentration of $\mathrm{V}'_{\mathrm{MA}}$ and $\mathrm{V}''_{\mathrm{Pb}}$, respectively.

The defect chemisty of $MAPbBr_3$ perovskites depends on A/B ratio and Br nonstoichiometry. A/B ratio is a certain value that will be determined by the preparation process. The concentration of $\mathrm{V}'_{\mathrm{MA}}$ is reported as being much higher compared with $\mathrm{V}''_{\mathrm{Pb}}$ in $MAPbBr_3$ [17]. As the mobility of A- and B- site vacancy are estimated to be much smaller than Br vacancy, it is reasonable to assume $\mathrm{V}'_{\mathrm{MA}}$ and $2\mathrm{V}''_{\mathrm{Pb}}$ as 'frozen' vacancies, which is independent of Br_2 activity (refer to the discussion in Chapter 2). This fixed concentration is defined as $\alpha_0 = [\mathrm{V}'_{\mathrm{MA}}] + 2[\mathrm{V}''_{\mathrm{Pb}}]$, and the neutrality condition can be rewritten as follows.

$$n + \alpha_0 = [V_{Br}^{\cdot}] + p. \quad (3\text{-}48)$$

The simulation of defects concentration as a function of a_{Br_2} based on the defect model above was shown in Fig. 3-14 (a). At high a_{Br_2} region corresponding to *p*-type domain, $h^{\cdot}$ is compensated by cationic vacancies, $[V'_{MA}] + 2[V''_{Pb}]$, leading to *p* being saturated at a constant value of α_0. In the intrinsic region, since total concentration of frozen cationic vacancies is also constant expressed as $[V_{Br}^{\cdot}] = [V'_{MA}] + 2[V''_{Pb}]$, *n* and *p* exhibit -1/2 and 1/2 power dependency to a_{Br_2}, respectively. At low a_{Br_2} region under increased *n* conditions, e' is compensated by the predominant defect of $V_{Br}^{\cdot}$. In this model, although the concentration of electrons shall exhibit 1/4 power dependence to a_{Br_2} in reducing region, no *n*-type domain could be observed in present experiment owning to *n* saturation at a certain low value. Therefore, another possible defect equilibrium should be taken into account in reduced Br_2 activity domain.

Shi *et al*. [18] calculated the formation energies of $V_{Br}^{\cdot}$, V_{Br}, and V'_{Br} with the variation of Fermi level in $CsPbBr_3$ perovskites, and found a $V_{Br}^{\cdot}$-to-V'_{Br} transition at 0.05 eV just below the conduction band minimum (CBM), which indicated V'_{Br} can be stabilized as a shallow donor state under reducing conditions (as shown in Fig. 3-15). Since the defect chemical nature of the $MAPbBr_3$ is quite similar with the inorganic perovskite containing the same halogen ions, it is reasonable to assume V'_{Br} as the predominant defect, which compensates $V_{Br}^{\cdot}$ at the low a_{Br_2} region in the $MAPbBr_3$ system. The dependences of defect concentrations, estimated by employing the concentration of V'_{Br} and $V_{Br}^{\cdot}$, can be deduced by the following equations.

$$V'_{Br} \rightarrow V_{Br}^{\cdot} + 2e', \quad (3\text{-}49)$$

$$K'_{V_{Br}} = [V_{Br}^{\cdot}]n^2/[V'_{Br}], \quad (3\text{-}50)$$

where $K'_{V_{Br}}$ is the equilibrium constant of reaction (3-49). The overall charge neutrality condition can be rewritten as,

$$[V'_{Br}] + n + \alpha_0 = [V_{Br}^{\cdot}] + p, \quad (3\text{-}51)$$

As shown in Fig. 3-14 (b), the concentration of $V_{Br}^{'}$ and $V_{Br}^{\cdot}$ exhibit 1/2 power dependency to a_{Br_2} in low a_{Br_2} region, and the free electron density shows a constant value. The $K_{V_{Br}}^{'}$ exhibits strong dependency on free electron density under saturation, and was estimated to be around 10^9 using current model. Meanwhile, the equilibrium constant parameters, $K_{V_{Br}} = 10^{-24}$, $K_i = 10^{-22}$, and the concentration of the "frozen"

defects, $\alpha_0 = 10^{-4}$. Current defect model indicated a broad a_{Br_2} region in which the ionic conductivity should be domainant even if under extremely reducing conditions.

Fig. 3-16 supplements the simulation results using current defect model by adjusting the equilibrium constant, $K'_{V_{Br}}$. From (a) to (d), $K'_{V_{Br}}$ was set as 10^6, 10^{12}, 10^{18}, 10^{22}, respectively. As $K'_{V_{Br}}$ increasing, the saturated concentration of electrons in reducing region will gradually decrease, and eventually reduced to the same concentration with that of holes. The partial conductivities obtained from polarization experiments suggested electrons saturated at a much lower concentration by more than one order of magnitude compared with holes, a reasonable estimation of $K'_{V_{Br}}$ should be around 10^9 which is in well agreement with the partial conductivity data.

Above all, the defect chemistry model introduced can well describe the results of the polarization experiment, and confirm $MAPbBr_3$ material seems more like an ion conductor than semiconductor in a wide Br_2 activities domain.

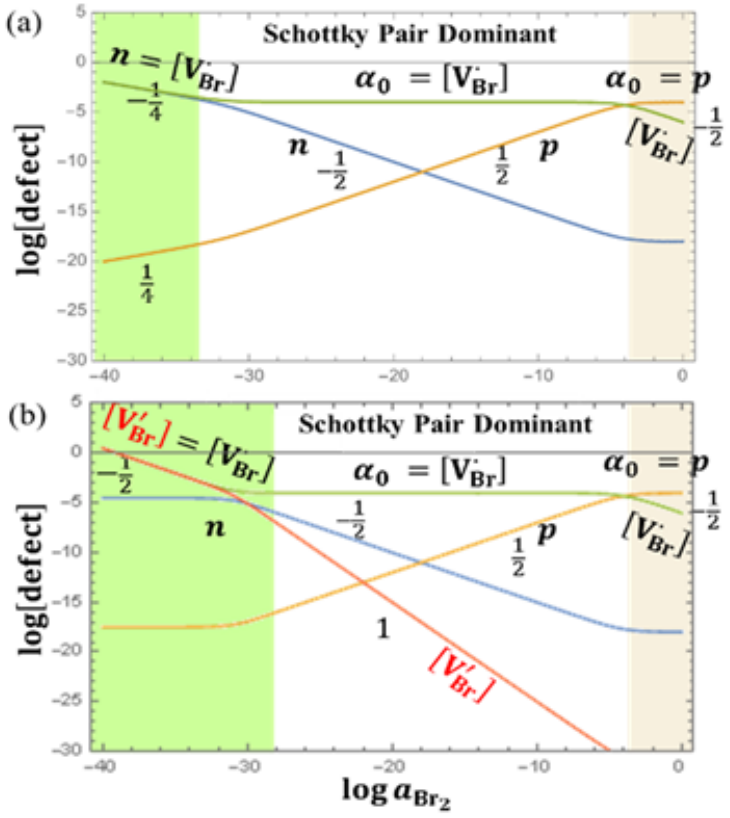

Fig. 3-14 Brower diagram for the $MAPbBr_3$ system with (a) charge neutrality condition with $\mathbf{n} + \boldsymbol{\alpha_0} = [\mathbf{V_{Br}^{\cdot}}] + \mathbf{p}$, where *n*-type domain appears at low $\boldsymbol{a_{Br_2}}$ region,

(b) charge neutrality condition with $[\mathbf{V_{Br}^{'}}] + \mathbf{n} + \boldsymbol{\alpha_0} = [\mathbf{V_{Br}^{\cdot}}] + \mathbf{p}$, where ionic defect is dominant at low $\boldsymbol{a_{Br_2}}$ region.

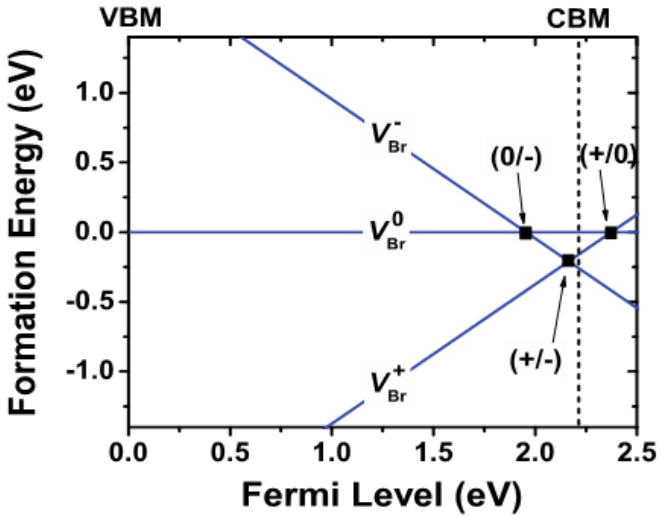

Fig. 3-15 The halide vacancy formation energy for $CsPbBr_3$ system [18].

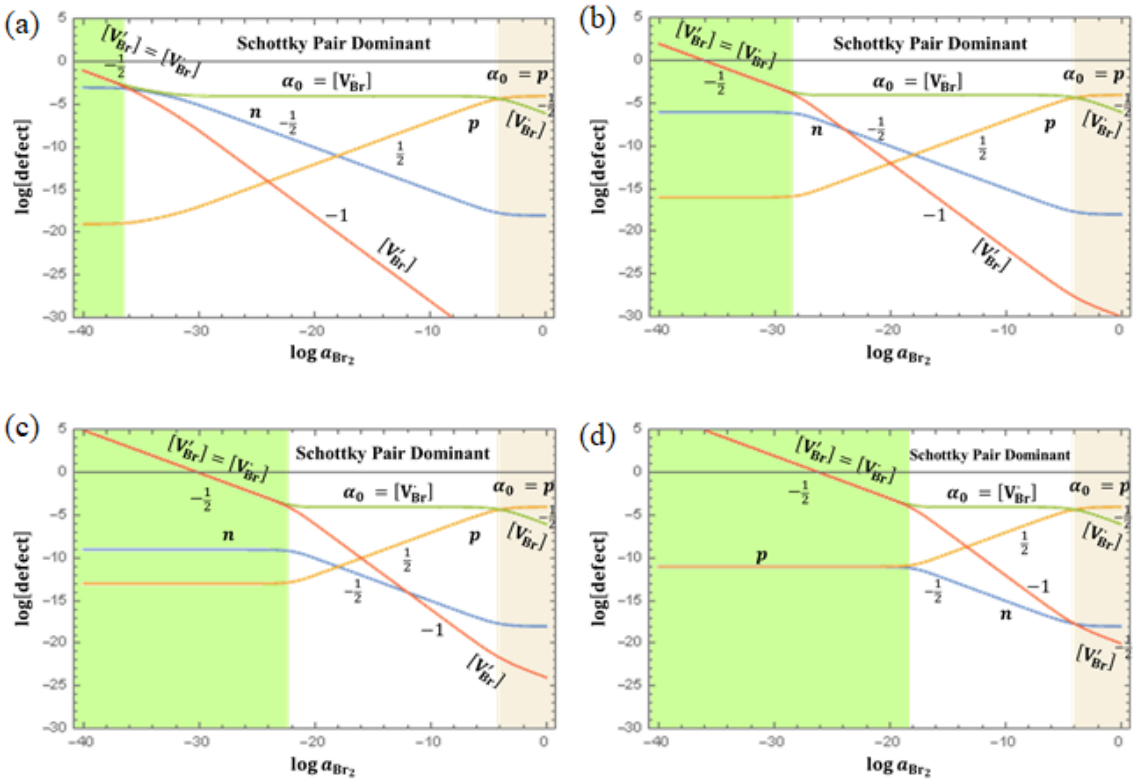

Fig. 3-16 Brower diagram for the $MAPbBr_3$ system with charge neutrality condition with $[\mathbf{V_{Br}^{'}}] + \mathbf{n} + \boldsymbol{\alpha_0} = [\mathbf{V_{Br}^{\cdot}}] + \mathbf{p}$, where equilibrium constant of electron trapping formation, $\boldsymbol{K_{V_{Br}}^{'}}$. From (a) to (d), $\boldsymbol{K_{V_{Br}}^{'}}$ was set 10^6, 10^{12}, 10^{18}, 10^{22}, respectively.

3.4.3 Band Gap Estimation

The band gap of $MAPbBr_3$ can be estimated from the *p*/*n* transition point corresponding to $\sigma_p = \sigma_n$ as shown in Fig. 3-17. For the intrinsic semiconductor, the concentration of electrons and holes can be calculated from the band theory,

$$n = p = 2\left(\frac{2\pi k}{h^2}\right)^{3/2}(m_e^* + m_h^*)^{3/4}T^{3/2}\exp\left(-\frac{E_g}{2kT}\right), \quad (3\text{-}52)$$

where m_e^* and m_h^* are the effective mass of the electrons and holes at conduction band maximum (CBM) and valence band minimum (VBM), respectively. E_g is the band gap of the material, k is the Boltzmann constant, h is the Planck constant, T is the temperature in Kelvin. The total electronic conductivity can be expressed as,

$$\sigma_{et} = en\mu_n + ep\mu_p = 2e\left(\frac{2\pi k}{h^2}\right)^{3/2}(m_e^* + m_h^*)^{3/4}T^{3/2}\exp\left(-\frac{E_g}{2kT}\right)(\mu_n + \mu_p). \quad (3\text{-}53)$$

If the free electron gas approximation is assumed, μ_n and μ_p should be proportional to $T^{-3/2}$, and σ_{et} can be expressed as,

$$\sigma_{et} = 2e\left(\frac{2\pi k}{h^2}\right)^{\frac{3}{2}}(m_e^* + m_h^*)^{\frac{3}{4}}\exp\left(-\frac{E_g}{2kT}\right)(a_n + \alpha_p), \quad (3\text{-}54)$$

where α_n and α_p are the pre-exponential factors for μ_n and μ_p, respectively. However, when the intersection between the lattice and the electrons becomes significant due to the orbital overlap, a typical "large polarons" case should be considered in the materials, where $\mu \propto T^{-1/2}$ is often found for large polarons. σ_{et} is expressed as,

$$\sigma_{et} = 2e\left(\frac{2\pi k}{h^2}\right)^{\frac{3}{2}}(m_e^* + m_h^*)^{\frac{3}{4}}T\exp\left(-\frac{E_g}{2kT}\right)(\alpha_n' + \alpha_p'), \quad (3\text{-}55)$$

where α_n' and α_p' are the pre-exponential factors of μ_n and μ_p in large polarons case, respectively. The band gap was estimated to be about 1.29 eV by free electron gas approximation and 1.24 eV by large polaron approximation discussed above. Previous researches reported the band gap of $MAPbBr_3$ is about 2.2 eV measured by UV-visible spectra [10], and the reduction of the band gap estimated in present work may due to possible in-gap state induced by the high concentration of ionic defects.

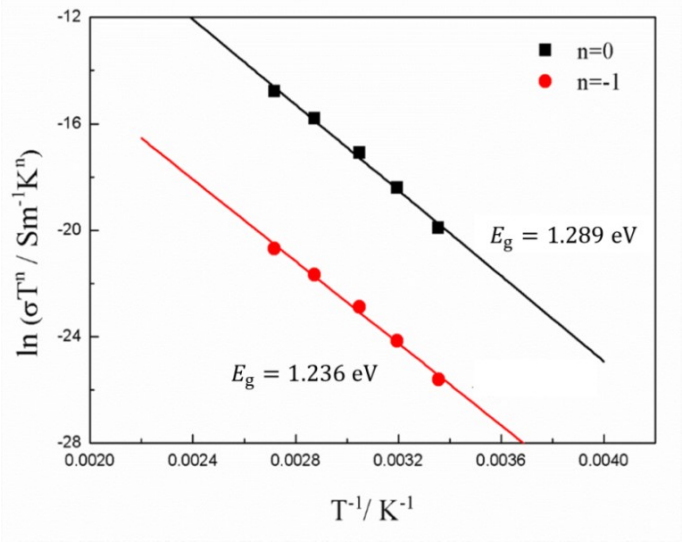

Fig. 3-17 Arrhenius relationship of electronic conductivities of *p*/*n* transition point ($\boldsymbol{\sigma_p = \sigma_n}$) from the polarization curves in Fig. 3-3. The band gap was estimated based on free electron gas approximation (n=0) and large polaron approximation (n=-1).

3.4.4 Electrochemical Stability Window

The partial conductivities and ion transference number measured by dc polarization indicates the predominance of ionic carrier in $MAPbBr_3$ materials that means the system is almost a pure electrochemical system. Thus, the chemical stability under applied bias voltage or generated photo-voltage is governed by the electrochemical window. Detailed discussion will be delivered with possible stabilization strategy of the materials based on the present results.

The electrochemical stability window and the conductivity domain of $MAPbBr_3$ perovskite materials under different temperatures were estimated from σ_e and t_{ion} data shown in Fig. 3-3. Since the $MAPbBr_3$ materials can be considered as electrolyte, on which the bias voltage applied that will caused decomposition is determined by the chemical potential gradient generated through the electrolyte. The *emf* of the cell using electrodes with different a_{Br_2} on both sides, can be expressed by Nernst's equation as follows,

$$emf = -\frac{\Delta_r G^\theta}{2F} = -\frac{\mu_{Br_2}^- - \mu_{Br_2}^+}{2F} = -\frac{RT}{2F}\ln\frac{a_{Br_2}^-}{a_{Br_2}^+}, \quad (3\text{-}56)$$

where $\Delta_r G^\theta$ is the standard Gibbs formation energy change of the Br_2 concentration cell using $MAPbBr_3$ as electrolyte, the reaction on the electrode can be expressed as,

$$\mathrm{Br_2}\left(a^{+}_{\mathrm{Br_2}}\right) \rightarrow \mathrm{Br_2}(a^{-}_{\mathrm{Br_2}}). \quad (3\text{-}57)$$

If pure liquid Br_2 was used as a reference electrode, $\mu^{+}_{\mathrm{Br_2}} = 0$, the *emf* of the Br_2 concentration cell will be determined by the chemical potential of Br_2 at the interface of $MAPbBr_3$/electrode. When $MAPbBr_3$ start to decompose and precipitate Br_2 at the interface of $MAPbBr_3$/electrode, $a_{\mathrm{Br_2}} = 1$, corresponding $emf^{+} = 0\mathrm{V}$ (shown with red dashed line in Fig. 3-18). The electrochemical window could be estimated by the minimum $a_{\mathrm{Br_2}}$ value required to maintain the integrity of the material compared with $a^{+}_{\mathrm{Br_2}}$=1 under oxidizing conditions.

Detailed thermodynamic stability data of the $MAPbBr_3$ is not available at the moment, but an approximated calculation could be given in present work. The thermodynamic properties of $MAPbBr_3$ materials is determined by any two activity parameters among a_{MABr}, $a_{\mathrm{PbBr_2}}$ and $a_{\mathrm{Br_2}}$. The following two conditions will be discussed, 1) $PbBr_2$-rich ($a_{\mathrm{PbBr_2}} > a_{\mathrm{MABr}}$), and 2) MABr-rich ($a_{\mathrm{PbBr_2}} < a_{\mathrm{MABr}}$). Under $PbBr_2$-rich condition, when $MAPbBr_3$ start to decompose and precipitate Pb at the interface of $MAPbBr_3$/electrode, the *emf* can be rearranged from (3-56),

$$emf = -\frac{\Delta_{\mathrm{r}}G^{\theta}}{2F} = -\frac{RT}{2F}\ln\frac{a_{\mathrm{PbBr_2}}}{a_{\mathrm{Pb}}a^{1}_{\mathrm{Br_2}}} = -\frac{RT}{2F}\ln a^{1}_{\mathrm{Br_2}}, \quad (3\text{-}58)$$

where $\Delta_{\mathrm{r}}G^{\theta}$ is the standard Gibbs formation energy of the equation, $\mathrm{Pb} + \mathrm{Br_2} \rightarrow \mathrm{PbBr_2}$, $a^{1}_{\mathrm{Br_2}}$ is the Br_2 activity at the interface of $MAPbBr_3$/electrode, $a_{\mathrm{PbBr_2}} = 1$, $a_{\mathrm{Pb}} = 1$ under this condition. The electrochemical window under $PbBr_2$-rich condition can be estimated to be 1.36 eV calculated from ΔG^{θ} in eq. (3-58).

The formation of $MAPbBr_3$ was expressed as,

$$\mathrm{MAPbBr_3} \rightarrow \mathrm{MABr} + \mathrm{PbBr_2}, \quad (3\text{-}59)$$

$$K_{\mathrm{f}} = (a_{\mathrm{MABr}}a_{\mathrm{PbBr_2}})/a_{\mathrm{MAPbBr_3}}, \quad (3\text{-}60)$$

where K_{f} is the equilibrium constant of eq.(3-59). The $a_{\mathrm{Br_2}}$ decreases with the decreasing of $a_{\mathrm{PbBr_2}}$ during Pb precipitation (eq. (3-58)), and the $a_{\mathrm{PbBr_2}}$ is inversely proportional to a_{MABr} (eq. (3-60)), thus, $a_{\mathrm{Br_2}}$ should be proportional to a_{MABr} at a certain temperature. The minimum $a_{\mathrm{Br_2}}$ required to maintain the integrity of the material could be expected when a_{MABr} reach the maximum value. The electrochemical window estimated will be somewhat wider in MABr-rich condition, which is governed by the Gibbs formation energy, $\Delta_{\mathrm{r}}G^{0}$, of eq. (3-59). Ivanov *et al.* [19] report a small value of $\Delta_{\mathrm{r}}G^{0} \approx 18.4$ KJ, which corresponds to 0.10v increase of *emf* during Pb

precipitation as shown with dashed line in Fig. 3-17. The calculation suggests the electrochemical window is about 1.36 eV~1.46 eV, which is far below the band gap of $MAPbBr_3$ (2.2eV). This narrow electrochemical window limits the voltage applied on the $MAPbBr_3$ materials, otherwise, the materials will be decomposed due to over potential.

The conductivity domains of $MAPbBr_3$ materials under different temperatures were shown in Fig. 3-18 with the solid red lines. The transition a_{Br_2} from ionic dominant to *p*-type domain was estimated from the ion transference number, t_{ion}=0.5 (Fig. 3-6), and the corresponding *emf* is defined as $E_{\oplus}$ (with red dots). The *emf* corresponding to *n*/*p* switching is defined as $E_{n/p}$ (with blue dots) which was obtained from the partial conductivity curves (Fig. 3-3). Since the possible *n*-type domain at very low a_{Br_2} could not be observed in present experiment, no $E_{\ominus}$ could be estimated corresponding to the transition from ionic dominant to *n*-type domain.

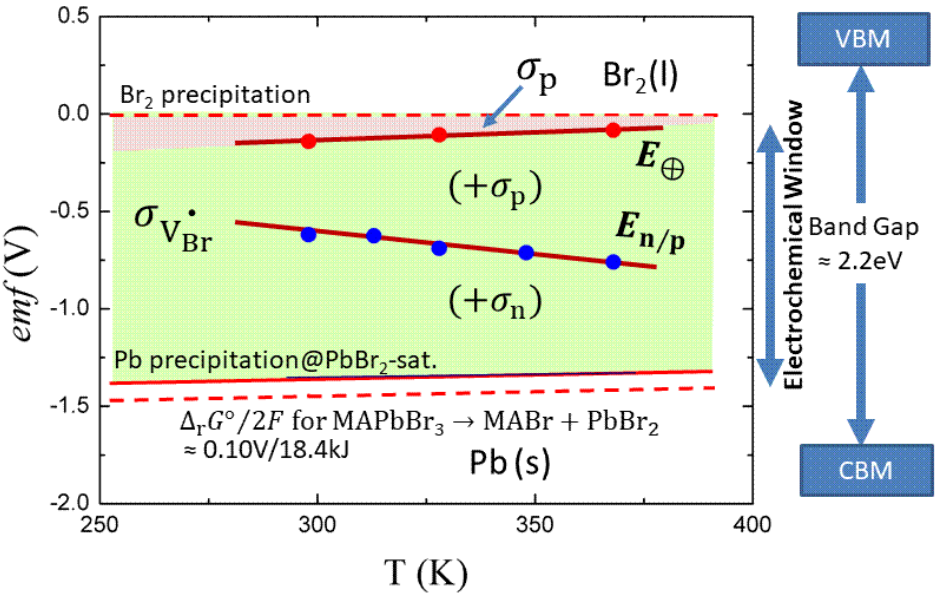

Fig. 3-18 Electrochemical window and the conductivity domain of $MAPbBr_3$.

The stability issue of materials is the important factor that restricts the outdoor applications of perovskite solar cells. There are three directions to increase the stability, 1) A-site mixing, 2) B-site mixing, and 3) anionic mixing. For 1), $FAPbI_3$ was reported to exhibit better long-term stability than $MAPbI_3$, and functions continuously for thousands of hours under illumination, which provided a possibility of FA^+/MA^+ mixing that may enhance the stability of the materials [20-22]. For 2), the possible way to

strengthen the stability is combine PbI_2 with SnI_2 to form $MASn_xPb_{1-x}I_3$ with a band gap of 1.15~1.55 eV, however, Sn^{2+} can be easily changed to Sn^{4+} exposed to ambient atmosphere [7, 23]. 3) is the most reported method: The stability of $MAPbI_3$ can be significant improved by mixing with Br, as $MAPb(I_{1-x}Br_x)_3$, and maintained their photo-electrical conversion efficiency at x=0.2, 0.29 [24]. I/Cl mixing perovksites were reported to exhibit remarkable stability to moisture, light and temperature [22]. $MAPbBr_{3-x}Cl_x$ materials also exhibit less sensitive to ambient atmosphere, no obvious degradation was observed after exposed for 30 days, indicating a good stability [24, 25]. Although the mechanism behind has not yet been fully understood, we believe the thermodynamic activity of halides will be significant reduced by A-site, B-site, and anionic mixing, thus, enhance the stability of perovskite materials.

3.5 Summary

The partial conductivities of electrons and holes of $MAPbBr_3$ perovskite single crystals have been measured by Hebb-Wagner dc polarization with the variation of a_{Br_2} at the temperature of RT~95 °C using an asymmetric cell with an ion blocking electrode and reversible electrode. The transference number of ions was measured by current interruption technique after steady-state was achieved during dc polarization. An annealing method was used to control a_{Br_2} of single crystals under $PbBr_2$-rich condition, and the total conductivities of these crystals were measured by ac impedance method. The possible defect chemicstry model was discussed in this chapter based on the partial Schottky disorder, and some thermodynamic data was also roughly estimated by simulation. The electrochemical window was discussed in detail based on the possible stability strategy of $MAPbBr_3$ system.

A p to n transition upon variation of a_{Br_2} was observed, however, it is confirmed that the partial ionic conductivity is dominate in a wide range of stability domain. The increasing of total conductivity was related to the enhancement of partial electronic conductivity in p-type domain. Discussion about defect chemistry was made employing simplified partial Schottky model with frozen vacancies of A-site and B-site and the presence of electron trapping by Br vacancy.

The band gap of $MAPbBr_3$ was estimated to be 1.3 eV from *p*/*n* switching point, which is narrow compared with the band gap measured by UV-visible spectra (2.2 eV) somewhere, which may due to the existence of possible in-gap defect states.

The predominance of ionic carrier means that the system is almost a pure electrochemical system that the stability of the system under bias voltage or photo-generated voltage is governed by the electrochemical window, which was estimated to be 1.36~1.46 V based on the calculation of the thermodynamic properties of $MAPbBr_3$, leading to the stability domains of the system narrower than the intrinsic band gap.

Systemic research of the partial conductivities controlled by chemical potential of the components will be helpful for understanding the defect chemistry of $MAPbBr_3$ perovskite materials and evaluating the comprehensive performance for industrial application. Present work will be helpful to further investigation on photo-electrochemical properties of $MAPbX_3$ materials based on the defect chemistry discussed in this chapter.

3.6 Reference

[1] Haruyama J, Sodeyama K. *et al*. First-principles study of ion diffusion in perovskite solar cell sensitizers. *J. Am. Chem. Soc.,* 137**,** 10048–10051 (2015).

[2] Yuan Y, Huang J. Ion migration in organometal trihalide perovskite and its impact on photovoltaic efficiency and stability. *Acc. Chem. Res.,* 49**,** 286–293 (2016).

[3] Azpiroz JM, Bisquert J. Defects migration in methylammonium lead iodide and their role in perovskite solar cells operation. *Energy Environ., Sci.* 8, 2118-2127 (2015).

[4] Meloni S, Moehl T, Tress W, *et al*. Ionic polarization-induced current–voltage hysteresis in $CH_3NH_3PbX_3$ perovskite solar cells. *Nat. commun.*, 7: 10334 (2016).

[5] Kim J, Lee SH, *et al*. The role of intrinsic defects in methylammonium lead iodide perovskite. *J. Phys. Chem. Lett.,* 5**,** 1312–1317 (2014).

[6] Eperon GE, Stranks SD, *et al*. Environmental science formamidinium lead trihalide : a broadly tunable perovskite for efficient planar heterojunction solar. *Energy Environ Sci*., **7**, 982-988 (2014).

[7] Stoumpos CC, Malliakas CD, *et al*. Semiconducting tin and lead iodide perovskites with organic cations: phase transitions, high mobilities, and near-infrared photoluminescent properties. *Inorg. Chem.,* 52**,** 9019–9038 (2013).

[8] Aono H, Sugimoto E. Br^{-1} ionic conductivity for $PbBr_2$-based solid electrolyte. *Chem. Mater*., **7**, 1233-1236 (1995).

[9] Kobayashi K, Kai Y, *et al*. Electronic conductivity measurements of 5 mol% TiO_2-doped YSZ by a d.c.-polarization technique. *Solid State Ionics,* 93**,** 193–199 (1997).

[10] Shi D, Adinolfi V, Comin R, *et al*. Low trap-state density and long carrier diffusion in organolead trihalide perovskite single crystals. *Science,* 347(6221): 519-522 (2015).

[11] Kobayashi K, Kai Y, *et al*. Partial Conductivity of YSZ Doped with 10 mol% TiO_2. *J. Korean Ceram*., 4, 114-121 (1998).

[12] Baikie T, Barrow NS, *et al*. A combined single crystal neutron/X-ray diffraction and solid-state nuclear magnetic resonance study of the hybrid perovskites $CH_3NH_3PbX_3$ (X= I, Br and Cl). *J. Mater. Chem. A Mater. energy Sustain.,* 3**,** 9298–9307 (2015).

[13] Hebb MH. Electrical conductivity of silver sulfide. *J chem.. phys.,* 20(1): 185-190 (1952).

[14] Wagner JB, Wagner C. Electrical conductivity measurements on cuprous halides. *J Chem. Phys.,* 26(6): 1597-1601 (1957).

[15] Wagner C, *Proc. 7th. Intern. Conf. Electrochem. Thermodyn. Kinetics*, Lindau, 1955 (Butterworth, London, 1965) pp.185.

[16] Choudhury NS, Patterson JW. Performance characteristics of solid electrolytes under steady-state conditions. *J Electrochem. Soc*., 118(9): 1398-1403 (1971).

[17] Walsh A, Scanlon DO, Chen S, *et al*. Self-regulation mechanism for charged point defects in hybrid halide perovskites. *Angew*. *Chem. Int. Edit.,* 54(6): 1791-1794 (2015).

[18] Shi H. Du MH. Shallow halogen vacancies in halide optoelectronic materials. *Phys. Rev. B,* 90**,** 174103 (2014).

[19] Ivanov IL, Steparuk AS, Bolyachkina MS, *et al*. Thermodynamics of formation of hybrid perovskite-type methylammonium lead halides. *J. Chem. Thermodyn*., 116: 253-258 (2018).

[20] Eperon GE, Stranks SD, Menelaou C, *et al*. Formamidinium lead trihalide: a broadly tunable perovskite for efficient planar heterojunction solar cells. *Energ. Environ Sci*., 7(3): 982-988 (2014).

[21] Burschka J, Pellet N, Moon SJ, *et al*. Sequential deposition as a route to high-performance perovskite-sensitized solar cells. *Nature,* 499(7458): 316 (2013).

[22] Leijtens T, Eperon GE, Pathak S, *et al*. Overcoming ultraviolet light instability of sensitized TiO_2 with meso-superstructured organometal tri-halide perovskite solar cells. *Nat. commun*., 4: 2885 (2013).

[23] Hao F, Stoumpos CC, Chang RPH, *et al*. Anomalous band gap behavior in mixed Sn and Pb perovskites enables broadening of absorption spectrum in solar cells. *J Am. Chem. Soc.,* 136(22): 8094-8099 (2014).

[24] Noh JH, Im SH, *et al*. Chemical management for colorful, efficient, and stable inorganic–organic hybrid nanostructured solar cells. *Nano lett.,* 13, 1764-1769 (2013).

[25] Lee MM, Teuscher J, Miyasaka T, *et al*. Efficient hybrid solar cells based on meso-superstructured organometal halide perovskites. *Science*, 2012: 1228604.

CHAPTER 4

Partial and Total Conductivities of $MAPbI_3$ Single Crystals

4.1 Introduction

As a promising photovoltaic material, $MAPbI_3$ materials draw extraordinary attentions recent years because of its excellent optical and electrical transport properties. Yang *et al*. [1] have found the ionic conductivity in $MAPbI_3$ materials is predominant in dark condition, and an ion transference number above 0.5 was reported indicating the significance of ionic conduction in hybrid perovskite materials. Impedance spectroscopy studies also suggested the hybrid perovskites exhibit ionic charge transport in addition to electronic conduction, the details of partial conductivity of holes and electrons are still lack of investigation [2].

In this chapter, the partial electronic conductivities of $MAPbI_3$ perovskite single crystals with tetragonal symmetry have been measured by Hebb-Wagner dc polarization under the temperature range of 25°C~45°C. Different from $MAPbBr_3$ materials, $MAPbI_3$ is a typical quaternary system, which means, besides PbI_2 and I_2, the chemical potential of H_2 should also be carefully controlled to fix the state of the entire system during long-term polarizations. The transference number of ions was estimated by *emf* measurement under steady-state generated by the chemical potential gradient of I_2, μ_{I_2}, through $MAPbI_3$ that controlled by the applied voltage, E_{app}, on an I^- ion conductor. A *p*/*n* transition was observed at a relatively lower I_2 activity range compared with $MAPbBr_3$ materials, and ion transference number also confirmed the presence of *p*-type domain, however, no *n*-type domain but an ion dominant domain due to electron trapping could be observed in very low I_2 activity.

The total conductivities of single crystals with different iodine activity were measured by ac impedance method. Furthermore, ac impedance spectra of several cells consisted of symmetric electrodes with different iodine activity were recorded during annealing, and the total conductivities were obtained after steady-state was attained, with this method, we could estimate the total conductivity at certain iodine activity with selective electrodes. The defect chemistry in $MAPbI_3$ perovskite was also discussed in

this chapter based on the frozen vacancy of A- and B- site and the presence of electron trapping.

In present work, electrochemical transport and defect chemical properties of $MAPbI_3$ materials were systematically investigated which will be helpful for understanding the defect chemistry of organo-lead trihalide hybrid perovskites.

4.2 Experimental

4.2.1 Asymmetric Cell for Polarization

An asymmetric cell with an ion blocking electrode as well as a reversible electrode was used to conduct Hebb-Wagner dc polarization of $MAPbI_3$ single crystals. In present work, thin carbon film (~100 nm) deposited on the crystals surface with carefully ground and polished by sputtering was used as ion blocking electrode, and then covered by a dense Au film to prevent the possible leakage of ions during polarization.

It is well known that small amount of P2VP can render iodine conductivity, and the heated mixture of P2VP-I_2 has been used as cathode electrode in some lithium batteries for long-term low-rate applications, the ion transference number was estimated below 0.1 [3, 4]. Since the vapor pressure of the complex is very close to that of I_2, P2VP-I_2 is considered as a good I_2 electrode that can be used as reversible electrode in present experiment. A tarry two-phase mixture of I_2 and P2VP with high viscosity was prepared with the weight ratio of I_2 to organic component of 7:1. The total conductivity of P2VP-I_2 complex was estimated to be 7.96×10^{-2} Sm^{-1} by ac impedance spectra, and the transference number of iodine ions was estimated to be 0.09 by dc polarization method conducted with two parallel carbon electrodes. Small amount of $MAPbI_3$ powder were mixed into the P2VP-I_2 complex to promote the equilibrium of each component in reversible electrode.

The schematic diagram of the asymmetric cell for polarization was shown in Fig. 4-1, in which the thickness of single crystal, L, is 1 mm, and the electrode area, A, is 11.95 mm^2 (cell constant L/A is 0.837 cm^{-1}).

Since graphite is an inert electrode, the iodine ion activity at the interface of $MAPbI_3$/C is totally determined by the applied voltage, E_{app}, and the iodine activity at the interface of $MAPbI_3$/P2VP-I_2 could be estimated using an I_2 concentration cell. The $0.97PbI_2\cdot0.03NaI$ solid solution was used as electrolyte, the mixture of PdI_2/Pd as a

reference electrode which provides a fixed a_{I_2}, and P2VP-I_2 was used as counter electrode. The *emf* through the I_2 concentration cell was recorded at room temperature. The a_{I_2} of reference electrode was determined by the equation as follows,

$$Pd + I_2 = PdI_2, \quad (4\text{-}1)$$

$$K = a_{PdI_2}/a_{Pd}a_{I_2}, \quad (4\text{-}2)$$

where K is the equilibrium constant of the reaction (4-1), a_{I_2} represents the iodine activity at the interface between $0.97PbI_2 \cdot 0.03NaI$ and PdI_2/Pd, and in eq. (4-2), $a_{PdI_2} = 1$, $a_{Pd} = 1$. The a_{I_2} was determined by equilibrium constant of the reaction which was calculated using the software HSC chemistry 6 (Outotec), K=12.437 at 25°C, corresponds to $a_{I_2} = 10^{-12.437}$.

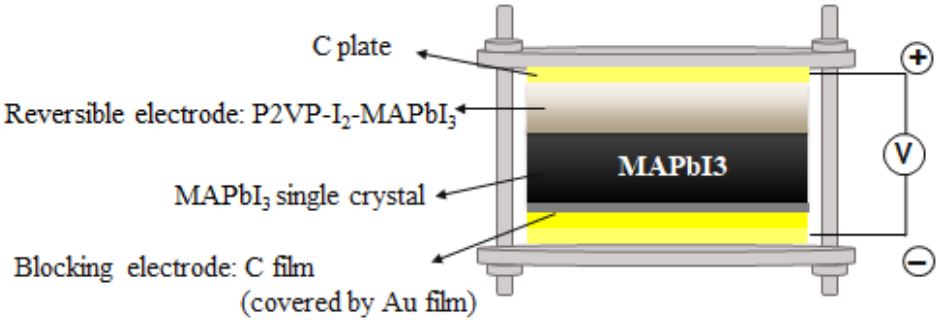

Fig. 4-1 The asymmetric cell for polarization using carbon film (covered with thick Au film) as ion blocking electrode and P2VP/I_2/$MAPbI_3$ as reversible electrode.

4.2.2 Dc Polarization Method

$MAPbI_3$ materials were reported to undergo phase transition from tetragonal perovskite to cubic at higher temperature (≈54~57 °C), and also a clear reduction on intensity of {211} reflections in XRD pattern at 55 °C was observed in present work (see Fig. 2-6 in Chapter 2) which also suggested a tetragonal/cubic transition. Therefore, dc polarization were performed at 25 °C, 30 °C, 35 °C, 40 °C, 45 °C under controlled I_2 activity at the interface of $MAPbI_3$/reversible electrode, $a_{I_2}^{rev}$ to avoid the affect due to difference of electronic conductivity during transition to cubic perovskite phase.

The potentiostatic dc polarization was conducted using an Ivium station (CompactStat B10060, Ivium Technologies, Netherlands) by applying voltage range

from 0.1V to 0.88V between two parallel carbon plate, and the value of current i_{ext} under different applied voltage E_{app} was recorded after the steady state was achieved.

The measurements were conducted under the mixed gas atmosphere of 5% H_2 and 95% Ar (in volume fraction). It is because, the equilibrium vapor pressure of HI is very low, supplying H_2 will effectively inhibit the decomposition of $MAPbI_3$ materials, thus, the chemical potential of H_2 should be carefully controlled to fix the state of $MAPbI_3$ material (refer to the chemical stability in Chapter 2). All the measurements were conducted under dark condition to exclude the contribution of photo-excited electrons.

4.2.3 Ion Transference Number Measurement

Since the electronic conductivity is expected to be much higher than ionic conduction in $MAPbI_3$ materials, here we used *emf* measurement under steady-state to estimate the transference number of iodine ions at different temperatures.

The *emf* measurement was conducted between the two poles of $MAPbI_3$ single crystals, and the schematic diagram of the concentration cell for measurement was shown in Fig. 4-2. It has been reported that the ionic conductivity of PbI_2 was significantly improved by doping small amount of NaI, thus, the solid solution of $(1-x)PbI_2 \cdot xNaI$ can be used as a good iodine conductor with the transference number of iodine ions almost equals to unity. The powders of PbI_2 and NaI were mixed with the molar ratio of 0.97:0.03, and then heated to 550 °C for an hour to form solid solution in Ar atmosphere. The ground powders of solid solution were pressed under 150 MPa to form dense pellet, and the carbon film (~50 nm) was deposited on one surface using an ULVAC sputtering machine (ACS-4000-C1-TSS, ULVAC Inc., Japan), P2VP-I_2 complex was pasted on the other surface, and then pressed the pellet with $MAPbI_3$ crystal as Fig. 4-2 shows to form the cell for measurement with a steady contact between $MAPbI_3$ and $0.97PbI_2 \cdot 0.03NaI$ solid solution.

The bias voltage was applied on $0.97PbI_2 \cdot 0.03NaI$ electrolyte using the Ivium station (CompactStat B10060, Ivium Technologies, Netherlands) from 0.1V to 0.8V. The open circuit voltage between two electrodes of $MAPbI_3$, E_{open}, was recorded by a digital multimeter (199 system DMM scanner, Keithley, USA). Similar to the polarization method as described in Chapter 3, the current through $0.97PbI_2 \cdot 0.03NaI$ electrolyte

would be gradually reduced to a certain value when steady state was attained. The *emf* was recorded after the steady state was attained.

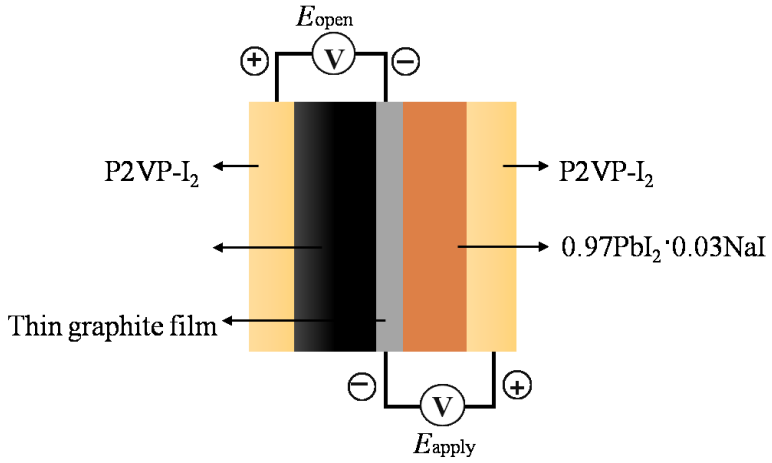

Fig. 4-2 The schematic diagram of cell for equilibrium *emf* measurement. The dc polarization was conducted on 0.97PbI_2·0.03NaI electrolyte, and the *emf* of $MAPbI_3$ was recorded after steady-state was attained.

4.2.4 Total Conductivity Measurement

The total conductivity, σ_{tot}, as the variation of a_{I_2} was measured by a two-probe ac impedance method using $MAPbI_3$ single crystals after annealed in the solution with a series different I_2 activities. As we discussed in Chapter 2, the chemical potential of the components, μ_{PbI_2}, μ_{I_2} and μ_{H_2} should be controlled to fix the A/B ratio and I nonstoichiometry in $MAPbI_3$ materials. Single crystals were placed in a vessel filled with dichloromethane (CH_2Cl_2) solvent with a series different concentration of I_2, and a certain amount of $MAPbI_3$ and PbI_2 powders. According to the discussion of phase relations in Chapter 2, the samples were annealed in equilibrium triangle of $MAPbI_3$-PbI_2-I_2. The vessel was sealed and annealed for four weeks under Ar /H_2 atmosphere to reach the chemical equilibrium state. The solutions with different I_2 concentration were prepared by infinite dilution, and the I_2 activities in different solution for annealing were confirmed by *emf* measurements of an I_2 concentration cell using 0.97PbI_2·0.03NaI solid solution as electrolyte, and PdI_2/Pd as a reference electrode with a fixed a_{I_2}. The *emf* at the steady state was recorded by a digital multimeter (199 system DMM scanner, Keithley, USA) at 25 °C under H_2/Ar atmosphere.

To order to investigate the variation of conductivity of $MAPbI_3$ materials during annealing, two different symmetric cells were prepared in which the structures were expressed as follows,

$$\mathrm{P2VP-I_2}(a_{\mathrm{I_2}}^{\mathrm{H}})\ |\ \mathrm{MAPbI_3(single\ crystal)}\ |\ \mathrm{P2VP-I_2}(a_{\mathrm{I_2}}^{\mathrm{H}}), \quad \text{(A)}$$

$$\mathrm{PbI_2-Pb}(a_{\mathrm{I_2}}^{\mathrm{L}})\ |\ \mathrm{MAPbI_3(polycrystal)}\ |\ \mathrm{Pb-PbI_2}(a_{\mathrm{I_2}}^{\mathrm{L}}), \quad \text{(B)}$$

where $a_{\mathrm{I_2}}^{\mathrm{H}}$ and $a_{\mathrm{I_2}}^{\mathrm{L}}$ represent extremely high and low $a_{\mathrm{I_2}}$ at the interface of $MAPbI_3$/electrode in present work, respectively. When equilibrium state was attained during annealing, the $a_{\mathrm{I_2}}$ in $MAPbI_3$ would be modified to reach the same level as that in electrode, thus, the total conductivity, σ_{tot}, with iodine activities of $a_{\mathrm{I_2}}^{\mathrm{H}}$ and $a_{\mathrm{I_2}}^{\mathrm{L}}$ could be obtained under equilibrium state. The $a_{\mathrm{I_2}}^{\mathrm{L}}$ can be estimated from the following reaction,

$$\mathrm{Pb+I_2=PbI_2}, \quad \text{(4-3)}$$

$$K = a_{\mathrm{PbI_2}}/a_{\mathrm{Pb}}a_{\mathrm{I_2}}. \quad \text{(4-4)}$$

The equilibrium constant of the reactions above could be found from thermodynamic database somewhere, $a_{\mathrm{I_2}}^{\mathrm{L}} = 10^{-30.412}$ at room temperature, and $a_{\mathrm{I_2}}^{\mathrm{H}}$ could be obtained from the *emf* measurements of the I_2 concentration cell described in section 4.2.1.

Cell (A) was annealed at room temperature for 700 h, and cell (B) was annealed at 75°C for 200 h. To compare with $MAPbBr_3$ materials, similar cells with (B) structure using $PbBr_2$-Pb as symmetric electrode, poly crystal and single crystal $MAPbBr_3$ as electrolyte were also prepared and annealed 75°C. Ac impedance spectra of the cells were recorded as a function of annealing time at different temperatures.

All the experiments in this section were conducted in the mixed gas atmosphere of 5% H_2 and 95% Ar to fix the chemical potential of H_2 and restrain the evaporation of CH_3NH_2 during polarization at higher temperatures. The ac impedance spectra were recorded in dark condition using solarton 1255B frequency response analyzer (solarton Inc., England) coupled with solarton 1296 dielectric interface (solarton Inc., England).

4.3 Results

4.3.1 Steady State Current and Partial Conductivity

The steady-state current, i_{ext}, as a function of applied voltage, E_{app}, at 25°C, 30°C, 35°C, 40°C and 45°C were shown in Fig. 4-3. The i_{ext} exhibited a non-linear dependency on E_{app}. A significant increase of i_{ext} was observed at very low applied

voltage range, and then stepped into a platform until E_{app} increased to intermediate voltage about 0.35V. A rapid rise of i_{ext} followed as E_{app} increased to 0.6V, and then gradually increased at high applied voltage range. The variation of $i_{ext} - E_{app}$ curves revealed a similar tendency at different temperatures and shows an exponential increase relationship within the voltage range of measurement.

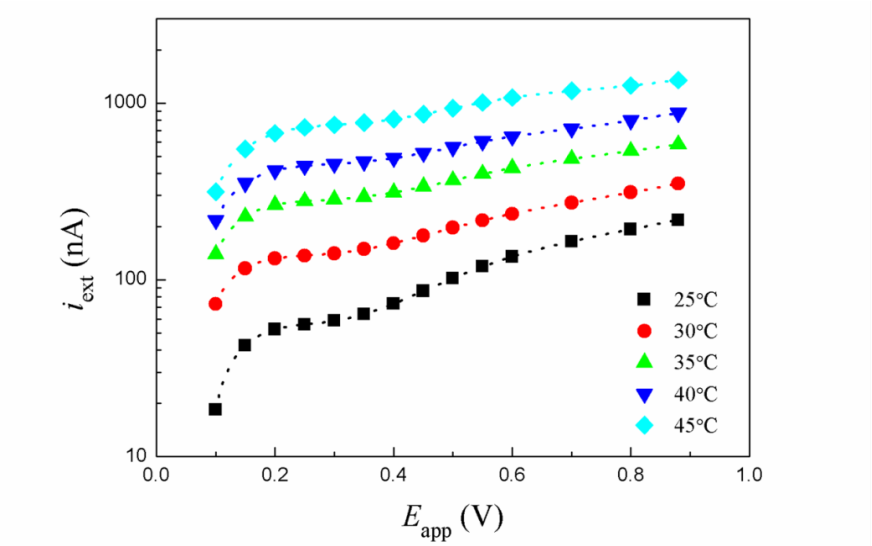

Fig. 4-3 The steady-state current, i_{ext}, as a function of applied voltage, E_{app}, at 25°C, 30°C, 35°C, 40°C and 45°C.

To calculate the differential of $i_{ext} - E_{app}$ curves, the least-squares polynomial fitting was applied in present work,

$$i_{ext} = \sum_{k=0}^{k=5 \text{ or } 7} a_k E_{app}^k. \quad (4\text{-}5)$$

The total electronic conductivity, σ_e^{block}, at the interface of $MAPbI_3$/blocking electrode, $a_{I_2}^{block}$, can be calculated with the following equation [5, 6],

$$\sigma_e^{block} = \frac{L}{A}\frac{di_{ext}}{dE_{app}}, \quad (4\text{-}6)$$

where A and L are electrode area and the thickness of the crystal, respectively. In eq. (4-6), the total electronic conductivity, $\sigma_e^{block} = \sigma_n + \sigma_p$. The values of $a_{I_2}^{block}$ was defined by Nernst's equation, which can be rearranged to,

$$\log a_{I_2}^{block} = \frac{2E_{app}F}{2.303RT} + \log a_{I_2}^{rev}, \quad (4\text{-}7)$$

where F, R and T are Faraday constant, gas constant and temperature, respectively, $a_{I_2}^{rev}$ represents the iodine acitivity at the interface of $MAPbI_3$/reversible electrode, which

was estimated from an I_2 concentration cell using $0.97PbI_2 \cdot 0.03NaI$ as electrolyte, PdI_2/Pd as a reference with a fixed a_{I_2}, and P2VP-I_2 as counter electrode, and the cell structure can be expressed as $\ominus\ PdI_2 - Pd \mid 0.97PbI2 \cdot 0.03NaI \mid P2VP - I_2 \oplus$. The *emf* of the cell was obtained as 0.34 V when equilibrium state was attained at 25°C. The *emf* as a function of temperature was shown in Fig. 4-4. The $a_{I_2}^{rev}$ can be calculated from the equation,

$$\log a_{I_2}^{rev} = \frac{2EF}{2.303RT} + \log a_{I_2}^{-}, \quad (4\text{-}8)$$

where $a_{I_2}^{-}$ represents the iodine activity in PdI_2/Pd electrode, and $\log a_{I_2}^{rev}$ was calculated to be -0.938, -1.005, -1.040, -1.113, and -1.155 at 25°C, 30°C, 35°C, 40°C and 45°C, respectively. The total electronic conductivities, σ_e^{block}, as a function of I_2 activities, $a_{I_2}^{block}$, were calculated using eq. (4-5) ~ (4-8) and plotted in Fig. 4-5 by solid symbols.

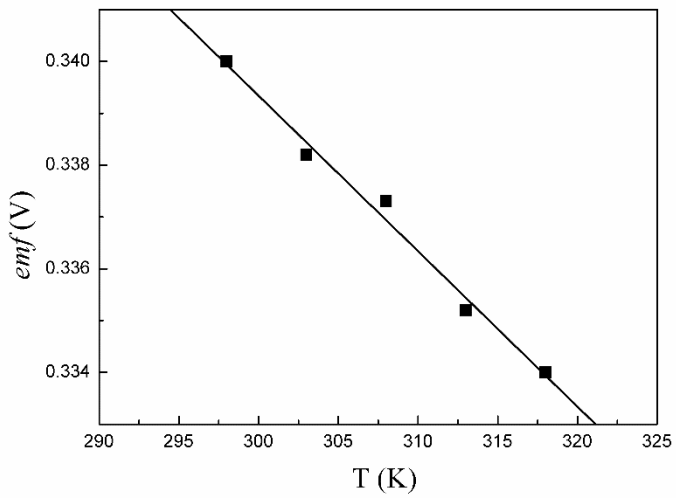

Fig. 4-4 The equilibrium *emf* of the I_2 concentration cell as a function of temperature.

A *p* to *n* transition upon variation of a_{I_2} was observed around 10^{-10}, and the transition point exhibited slight temperature dependency as the temperature increased from 25°C to 45°C. In high a_{I_2} domain, σ_e^{block} showed a 1/4 power dependency on $a_{I_2}^{block}$ just above the *p*/*n* switching point, and σ_p increased followed a linear relationship on $a_{I_2}^{block}$. At higher temperature, σ_p showed a deviation in very high a_{I_2} domain, indicating σ_p gradually become saturated to a certain value of conductivity. In low a_{I_2} region, σ_e^{block} showed a similar power dependency of -1/4, and σ_n rapidly saturated to a constant value at $a_{I_2}^{block} \approx 10^{-17}$. In very low a_{I_2} domain, σ_n exhibited significant deviations hovered

around the saturation value, $\sigma_n^{sat.}$ as a result of the presence of electrons trapping. The boundary of the trapping domain is marked with yellow line in Fig. 4-5. Particularly, compared with $\sigma_n^{sat.}$, the saturated conductivity of holes, $\sigma_p^{sat.}$ exhibits a remarkable increase by one order of magnitude or more if σ_n curve was extrapolated to $a_{I_2}^{block} = 1$. The carrier density of *p* and *n* was asymmetric as the measurement suggested in present work.

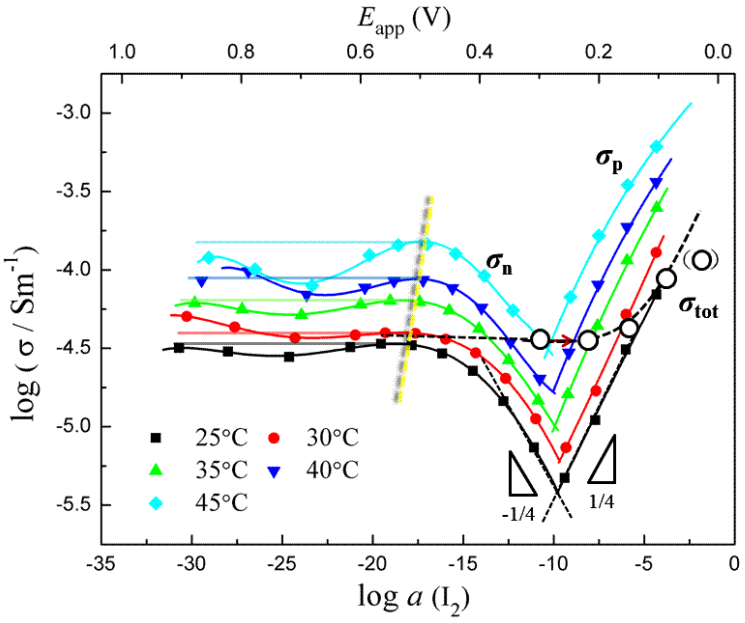

Fig. 4-5 The variation of $\boldsymbol{\sigma_e}$ (solid symbols) calculated from the slope of polarization curves in Fig. 4-4 as a function of $\boldsymbol{a_{I_2}}$, and $\boldsymbol{\sigma_{tot}}$ (open symbols) by ac impedance method measured with the crystals after annealed (yellow line represented the boundary of electron trapping domain, and the semitransparent lines were extrapolated from the fitting lines of partial conductivity curves) .

Compared with $MAPbBr_3$, $MAPbI_3$ shows a significant enhancement of partial electronic conductivities, and almost comparable total conductivities at RT. It is worth noting that the abnormal 1/4 power dependency on $a_{I_2}^{block}$ should due to the deviation from experimental error, in fact, the power dependency might be close to 1/2. Based on the discussion on defect model discussed in Chapter 3, 1/4 power relationship leads to the equal concentration of electrons and defect vacancies in this a_{I_2} region. In generally, the mobility of electrons and holes is much higher than that of defect vacancies, which the electronic conductivity should be dominant, however, the variation of total

conductivity indicated an opposite conclusion that ionic conduction is predominant. Therefore, it is reasonable to assume a 1/2 power dependency in this a_{I_2} region and electrons and holes are just minority carriers.

4.3.2 Ion Transference Number

Different from $MAPbBr_3$ materials, the electronic conduction in $MAPbI_3$ can be expected to be predominant, which makes the current interruption measurement very difficult, since the *IR* drop on voltage is very huge. Therefore, in present work, the ion transference number in $MAPbI_3$ materials was estimated by *emf* measurements based on the double concentration cell as shown in Fig. 4-2. The chemical potential gradient of I_2 between the electrodes of C and P2VP-I_2 was controlled by the bias voltage that applied on $0.97PbI_2 \cdot 0.03NaI$ solid solution. Since the graphite film is thin enough that is sufficient for I^- ion migration, thus, there is no μ_{I_2} gradient across graphite film at the steady-state, and the a_{I_2} at the interface of $MAPbI_3$/C and $0.97PbI_2 \cdot 0.03NaI$/C could be considered as the same value. During dc polarization, the current through $0.97PbI_2 \cdot 0.03NaI$ will gradually decreased until the steady-state was attained, the *emf* was recorded under different E_{app}. According to the discussion in section 3.4.1, the applied voltage, E_{app} and E_{open} across $MAPbI_3$ can be expressed as follows,

$$E_{app} = -\frac{1}{2F}\int_{\mu_{I_2}^{x=0}}^{\mu_{I_2}^{x=L}} d\mu_{I_2}, \tag{4-9}$$

$$E_{open} = -\frac{1}{2F}\int_{\mu_{I_2}^{x=0}}^{\mu_{I_2}^{x=L}} \frac{\sigma_{I^-}}{\sigma_n+\sigma_p+\sigma_{I^-}} d\mu_{I_2} = -\frac{1}{2F}\int_{\mu_{I_2}^{x=0}}^{\mu_{I_2}^{x=L}} t_{ion}\, d\mu_{I_2}. \tag{4-10}$$

Where $\mu_{I_2}^{x=0}$ represent the chemical potential of I_2 at the interface between P2VP-I_2 and $MAPbI_3$ or $0.97PbI_2 \cdot 0.03NaI$ solid solution, and $\mu_{I_2}^{x=L}$ is the chemical potential of I_2 and at the interface of $MAPbI_3$/C/$0.97PbI_2 \cdot 0.03NaI$. Thus, the ions transference number can be calculated with,

$$t_{ion} = \frac{dE_{open}}{dE_{app}}. \tag{4-11}$$

The open circuit voltages as a function of E_{app} at 25°C and 40°C were shown in Fig. 4-6. The least-squares polynomial fitting was applied as follows,

$$E_{open} = \sum_{k=0}^{k=5} a_k E_{app}^k. \tag{4-12}$$

The ion transference number was calculated by the differential of eq. (4-12) as shown in Fig. 4-7. As a_{I_2} decrease, the ions transference number, t_{ion}, gradually increase to 0.8 at

25°C, and 0.85 at 40°C corresponding to an ionic dominant domain. Meanwhile, t_{ion} showes a positive dependency on temperature. The dashed line in Fig. 4-7 represents t_{ion} =0.5, and from the intersections with t_{ion} curves, the transition from ionic conductivity domain to electronic conductivity domain could be obtained as, $a_{\mathrm{I_2}}$=$10^{-8.3}$ and $10^{-6.6}$ at 25°C and 40°C, respectively. The *emf* at this transition was defined as $E_{\oplus}$ (pure I_2 was used as reference). However, no *n*-type domain could be observed in low $a_{\mathrm{I_2}}$ range under present experimental conditions because of strong electron trapping.

This work reveals the presence of *p*-type dominant in higher $a_{\mathrm{I_2}}$ range, and then transit to an ionic dominant domain corresponding to a high ion transference number that suggests ion is the majority carriers and is predominant in the range of log$a_{\mathrm{I_2}}$ <-8.2.

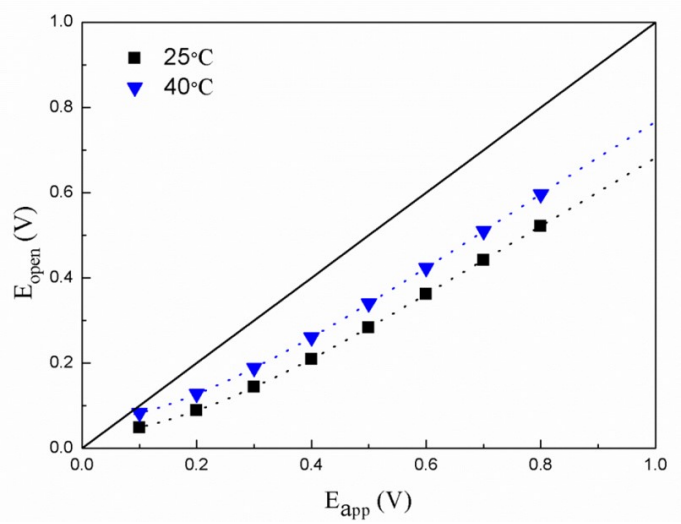

Fig. 4-6 The open circuit voltages as a function of $\boldsymbol{E_{app}}$ at 25°C and 40°C.

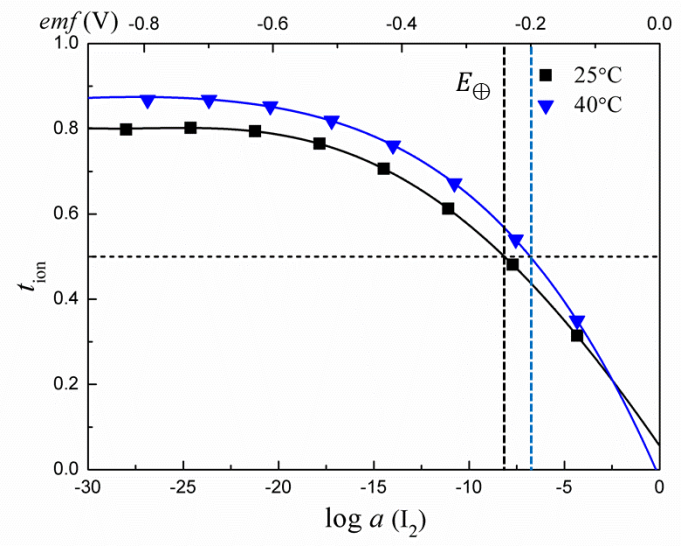

Fig. 4-7 The ion transference number as a function of $\boldsymbol{a_{I_2}}$ at 25°C and 40°C. The dashed line represents $\boldsymbol{t_{ion}}$=0.5 ($\boldsymbol{E_{\oplus}}$ was defined as the equilibrium *emf* of the transition from ionic dominant domain to *p*-type domain, using pure I_2 as reference).

4.3.3 Total Conductivity

The iodine activity of the organic solution used for annealing was obtained from *emf* measurement of an I_2 concentration cell, and cell structure was shown as follows,

$$(-)\text{solution}\left(a_{I_2}\right) \mid 0.97PbI_2 \cdot 0.03NaI \mid \left(a_{I_2}^0\right) \text{P2VP} - I_2(+), \qquad \text{(D)}$$

The *emf* between two C plates of the concentration cell obeys Nernst equation,

$$emf = -\frac{RT}{2F}\ln\frac{a_{I_2}}{a_{I_2}^0}, \qquad (4\text{-}12)$$

where *R*, *T*, *F* are gas constant, temperature, and Faraday constant, a_{I_2} and $a_{I_2}^0$ represent the iodine activity at the interface of solution/electrolyte and electrolyte/P2VP-I_2, respectively. The a_{I_2} in CH_2Cl_2 solvent can be estimated from the *emf* of the concentration cell, and the results were shown in Fig. 4-8.

In infinitely diluted solution, the *emf* can be expressed based on Henry's law as follows,

$$emf = -\frac{2.303RT}{2F}(\log x + \log\gamma_{I_2}^0), \qquad (4\text{-}13)$$

where *x* represents the concentration of I_2 in organic solution, $\gamma_{I_2}^0$ is activity coefficient of ideal solution. The *emf* exhibited almost linear dependency on molar fraction of I_2 in organic solvent, x_{I_2}, and the slope of the line is basically in agreement with theoretical value of $-\frac{2.303RT}{2F}$.

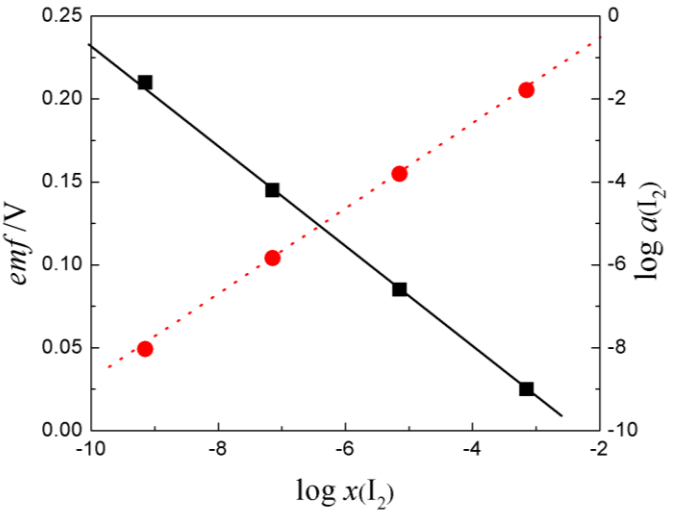

Fig. 4-8 The *emf* of I_2 concentration cell, and activities of I_2 in different organic solutions for annealing.

After annealed for four weeks, the total conductivities, σ_{tot} were measured by ac impedance method, and the total conductivities at room temperature have been plotted in Fig. 4-5 with open symbols. An abrupt decrease of total conductivity was observed when a_{I_2} decreased from high activity domain to intermediate region which should due to the significant enhancement of partial electronic conductivity under oxidizing conditions, indicating a transition from *p*-type to ionic dominant domain. In *p*-type domain, σ_{tot} slowly became saturated with the increasing of a_{I_2}, while, in ionic dominant region, σ_{tot} is almost constant. The ionic conductivities, σ_{ion}, within the measurement region could be calculated from the equation, $\sigma_{ion} = \sigma_{tot} - \sigma_e$, with the variation of a_{I_2}, and the σ_{ion} and σ_e were plotted in Fig. 4-9. The transition point from ions dominant domain to *p*-type domain as shown in the figure is around $\log a_{I_2} \approx -7$, which is basically consistent with the ion transference number in higher a_{I_2} range as discussed in section 4.3.2. At lower a_{I_2} domain ($a_{I_2} \leq 10^{-12}$), the t_{ion} could be estimated of above 0.85 using the extrapulation of σ_{ion} and σ_e lines in Fig. 4-9, consistent the t_{ion} obtained from *emf* measurement.

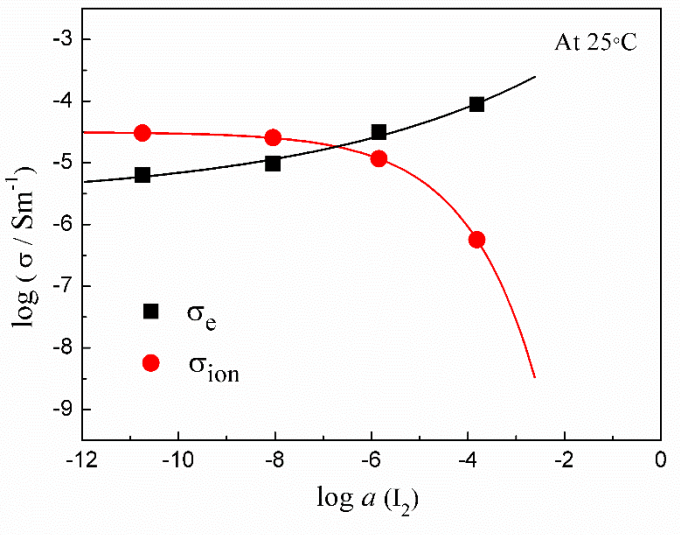

Fig. 4-9 The partial electronic and ionic conductivities as a function of a_{I_2} at 25 ºC.

4.3.4 Conductivities Variation during Annealing

To investigate the variation of the total conductivity of pervoskite materials with the iodine activity, a_{I_2}, we introduced two kinds of symmetric cells, which consisted of two symmetric electrodes with a fixed a_{I_2} and a perovskite bulk in between. Since the a_{I_2} in electrodes and perovskite materials is obviously different, an chemical potential gradient of I_2 was formed between the electrodes and the perovskite materials, which provided a driving force of ions migration between materials with different a_{I_2} if they were in good contact. A schematic diagram of the procedure was shown in Fig. 4-10 when the mixture of lead and lead halide was used as electrode, which provided a reducing condition with an extremely low a_{I_2}. If a_{I_2} in electrodes is much lower than pervoskite materials, perovskite samples will be in a strong reducing environment as shown in Fig. 4-10. As the time extending, the iodine ions will slowly diffuse out of the perovskite layer, and continuously decrease the chemical potential of I_2 in perovskite until a equilibrium state with electrodes was attained. With this method we can obtain total conductivity of perovskite samples with a fixed a_{I_2} finally, and also observe the variation tendency of conductivities during annealing. The two different kinds of symmetric electrode with different a_{I_2} were used in repsent experimental as follows, 1) P2VP-I_2 ($a_{I_2} = 10^{-0.938}$ at RT), 2) PbI_2-Pb ($a_{I_2} = 10^{-25.996}$ at 75 ºC) under strong oxidizing and reducing conditions, respectively, and the total conductivities were shown in Fig. 4-11 and 4-12.

In ac impedance sepctra of the cell with P2PV-I_2 as electrode as shown in Fig. 4-11 (a), two obvious semicircals could be observed due to the contribution of perovskite single crystal and the interface of $MAPbI_3$/P2VP-I_2 respectively. A simple equivalent circuit that describes the physical processes taking place in cell is represented in Fig. 4-12 (b). In this model, R_{bulk} is the resistance of $MAPbI_3$ single crystal, $R_{interface}$ represents the resistance contributed by the resistance of $MAPbI_3$/P2VP-I_2 interface, paralleled with the constant phase element QPE_1, and the resistance of P2VP-I_2, $R_{electrode}$ also paralleled with the constant phase element QPE_2, and the QPE_3 is dominated by geometric capacitance and in some examples may contain components of interface layers responding in a higher frequency region. The conductivities of single crystal were calculated by fitting the spectra with equivalent circuit model above. Fig. 4-11 (b) shows the variation of total conductivities of $MAPbI_3$ single crystal at room temperature

with annealing time extending corresponding to an increasing a_{I_2}. The total conductivity revealed a significant increasing tendency with the annealing time of 20~300 h, and then followed by a slowly grow until the equilibrium state between $MAPbI_3$ and P2VP-I_2 was attained after annealed for 700 h. The total conductivity of single crystal $MAPbI_3$ at, $a_{I_2} \approx 10^{-0.938}$, was estimated to be $10^{-3.662}$ Sm^{-1}. This value is basically consistent with the variation trend of σ_p in *p*-type domain (Fig. 4-5), since holes are domiant carriers and $\sigma_{tot} \approx \sigma_p$ in this domain. The results confirmed the as-grown $MAPbI_3$ single crystals were in *p*-type domain with a possible iodine activity around 10^{-6}.

To compare the variation of total conductivities of $MAPbI_3$ and $MAPbBr_3$ materials, the mixtures of PbI_2-Pb and $PbBr_2$-Pb were used as electrode with a fixed halide activity. The annealing was conducted at 75°C in Ar atmosphere. Since the halide activity in PbX_2-Pb electrode is very low, the halide ions, X^{-1}, will be released from perovskite materials and gradually diffused into electrode, and then form PbX_2 at the interface because of the reaction, $Pb + 2X^- = PbX_2 + 2e'$ as shown in Fig. 4-10. Since the concentration of lead grains is high enough at the interface, this reaction will not change halide activity and conduction at the interface.

A transition in total conductivities of poly crystalline $MAPbI_3$ was observed after annealed for 80 h on the curve marked with red dashed line. The total conductivities decreased gradually at the initial stage before the transition point was achieved during annealing, and then started to increase. The region before transition occurred corresponded to an ions dominant domain with high concentration of electron trap because of the presence of V_I' which is compensated by $V_I^{\cdot}$. The decreasing conductivity in this domain should due to the reduction of ionic conductivity with the increasing of a_{I_2}, and then stepped into a *p*-type domain since the total conductivity started to increase. Because of the huge chemical potential gradient between $MAPbI_3$ and P2VP-I_2, a long time may need to reach the equilibrium state above the annealing time in present experiment. Although $MAPbI_3$ materials exhibit cubic symmetry at 75°C, according to the discussion in Chapter 2, the phase transition might not significantly change the defect chemistry model of perovskite materials, thus, it is possible to explain the behavior at higher temperatures with current data of partial and total conductivities of $MAPbI_3$ materials.

Compared to $MAPbI_3$ materials, the total conductivities of poly crystal $MAPbBr_3$ bulk exhibited just a slight decrease at the initial stage of annealing, and then remain almost constant as the annealing time extending to 150 h. A similar variation tendency of decrease of conductivity was observed in single crystal materials. The variation of σ_{tot} of $MAPbBr_3$ materials is essentially consistent with the results obtained from the crystals annealed in solution, which confirms the ionic conductivity is dominant in a broad range of Br_2 domain.

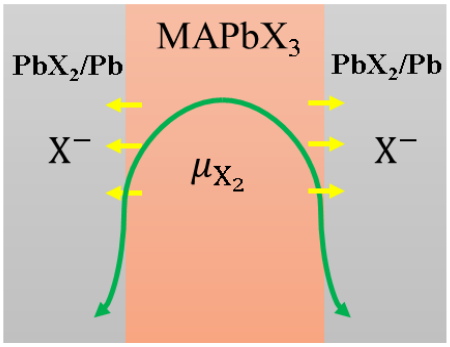

Fig. 4-10 The schematic diagram shows the variation of chemical potential of halogen when lead/lead halide electrode contact with $MAPbX_3$ materials during annealing.

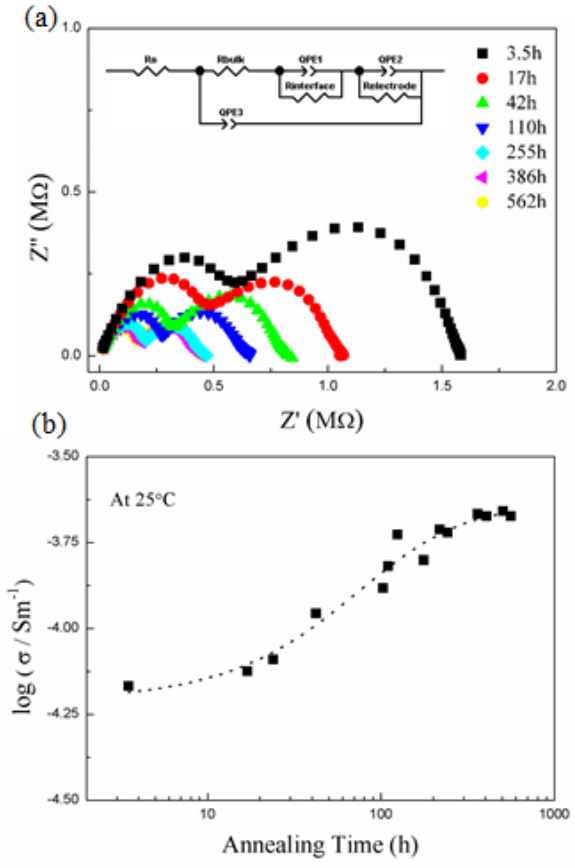

Fig. 4-11 The ac impedance spectra of $\mathbf{P2VP-I_2 \mid MAPbI_3 \mid P2VP-I_2}$ cell (a) and the bulk conductivities as a function of annealing time (b).

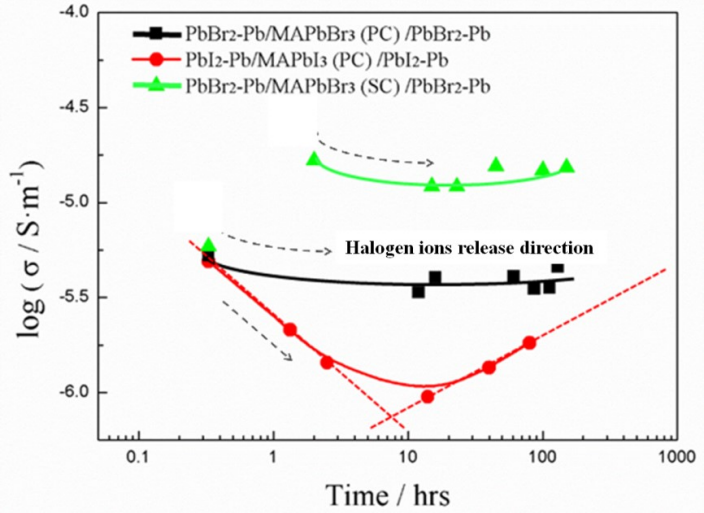

Fig. 4-12 Total conductivities as a function of annealing time at 75°C (PC represents poly-crystal, and SC represents single-crystal).

4.4 Discussion

4.4.1 Defect Chemistry Model

Similar to $MAPbBr_3$ materials, the overall charge neutral condition in $MAPbI_3$ materials can be expressed as follows using Kröger-Vink notation,

$$n + [V'_{MA}] + 2[V''_{Pb}] = [V_I^{\cdot}] + p, \quad (4\text{-}14)$$

where $[V'_{MA}]$ and $[V''_{Pb}]$ are the concentration of V'_{MA} and V''_{Pb}, respectively. As a quaternary system, the defect chemisty of $MAPbI_3$ perovskite depends on A/B ratio and I nonstoichiometry goerned by the chemical potenttial of components, μ_{PbI_2}, μ_{I_2} and μ_{H_2}. A/B nonstoichiometry is related to the synthesis process and can be considered as a certain value in the same batch of single crystals. Meanwhile, further formation of A-site vacancy was inhibited by controlling the chemical potential of H_2 because of the reaction, $2CH_3NH_2 \cdot HI = 2CH_3NH_2 + H_2 + I_2$, thus, the A/B ratio will not be changed in experiment. Since the concentration of V'_{MA} is reported as being much higher compared with V''_{Pb}, and the mobility of A- and B- site vacancy are estimated to be much smaller than halide vacancy [7, 8], the V'_{MA} and V''_{Pb} are reasonably considered as

"frozen" vacancy, which is independent of I_2 activity. This fixed concentration is defined as $\beta_0 = [V'_{MA}] + 2[V''_{Pb}]$, and the neutrality condition can be rewritten as follows,

$$n + \beta_0 = [V_I^{\cdot}] + p. \quad (4\text{-}15)$$

A defect chemical model based on partial Schottky disorder was used to explain the variation of conductivities which can be summarized as follows: For intrinsic ionization of elelctrons and holes,

$$nil \rightarrow e' + h^{\cdot}, \quad (4\text{-}16)$$

The equilibrium constant is,

$$K_i = np, \quad (4\text{-}17)$$

The equilibrium constant for the formation of bromine vacancy

$$I_I^{\times} \rightarrow V_I^{\cdot} + \tfrac{1}{2}I_2 + e', \quad (4\text{-}18)$$

can be expressed as,

$$K_{V_I} = [V_I^{\cdot}] n a_{I_2}^{1/2}. \quad (4\text{-}19)$$

Where $[V_I^{\cdot}]$ are the concentration of $V_I^{\cdot}$, and n and p are the concentration of the free electrons (e') and holes ($h^{\cdot}$), respectively. The simulation of defects concentration based on the model discussed above was shown in Fig. 4-13 (a). The variation of defects concentration is well agreement with the partial conductivities measured by dc polarization in p-type domain and Schottky dominant domain, however, since there is no *n*-type domain could be observed, σ_n should not follow -1/4 power dependency on a_{I_2} but saturated to a constant value in low a_{I_2} region.

Simialr to the conditions of $MAPbBr_3$ materials, the saturated electronic conductivity at low a_{I_2} domain indicated the existence of electron trap where electrons are highly localized around $V_I^{\cdot}$, and form the defect V_I', which compensates $V_I^{\cdot}$ at the low a_{I_2} domain in the $MAPbI_3$ materials. The dependences of defect concentrations, estimated by employing the concentration of V_I' and $V_I^{\cdot}$, can be deduced by the following equations.

$$V_I' \rightarrow V_I^{\cdot} + 2e', \quad (4\text{-}20)$$

$$K'_{V_I} = [V_I^{\cdot}] n^2 / [V_I'], \quad (4\text{-}21)$$

where K'_{V_I} is the equilibrium constant of reaction (4-20). The overall charge neutrality condition can be rewritten as,

$$[V_I'] + n + \beta_0 = [V_I^{\cdot}] + p. \quad (4\text{-}22)$$

The simulation result was shown in Fig. 4-13. (b). In *p*-type domain, $h^{\cdot}$ is compensated

by cationic vacancies, $[V'_{MA}] + 2[V''_{Pb}]$, leading to p being saturated at a constant value of β_0. In Schottky defect dominant domain, $V_I^{\cdot}$ is the predomiant defect, which is conpensated by total concentration of frozen vacancies expressed as $[V_I^{\cdot}] = [V'_{MA}] + 2[V''_{Pb}]$, thus, n and p exhibit -1/2 and 1/2 power dependency on a_{I_2}, respectively. At low a_{I_2}region, V_I' becomes predominant defect compensated by $V_I^{\cdot}$, and the concentration of V_I' and $V_I^{\cdot}$ exhibit 1/2 power dependency on a_{I_2} in low a_{I_2} domain, thus, no increase of free electrons concentration could be observed. Present work suggested the formation of high concentration of electrons trapping when a_{I_2}decreased below 10^{-20} corresponding to an ionic defect dominant domain. The free electron density under saturation depends on the equilibrium constant K'_{V_I} , which could be estimated to be around 10^{10} based on current defect model. Meanwhile, the equilibrium constant parameters was assumed as, $K_{V_I} = 10^{-19}$, $K_i = 10^{-16}$, and the concentration of the "frozen" defects was assumed as, $\beta_0 = 10^{-5}$.

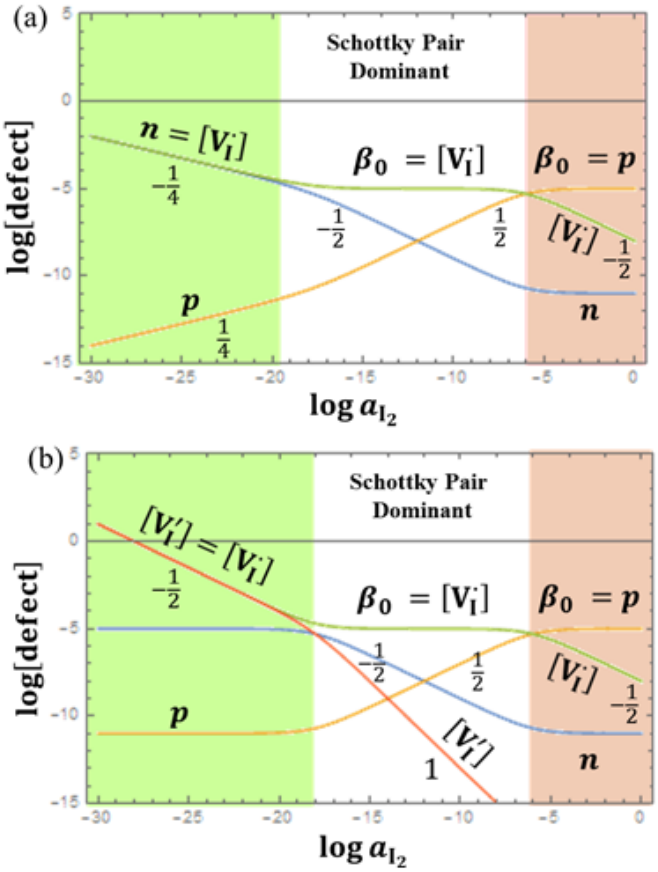

Fig. 4-13 Brower diagram for the $MAPbI_3$ system with (a) charge neutrality condition with $\mathbf{n} + \boldsymbol{\beta_0} = [\mathbf{V_I^{\cdot}}] + \mathbf{p}$, where n-type domain appears at low $\boldsymbol{a_{I_2}}$ region, (b) charge

neutrality condition with $[\mathbf{V_I'}] + \mathbf{n} + \boldsymbol{\beta_0} = [\mathbf{V_I^{\cdot}}] + \mathbf{p}$, where ionic defect is dominant at low $\boldsymbol{a_{I_2}}$ region.

More simulation results by changing equilibrium constant K'_{V_I}could be found in Fig. 4-14. From (a) to (d), $K'_{V_I}$was set as 10^8, 10^9, 10^{12}, 10^{16}, respectively. If K'_{V_I} increase, the saturated concentration of free electrons will gradually decrease, and eventually reduce to the same level with the concentration of holes in low a_{I_2}domain. From the partial and total conductivities of $MAPbI_3$ materials, the saturated concentration of free electrons is lower than holes concentration in p-type domain, estimated as $\sigma_p^{sat.} \approx 3.5\sigma_n^{sat.}$. The K'_{V_I} could be estimated to be 10^9~10^{10} if the mobility of electrons and holes is almost comparable in $MAPbI_3$ materials.

Above all, the defect chemistry model introduced can well describe the results of the polarization experiment, and confirm an ionic dominant domain at lower a_{I_2} domain which is simialr to $MAPbBr_3$ materials, however, $MAPbI_3$ exhibited a wider p-type domain in high a_{I_2} domain as well as a more sigfinicant electron trapping in low a_{I_2} domain .

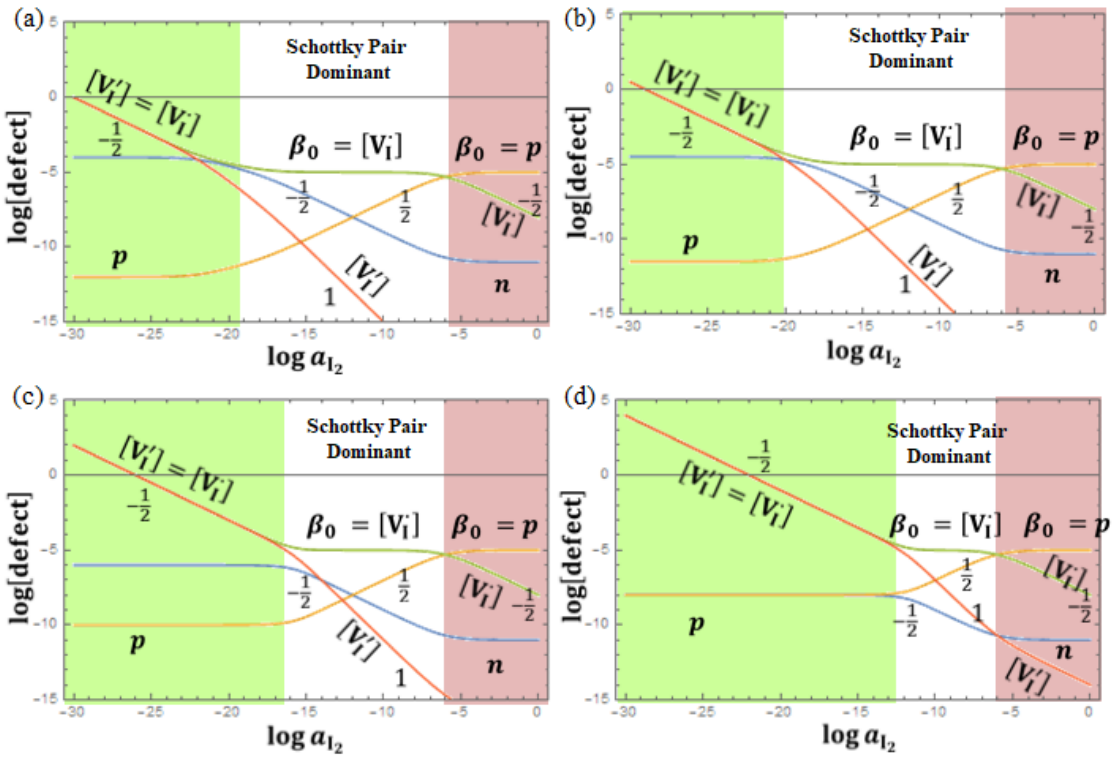

Fig. 4-14 Brower diagram for the $MAPbI_3$ system with charge neutrality condition with $[\mathbf{V_I'}] + \mathbf{n} + \boldsymbol{\beta_0} = [\mathbf{V_I^{\cdot}}] + \mathbf{p}$, where equilibrium constant of electron trapping

formation, $\boldsymbol{K}'_{\mathbf{V_I}}$. From (a) to (d), $\boldsymbol{K}'_{\mathbf{V_I}}$ was set as 10^8, 10^9, 10^{12}, 10^{16}, respectively.

4.4.2 Band Gap Estimation

The band gap of $MAPbI_3$ can be estimated from the *p*/*n* transition point on partial electronic conductivity curves as shown in Fig. 4-15. As we have discussed in section 3.4.3, two approximations were used to estimate the band gap, 1) if the free electron gas approximation is assumed, μ_n and μ_p are proportional to $T^{3/2}$, and σ_{et} can be rewritten as,

$$\sigma_{et} = 2e\left(\frac{2\pi k}{h^2}\right)^{\frac{3}{2}}(m_e^* + m_h^*)^{\frac{3}{4}}\exp\left(-\frac{E_g}{2kT}\right)(a_n + \alpha_p), \quad (4\text{-}23)$$

where m_e^* and m_h^* are the effective mass of the electrons and holes at CBM and VBM, respectively. E_g is the band gap, k is the Boltzmann constant, h is the Planck constant, T is temperature, α_n and α_p are the pre-exponential factors for μ_n and μ_p, respectively. 2) If large polaron approximation is assumed, μ is proportional to $T^{-1/2}$ in general, σ_{et} is expressed as,

$$\sigma_{et} = 2e\left(\frac{2\pi k}{h^2}\right)^{\frac{3}{2}}(m_e^* + m_h^*)^{\frac{3}{4}}T\exp\left(-\frac{E_g}{2kT}\right)(\alpha'_n + \alpha'_p), \quad (4\text{-}24)$$

where α'_n and α'_p are the pre-exponential factors of μ_n and μ_p, respectively. The band gap was estimated to be 1.698 eV by free electron gas approximation and 1.645 eV by large polaron approximation which is in agreement with the band gap measured by UV-visible spectroscopy from previous literature [9, 10].

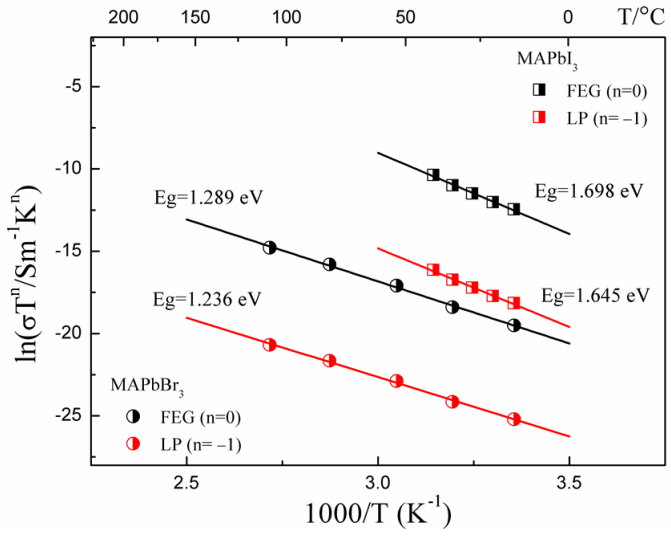

Fig. 4-15 Arrhenius relationship of electronic conductivities of *p*/*n* transition point

($\boldsymbol{\sigma_p = \sigma_n}$) from the polarization curves in Fig. 4-3. The band gap was estimated based on free electron gas approximation (FEG, n=0) and large polaron case (LP, n=-1). The band gap of $MAPbBr_3$ was also plotted for comparison.

4.4.3 Electrochemical Window

The electrochemical stability window and the conductivity domain of $MAPbI_3$ perovskite materials under different temperatures were estimated from polarization results as shown in Fig. 4-16. If pure I_2 was used as a reference electrode, the *emf* of the I_2 concentration cell will be determined by the chemical potential gradient of I_2 through $MAPbI_3$ materials. Based on the discussion in Chapter 3, under PbI_2-rich condition, the *emf* can be estimated to be 0.90 V, while under MAI-rich condition, the emf was expected to be wider determined by Gibbs formation energy, $\Delta_r G^\theta$, of the reaction as follow,

$$MAPbI_3 \rightarrow MAI + PbI_2, \tag{4-25}$$

$\Delta_r G^\theta$ of eq. (4-25) was reported to be about 10.20 KJ corresponding to 0.053v increase of the *emf*. The electrochemical window was shown in Fig. 4-16 with dashed line. The electrochemical window is about 0.9 V~0.95 V, far below the band gap of $MAPbI_3$ (1.7eV). Higher voltage applied on the $MAPbI_3$ materials will lead to decomposition because of over potential.

The conductivity domains of $MAPbI_3$ materials were also shown in Fig. 4-16 with the red lines. The transition a_{I_2} from ionic dominant to *p*-type domain was estimated from the ion transference number, t_{ion}=0.5 (Fig. 4-7), and the corresponding *emf* is defined as $E_\oplus$ (with red dots). The gap of $E_\oplus$ between low temperature and high temperauture range might be related to the transition from tetragonal system to cubic phase. The *emf* corresponding to *n*/*p* switching is defined as $E_{n/p}$ (with blue dots) which was obtained from the partial conductivity curves (Fig. 4-4).

Compared with $MAPbBr_3$ materials, $MAPbI_3$ exhibited a wider *p*-type domain and a narrower electrochemical window indicating poor electrochemical stability of $MAPbI_3$ materials. In both materials, no *n*-type domain could be observed in present experiment because of electron trapping, thus $E_\ominus$ could not be estimated under present experimental conditions.

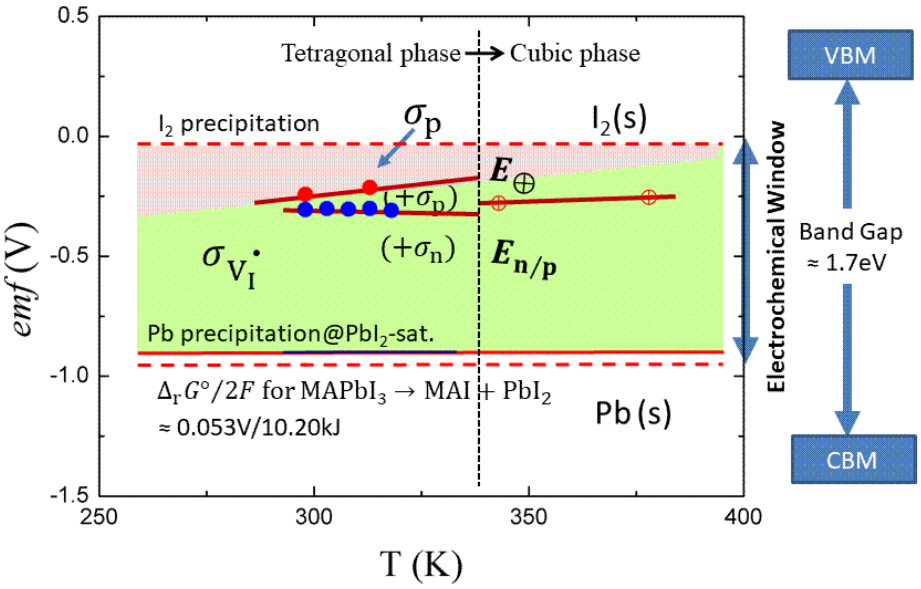

Fig. 4-16 The electrochemical window and the stability domain of $MAPbI_3$ system (solid symbols represent the data in present work, and the open symbols are from previous literature [11]).

4.4.4 Comparison of $MAPbI_3$ and $MAPbBr_3$ Materials

The partial electronic and ionic conductivities of $MAPbI_3$ and $MAPbBr_3$ materials have been measured using electrochemical method as well as transference number of ions. Fig. 4-17 shows the comparison of partial and total conductivities of both materials at 25 ºC and 40 ºC. In a wide range of activity domain, the electronic conductivity of $MAPbI_3$ is much higher than that of $MAPbBr_3$ materials, i.e. in *p*-type domain, $\sigma_p(MAPbI_3) \approx 10\sigma_p(MAPbBr_3)$, and in electron trapping region, $\sigma_n(MAPbI_3) \approx 30\sigma_n(MAPbBr_3)$, however, the total conductivity of these materials is basically comparable, at least in *p*-type domain (marked with blue symbols).

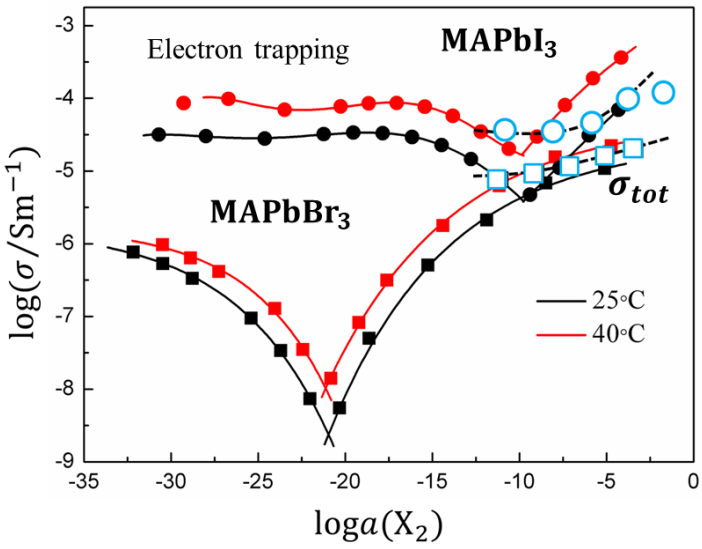

Fig. 4-17 The comparison of partial and total conductivities of $MAPbI_3$ and $MAPbBr_3$ materials at 25 ºC and 40 ºC.

The carrier density of electrons and holes can be estimated as follows,

$$\sigma = neu, \tag{4-26}$$

where σ, n, e, u is the partial conductivity, density, charge number, and mobility of charge carriers. The mobility of electrons and holes has been widely reported by pervious literature [12-14], however, the values dispersed in a board range based on different measurement methods. Table 4-1 shows a range of dispersion on mobilities measured by Hall-effect method (large value) and time-of-flight method (small value), respectively. Combined with the hole conductivity at p-type domain and saturated electron conductivity in low activity range at RT (Fig. 4-17), the carrier density of electrons and holes could be estimated and the results were shown in Table 4-2. It is worth noting that in $MAPbI_3$ materials, the carrier densities of electrons and holes are all in the range of 10^{10}~10^{13} cm^3 which is in well consistent with the value reported by Chen *et al.* [15]. Compared with $MAPbI_3$ materials, the carrier densities of holes in $MAPbBr_3$ is relatively lower, and also consistent with previous report [14].

Table 4- 1 The mobility of electrons and holes reported by pervious literature.

Material	μ_p (cm^2/Vs)	μ_n (cm^2/Vs)	Ref.
$MAPbI_3$	0.063	0.11	[1]
	105±35(SC)	24.8±4.1	[2]
$MAPbBr_3$	115(SC)	--	[3]
	20~60(SC)	--	[3]

*SC represents single crystal

Table 4- 2 The calculated carrier density of electrons and holes in present work.

Material	p (cm^3)	n (cm^3)	Ref.
$MAPbI_3$	9.92×10^{13}	1.80×10^{13}	8×10^{13} (cm^3) [4]
	5.95×10^{10}	7.89×10^{10}	--
$MAPbBr_3$	4.0×10^{12}	--	--
	4.9×10^{10}	--	$5\times10^{9\sim10}$ (cm^3) [3]

From the Arrhenius plots of partial conductivity curves under different temperature, the apparent activation energy of electrons and holes in $MAPbI_3$ and $MAPbBr_3$ materials can be estimated as s function of halogen activity as shown in Fig. 4-18. In both cases, as a_{X_2} decreased, the activation energy exhibited a tendency of a sharp increase and then decrease. A peak could be observed at the a_{X_2} around 10^{-20} ($MAPbBr_3$) and 10^{-12} ($MAPbI_3$) due to the intrinsic ionization of electron/hole pairs, indicating the presence of a narrow intrinsic region around $\sigma_n = \sigma_p$, although the electrons and holes are just minority carriers in this region. Based on the defect model discussed in Chapter 3 and 4, in p-type domain, $p = [V'_{MA}](+2[V''_{Pb}])$, and the predominant vacancy defect will form acceptor level in gap. The energy level could be simply estimated as 0.7 eV and 0.4 eV (corresponds to the activation energy of holes) above the VBM for $MAPbI_3$

and $MAPbBr_3$ materials. In electron trapping region, a similar estimation of donor level is about 0.65 eV and 0.4 eV below the CBM for $MAPbI_3$. Compare the electron trapping region in these materials (Fig. 4-17), the trapping state might form a shallow level in $MAPbBr_3$, but a deep level could be suspected in $MAPbI_3$ materials.

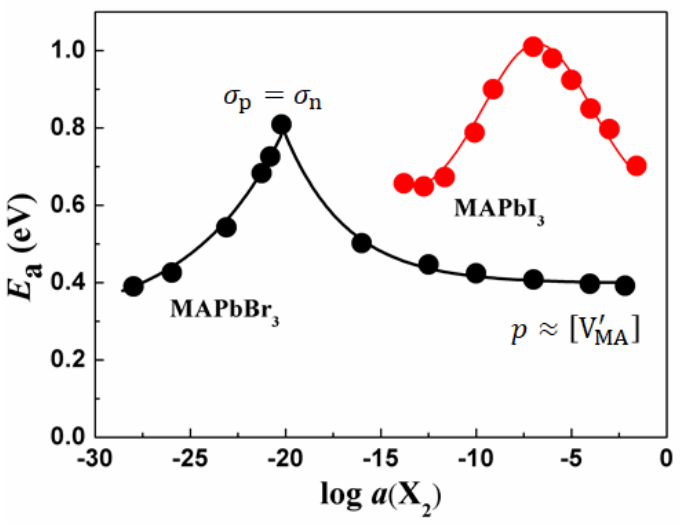

Fig. 4-18 The apparent activation energy of electrons and holes in $MAPbI_3$ and $MAPbBr_3$ materials as a function of halogen activity.

4.5 Summary

The partial electronic conductivities of $MAPbI_3$ perovskite single crystals have been measured by dc polarization method with the variation of a_{I_2} at the temperature of 25°C~45°C under the controllable μ_{PbI_2} and μ_{H_2}, using an asymmetric cell with C film as ion blocking electrode and P2VP-I_2 complex as reversible electrode. The transference number of ions was measured by the equilibrium *emf* of a double concentration cell. An annealing method was also used to control a_{I_2} of single crystals under PbI_2-rich condition, and the total conductivities of these crystals were measured by ac impedance method. The defect model was discussed in this chapter based on the partial Schottky disorder assuming A- and B-site vacancy as "frozen" state adn the presence of electron trapping. Several cells with symmetric electrodes with fixed a_{I_2} were used to estimate the varaition of total conductivities during annealing under different temperatures.

A *p* to *n* transition upon variation of a_{I_2} was observed, and a *p*-type domain was confirmed at high a_{I_2} domain by ion transference number, however, no *n*-type domain

could be detected but an ionic dominant domain in lower a_{I_2} range. The increasing of total conductivity may due to the contribution of partial conductivity of holes in *p*-type domain in agreement with the polarization results. The total conductivity of $MAPbI_3$ with $a_{I_2} = 10^{-0.938}$ was estimated to be $10^{-3.662}$ Sm^{-1} by annealing at 25°C, which is basically consistent with the variation trend of σ_p in *p*-type domain. A transition could be observed on total conductivities curves of cubic $MAPbI_3$ perovskite annealed at 75°C which confirmed the *p*-type domain switch to ionic dominant domain as a_{I_2} decreasing. Discussion about defect chemistry was made employing partial Schottky disorder with frozen vacancies of A-site and B-site and the presence of strong electron trapping by $V_I^{\cdot}$

The band gap of $MAPbI_3$ was estimated to be ~1.7 eV from *p*/*n* switching point, which is consistent with the band gap measured by UV-visible spectra from previous literature.

The electrochemical stability window was estimated to be 0.9 V~0.95 V, far below the band gap of $MAPbI_3$. Compared with $MAPbBr_3$ materials, $MAPbI_3$ exhibited a wider *p*-type domain and a narrower electrochemical window indicating poor electrochemical stability of $MAPbI_3$ materials.

The carrier density of electrons and holes in $MAPbI_3$ and $MAPbBr_3$ materials was estimated to be comparable in the range of 10^{10}~10^{13} cm^3 in agreement with previous studies.

The discussion on band structure based on energy levels of defect vacancies will be helpful for understanding $MAPbI_3$ perovskite materials and evaluating its future applications on photovoltaic devices.

4.6 Reference

[1] Yang TY, Gregori G, Pellet N, *et al*. The significance of ion conduction in a hybrid organic-inorganic lead−iodide−based perovskite photosensitizer. *Angew. Chemie.,* 127(27): 8016-8021 (2015).

[2] Snaith HJ. Perovskites: the emergence of a new era for low-cost, high-efficiency solar cells. *J. Phys. Chem. Lett.,* 4, 3623-3630 (2013).

[3] Schoonman J, Wolfert A, Untereker DF. Hebb-Wagner polarization of PbI_2 with conducting iodine electrodes. *Solid State Ionics*, 11(3): 187-193 (1983).

[4] Sarma NS, Dass NN. Role of vinyl polymers as solid state ionics. *Mater. Sci. Eng. B,* 79(1): 78-82 (2001).

[5] Kobayashi K, Kai Y, *et al*. Electronic conductivity measurements of 5 mol% TiO_2-doped YSZ by a d.c.-polarization technique. *Solid State Ionics,* 93**,** 193–199 (1997).

[6] Kobayashi K, Kai Y, *et al*. Partial Conductivity of YSZ Doped with 10 mol% TiO_2. *J. Korean Ceram*., 4, 114-121 (1998).

[7] Yuan Y, Huang J. Ion migration in organometal trihalide perovskite and its impact on photovoltaic efficiency and stability. *Acc. Chem. Res.,* 49**,** 286–293 (2016).

[8] Azpiroz JM, Bisquert J. Defects migration in methylammonium lead iodide and their role in perovskite solar cells operation. *Energy Environ. Sci.,* 8, 2118-2127 (2015).

[9] Baikie T, Fang Y, Kadro JM, *et al*. Synthesis and crystal chemistry of the hybrid perovskite $(CH_3NH_3)PbI_3$ for solid-state sensitised solar cell applications. *J Mater. Chem. A,* 1(18): 5628-5641 (2013).

[10] Kulkarni SA, Baikie T, Boix PP, *et al*. Band-gap tuning of lead halide perovskites using a sequential deposition process. *J Mater. Chem. A,* 2(24): 9221-9225 (2014).

[11] Senocrate A, Yang TY, Gregori G, *et al*. Charge carrier chemistry in methylammonium lead iodide. *Solid State Ionics,* 321: 69-74 (2018).

[12] Maynard B, Long Q, Schiff EA, *et al*. Electron and hole drift mobility measurements on methylammonium lead iodide perovskite solar cells. *Appl. Phys. Lett.,* 108(17): 173505 (2016).

[13] Dong Q, Fang Y, Shao Y, *et al*. Electron-hole diffusion lengths> 175 μm in solution grown $CH_3NH_3PbI_3$ single crystals. *Science,* aaa5760 (2015).

[14] Shi D, Adinolfi V, Comin R, *et al*. Low trap-state density and long carrier diffusion in organolead trihalide perovskite single crystals. *Science,* 347(6221): 519-522 (2015).

[15] Chen YF, Tsai YT, Bassani DM, *et al*. Evidence of band bending induced by hole trapping at $MAPbI_3$ perovskite/metal interface. *J. Mater. Chem. A*, 4(44): 17529-17536 (2016).

CHAPTER 5

Applications of Perovskite Materials in Novel Photoelectrical Conversion Devices

5.1 Introduction

Based on the measurements of partial and total conductivities of $MAPbX_3$ perovskites varied with halogens activities, the defect chemical properties of hybrid perovskites were investigated and discussed systematically discussed in present work. We found the ionic conductivity is predominant, while electrons are just minority carriers in a wide range of a_{X_2} domain, which is quite different from traditional photoelectrical semiconductor materials. This unique property may broaden the application area of these materials to some degree, and besides absorbers in solar cells, it can probably be used in novel photo-electrical conversion devices because of its good photoelectric properties combined with the significant ionic conduction.

In this chapter, the photo-electrochemical characteristic of $MAPbBr_3$ perovskite single crystals was performed with $Au \mid CH_3NH_3PbBr_3 \mid Pb$ cell. The charge-discharge cycles have been measured under illumination to confirm the influence of ion migration on photo-electrochemical properties, on the basis of electronic band structure modification by photo-polarization. Also applications for novel photo-electrochemical energy conversion device will be discussed.

5.2 Photo-rechargeable Capacitor

The solid-state photo-rechargeable capacitors have been reported that could be obtained by coupling a dye-sensitized solar cell and a semiconductor metal oxide based electrochemical capacitor [1]. Different from the traditional photo-capacitors which comprise of parallel combination of two separate devices, a capacitor and a photo-cell, the system based on $MAPbBr_3$ material could permit direct storage of electrochemical energy generated by sunlight within a single system contributed by its high photoelectric properties and the significant conduction of vacancy defects. The concepts of preparation of photo-rechargeable capacitor is described in Fig. 5-1, the electronic band structure modified under illumination is related to the conductivity contributed by ionic vacancies, $V_{Br}^{\cdot}$, in $MAPbBr_3$ materials. Under illumination, a *p*/*n* junction will

form due to the migration of photo-excited electrons and holes, meanwhile, $V_{Br}^{\cdot}$ will migrate to the direction as shown with arrows. In the condition of $\sigma_e > \sigma_i$, the band structure exhibits almost no change during $V_{Br}^{\cdot}$ migration due to very low concentration of ionic defects. However, in the condition of $\sigma_e < \sigma_i$, some in-gap states, such as shallow donor level and acceptor level, will be formed caused by the significant ions migration, and Fermi level will shift towards CBM and VBM in *n*-type and *p*-type domain respectively, which determines the electrochemical energy that can be directly stored in the device generated by illumination.

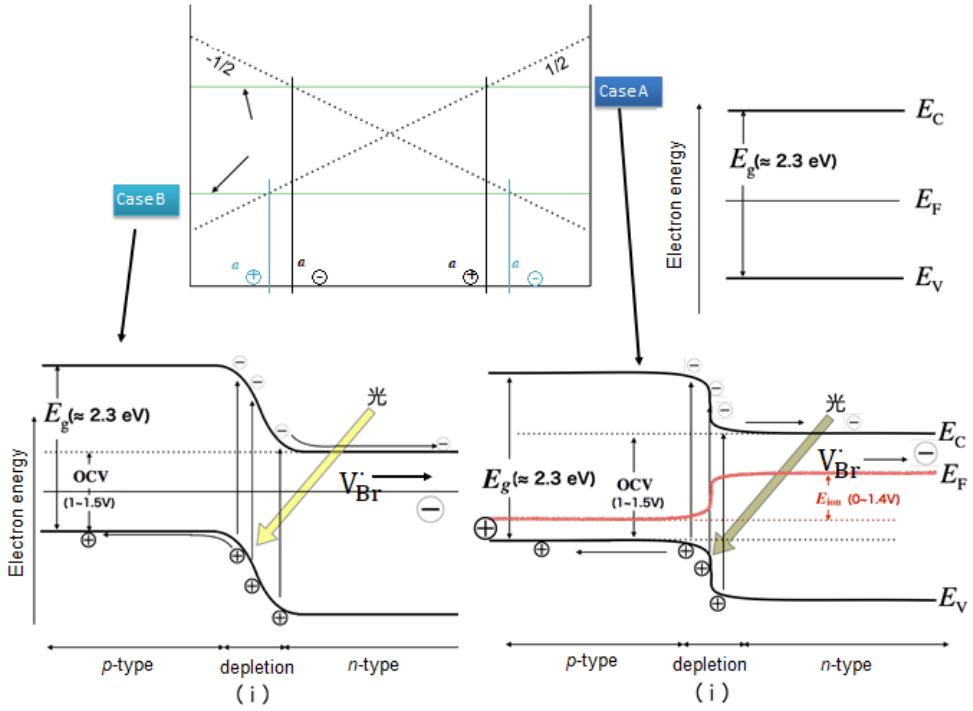

Fig. 5-1 The band structure modification under illumination under different conditions of $\boldsymbol{\sigma_e > \sigma_i}$ and $\boldsymbol{\sigma_e < \sigma_i}$ respectively.

The photo-electrochemical characteristic of $MAPbBr_3$ perovskite single crystals wasuk performed with Au | $MAPbBr_3$ | Pb cell, the cell structure and energy levels diagram of the components involved in the cell were shown in Fig. 5-2. The single crystal for measurements was prepared in $PbBr_2$ saturated condition, and a Hg UV lamp was used as light source in present experiment. The charge-discharge curves have been measured under illumination as shown in Fig. 5-3. Once light was turned on, the open circuit voltage (OCV) gradually increased to 0.42 V, as the illumination time extended, the OCV maintains almost constant, and then gradually decay after light was turned off.

The OCV shows a similar decay behavior in dark condition after illuminated for different times, the relaxation time during decay was estimated to be around 700 s.

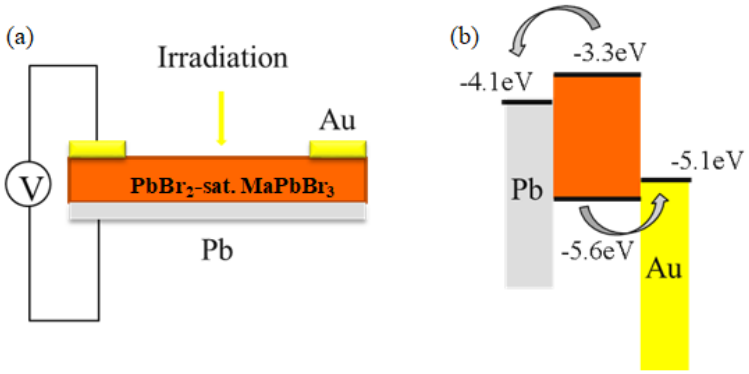

Fig. 5-2 The schematic diagram of Au | $CH_3NH_3PbBr_3$ | Pb cell (a), and energy level diagram of components (b).

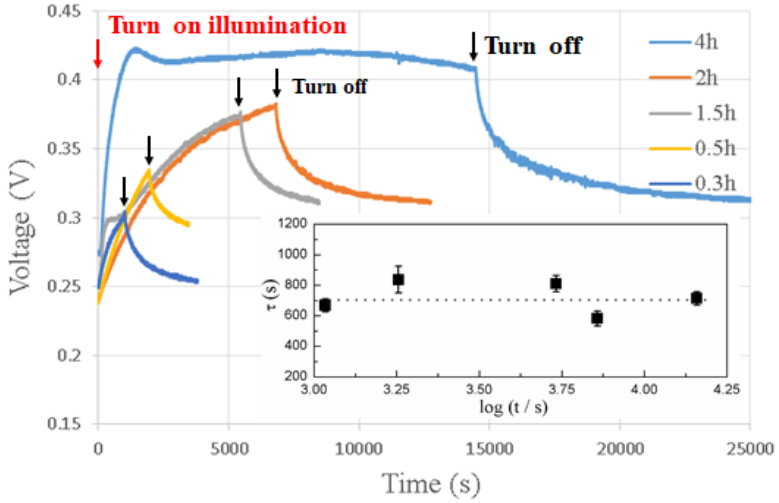

Fig. 5-3 The charge-discharge curves under different illumination time.

The Schematic diagram of the electronic band structure modification by photo-polarization was described in Fig. 5-4. Once the semiconductor contacts with metal electrodes, the energy levels of different components are aligned at their interface due to the band bending in space charge layer. The thermal equilibrium state, in which Fermi level is constant everywhere in the whole system marked with dashed line in figure, is assumed to be achieved. The open circuit voltage in dark condition, E^{D}_{open}, was 0.25 V which caused by the difference of electrochemical potential at the interface of $MAPbBr_3$/electrode. The open circuit voltage under illumination, E^{I}_{open}, was estimated

to be 1.3 V as shown in Fig. 5-4. However, the E^{I}_{open} obtained in present work is far below this theoretical value, it is because the light intensity will be sharply reduced with thickness, thus, photo-excitation occurs only on the surface of the single crystals. Higher E^{I}_{open} could be obtained if high quality of perovskite thin films was used instead of bulk crystals.

Based on electronic band structure modification by photo-polarization, the charge-discharge curves have confirmed the influence of ion migration on photo-electrochemical properties, which provides the feasibility of fabricating photo-rechargeable capacitor based on $MAPbBr_3$ materials with selective electrodes.

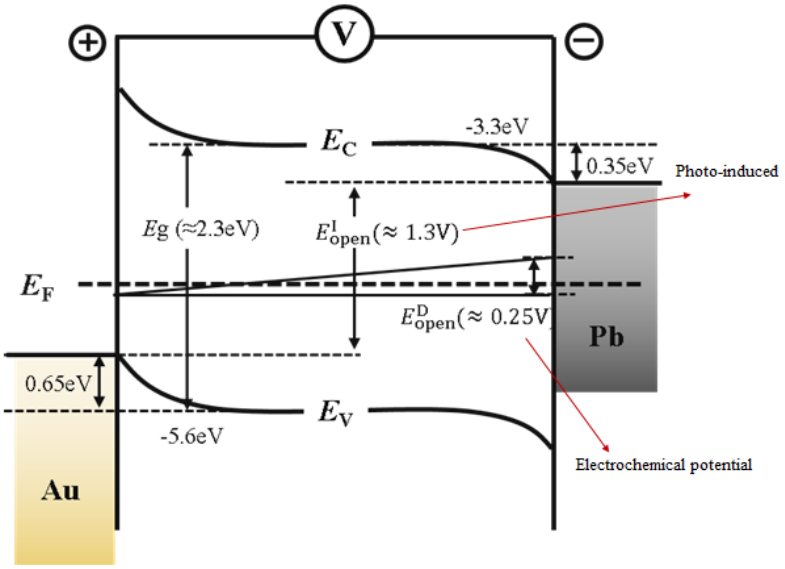

Fig. 5-4 The Schematic diagram of the electronic band structure modification by photo-polarization.

5.3 Photo-intercalation Device

Another possible application of hybrid perovskite materials is to prepare the photo-intercalation devices. The mechanism of intercalation could be explained with the schematic diagram shown in Fig. 5-5 in which X^- represents the halogen ions. The mixture of metal/metal halide was used as layer compounds, which intercalates X^- in a highly reversible manner at room temperature. During discharging of the device, the X^- will be intercalated into M^0_B/M_BX_m electrode driven by the chemical potential gradient of X_2 between two reversible electrodes. Electrons will flow in the external circuit from M^0_B/M_BX_m electrode with a lower a_{X_2} to M^0_A/M_AX_n electrode with a higher a_{X_2}. A

current imposed in the opposite direction, which generated by photo-excitation, will cause the X^- ions deintercalate into $MAPbBr_3$ layer. Unlike earlier reported photo-intercalation device based on intercalation compounds (TM_iX_2) of transition-metal dichalcogenides (TX_2) [2], the intercalation reaction between halogens and metal/metal halide in present work will not yield any new products during charging-discharging cycles.

The open circuit voltage of the photo-intercalation device is determined by the chemical potential gradient of X_2 between reversible electrodes. There are several metal/metal halide system can be used as reversible electrode that could provide different activities of X_2. Take $MAPbBr_3$ for instance, the metal/metal bromine mixture and corresponding OCV were plotted in Fig. 5-6 using pure Br_2 as reference. The mixture of $Pb/PbBr_2$, $Sb/SbBr_3$, $Sn/SnBr_2$, $CuBr/Cu$ may generate OCV above 1.0V taking pure Br_2 electrode as reference, which can more effectively store electrochemical energy converted from solar energy.

The device we designed can effectively convert solar energy into electrochemical energy, and the charging-discharging of the device can be achieved by the intercalation and de-intercalation of the halogen ions between the reversible electrodes. To optimize the light transmittance of the reversible electrodes, extend the illumination area, and improve the conversion efficiency are important issues that need further investigation.

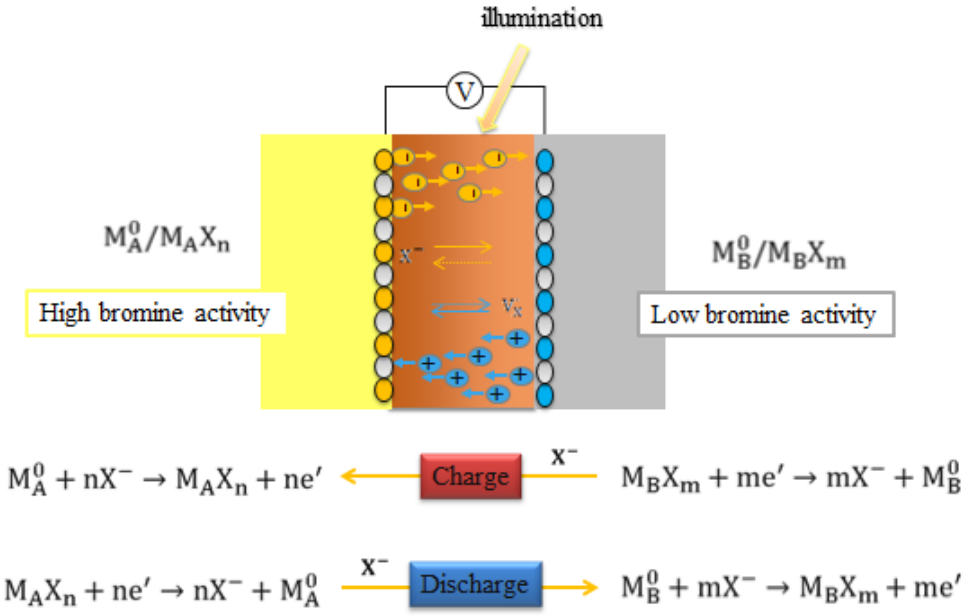

Fig. 5-5 The schematic diagram of photo-intercalation device using metal/metal halide with a certain halogen activity as electrodes.

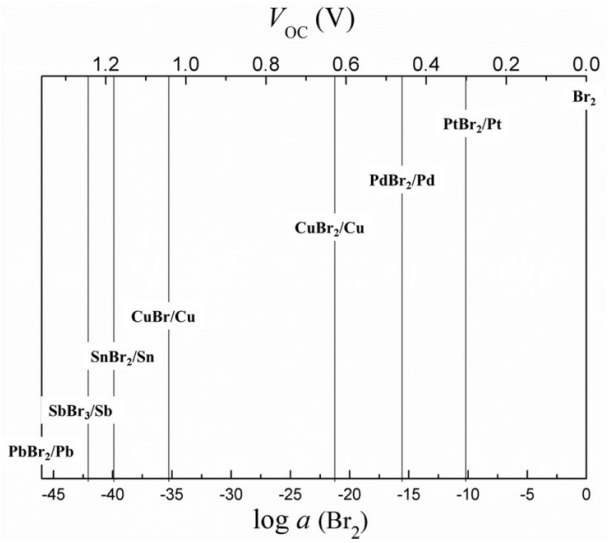

Fig. 5-6 The open circuit voltage of the cell in Fig. 5-5 with different metal/metal halide with a certain halogen activity as electrodes.

5.4 Summary

The photo-electrochemical properties of $MAPbBr_3$ single crystals and the applications for novel photo-electrochemical energy conversion devices based on $MAPbX_3$ perovskite were discussed.

The photo-induced charge curves of Au | $CH_3NH_3PbBr_3$ | Pb cell and also discharge process in dark condition was measured, which confirmed ions migration is of significant importance on photo-electrochemical properties, based on the electronic band structure modification by photo-polarization. According to the discussion in this chapter, $MAPbX_3$ perovskites can probably be used in novel photo-electrical conversion devices, such as photo-rechargeable capacitors and photo-intercalation devices, because of its good photoelectric properties combined with the significant ionic conduction.

In this chapter, we analyzed the working mechanisms of the photo-electrochemical conversion devices, and also introduced some possible choices for devices designing. We expect that the photo-electrochemical conversion efficiency can be improved by optimizing the structure of the devices, and achieve the storage electrochemical energy within a single system based on $MAPbX_3$ perovskites.

5.5 Reference

[1] Skunik-Nuckowska M, Grzejszczyk K, Kulesza PJ, *et al*. Integration of solid-state dye-sensitized solar cell with metal oxide charge storage material into photoelectrochemical capacitor. *J Power Sources,* 234: 91-99 (2013).

[2] Tributsch H. Photo-intercalation: Possible application in solar energy devices. *Appl. phys*., 23(1): 61-71 (1980).

CHAPTER 6

Conclusion

Methylammonium lead halide perovskite materials have recently draw extraordinary attentions as a promising photovoltaic materials benefit from the excellent photo-electrical properties, which exhibits significant ionic charge transport in addition to electronic conduction. Based on the theoretical calculations and electrochemical measurements, it is generally accepted that halide ions should be the most mobile species with a very low activation energy, however, there are still some controversies on the species of dominant ionic defects under different chemical potentials of the components in perovskites, and more importantly, no systemic experimental evidences were reported to support the calculation results.

In Chapter 1, the research background of the $MAPbX_3$ perovskite materials is introduced including the crystals structure, electronic structure, ionic conduction as well as thermodynamic instability of these perovskite materials. Based on these theoretical calculations and electrochemical measurements, it is halogen ion was found to be the most mobile species in perovskites with low activation energy, however, the details of partial conductivities of electrons and holes have never been established. The objectives and innovation of this work were demonstrated in this chapter. Different from previous reports, the electrochemical properties and defect chemistry of $MAPbX_3$ was investigated using Hebb-Wagner dc polarization combined with current interruption technique. The partial electronic conductivity and transference number of ions was estimated as a function of the chemical potential of halogens, which will be helpful for understanding the defect chemical properties of the materials.

In Chapter 2, high quality single crystals of $MAPbBr_3$ and $MAPbI_3$ perovskites were prepared by solution-process technology with clear transparency and well-controlled shapes. XRD patterns of single crystals showed that $MAPbBr_3$ is in cubic phase with {001} orientation, while $MAPbI_3$ showed tetragonal symmetry with {112} orientation at room temperature. The TG/DTA analysis revealed a high thermal stability of single crystals above 240°C in both Ar and Ar/H_2 atmosphere. For $MAPbBr_3$ materials, the presence of H_2 almost had no effect on the decomposition temperature, however, $MAPbI_3$ single crystals exhibited an improvement of thermal stability in Ar/H_2 atmosphere. The phase stability was also confirmed by high temperature XRD, which

exhibited a phase decomposition of samples at 240°C in well agreement with the TG/DTA profiles, and the phase transition of $MAPbI_3$ from tetragonal to cubic symmetry at ~55° was also observed on XRD patterns. The total conductivities of single crystals were measured by ac impedance method varied with temperature. The activation energy of $MAPbBr_3$ and $MAPbI_3$ single crystals was estimated to be 0.13 eV at low temperature and followed by a sharp bending as the temperature increased. A transition from intrinsic to extrinsic region was observed at low temperature (below 100°C) on Arrhenius plot in both $MAPbBr_3$ and $MAPbI_3$ materials, which indicated the material is in a "frozen" state with a fixed defects concentration at lower temperatures, above the transition temperature, the abrupt increase of apparent activation energy should contributed by the enthalpy of defect vacancy formation. The phase relations of perovskites were also discussed in this chapter. $MAPbX_3$ materials should be considered as a quaternary system, three independent variables, μ_{PbX_2}, μ_{X_2} and μ_{H_2} should be fixed to completely describe the state of the system. The thermodynamic stability of $MAPbX_3$ system was also discussed, and under equilibrium state, μ_{HBr} was found much higher than μ_{HI}, thus $MAPbBr_3$ is less sensitive to the vapor pressure of H_2. The analysis in this chapter is helpful for understanding the defect chemistry of $MAPbX_3$ materials, and confirmed the method to control A/B ratio and X nonstoichiometry in following dc polarization.

In Chapter 3, the partial conductivities of electrons and holes of $MAPbBr_3$ perovskite single crystals have been measured by Hebb-Wagner dc polarization with the variation of a_{Br_2} at the temperature of RT~95 °C using an asymmetric cell with an ion blocking electrode and reversible electrode, combined with a current interruption technique of ion transference number measurements under steady-state. An annealing method was used to control a_{Br_2} of single crystals under $PbBr_2$-rich condition, and the total conductivities of these crystals were measured by ac impedance method. The possible defect chemicstry model was also discussed based on the partial Schottky disorder. The electrochemical window was discussed in detail based on the possible stability strategy of $MAPbBr_3$ system. A *p* to *n* transition upon variation of a_{Br_2} was observed, however, it is confirmed that the partial ionic conductivity is dominate in a wide range of stability domain. The increasing of total conductivity was related to the enhancement of partial electronic conductivity in *p*-type domain. Discussion about defect chemistry was made employing simplified partial Schottky model with frozen vacancies of A-site and B-site

and the presence of electron trapping by Br vacancy. The band gap of $MAPbBr_3$ was estimated to be 1.3 eV from *p*/*n* switching point, which is narrow compared with the band gap measured by UV-visible spectra of 2.2 eV, which may due to the existence of possible in-gap defect states. The predominance of ionic carrier means that the system is almost a pure electrochemical system that the stability of the system under bias voltage or photo-generated voltage is governed by the electrochemical window, which was estimated to be 1.36~1.46 V based on the calculation of the thermodynamic properties of $MAPbBr_3$, leading to the stability domains of the system narrower than the intrinsic band gap.

In Chapter 4, the partial electronic conductivities of $MAPbI_3$ perovskite single crystals was measured by dc polarization method at the temperature of 25°C ~45°C under the controllable μ_{PbI_2} and μ_{H_2}, using an asymmetric cell with C film as ion blocking electrode and P2VP-I_2 complex as reversible electrode. The transference number of ions was measured by *emf* under steady-state generated by the μ_{I_2} gradient through $MAPbI_3$ that controlled by E_{app} applied on $0.97PbI_2 \cdot 0.03NaI$ electrolyte. Annealing method was used to control a_{I_2} of single crystals under PbI_2-rich condition. Several cells with symmetric electrodes with fixed a_{I_2} were used to estimate the varaition of total conductivities during annealing. The total conductivities of these single crystals were measured by ac impedance method. A p to n transition upon variation of a_{I_2} was observed, and a *p*-type domain was confirmed at $a_{I_2} > 10^{-8}$ region by ion transference number, however, no *n*-type domain could be detected but an ionic dominant domain was observed in lower a_{I_2} range. The increasing of total conductivity may due to the contribution of partial conductivity of holes in *p*-type domain in well agreement with the variation of ion transference number. The band gap of $MAPbI_3$ was estimated to be ~1.7 eV from *p*/*n* switching point, which is consistent with the band gap measured by UV-visible spectra from previous literature. The electrochemical stability window was estimated to be 0.9 V~0.95 V, far below the band gap of $MAPbI_3$. Compared with $MAPbBr_3$ materials, $MAPbI_3$ exhibited a wider *p*-type domain and a narrower electrochemical window indicating poor electrochemical stability of $MAPbI_3$ materials. The carrier density of electrons and holes in $MAPbI_3$ and $MAPbBr_3$ materials was estimated to be comparable in the range of 10^{10}~10^{13} cm^3 in agreement with previous studies. The discussion on band structure based on energy levels of defect

vacancies will be helpful for understanding $MAPbI_3$ perovskite materials and evaluating its future applications on photovoltaic devices.

In Chapter 5, the photo-electrochemical properties of $MAPbBr_3$ single crystals and the applications for novel photo-electrochemical energy conversion devices based on $MAPbX_3$ perovskite were discussed. The photo-induced charge-discharge curves of Au | $CH_3NH_3PbBr_3$ | Pb cell confirmed ions migration is of significant importance on photo-electrochemical properties, based on the electronic band structure modification by photo-polarization. Therefore, $MAPbX_3$ perovskites can probably be used in novel photo-electrical conversion devices, such as photo-rechargeable capacitors and photo-intercalation devices, because of its good photoelectric properties combined with the significant ionic conduction. In this chapter, the working mechanism of the photo-electrochemical conversion devices was analyzed, and some possible choices for devices designing were introduced.

Present work will be helpful for a full understanding of the charge carrier chemistry and its transport properties in $MAPbX_3$ perovskites, which is an essential prerequisite for further enhancement of the device performance. Based on all the conclusions present work have drawn, $MAPbX_3$ materials behaves more like an electrolyte but not typical semiconductor, at least in dark condition. Meanwhile, the ionic conduction has been proved to be tunable under photo-excitation and can be enhanced by several orders of magnitude, which is absolutely surprising. The electrochemical window of $MAPbX_3$ materials is far below the band gap indicating the materials will be decomposed in a low voltage range, this phonomenen limits the development of photovoltaic materials, and to investigate pervoskites with high stability and better conversion efficiency is in urgent need. Benefit from the excellent ionic transport properties of the hybrid perovskite materials, the generation of a new class of smart devices based on hybrid perovksites may be expected, such as light-induced energy storage, and light-induced switches. Photo-intercalation device is one possible choice, in which solar energy can be effectively converted to electrochemical energy, and the charging-discharging of the device can be achieved by the intercalation and de-intercalation of the halogen ions between the reversible electrodes. By optimizing the structure of such devices, there is high possibility that the photo-electrochemical conversion efficiencies could be improved, and the storage of electrochemical energy within a single system could be achieved in the future.

List of Symbols and Abbreviations

i_{ext}	Current through external circuit
E_{app}	Applied voltage on samples for polaization
E_{open}	Open circuit voltage after current interrupted
$a_{\mathrm{Br_2}}^{\mathrm{rev}}$	Bromine activity at the interface of $MAPbBr_3$/reversible electrode
$a_{\mathrm{I_2}}^{\mathrm{rev}}$	Iodine activity at the interface of $MAPbI_3$/reversible electrode
$a_{\mathrm{Br_2}}^{\mathrm{block}}$	Bromine activity at the interface of $MAPbBr_3$/Au electrode
$a_{\mathrm{I_2}}^{\mathrm{block}}$	Iondine activity at the interface of $MAPbI_3$/C electrode
σ_{tot}	Total conductivity
$\sigma_{\mathrm{e}}^{\mathrm{block}}$	Electronic conductivity at the interface of $MAPbX_3$/blocking electrode
σ_{n} , σ_{p}	Partial conductivity of electrons and holes
μ_{e}, μ_{p}	Mobility of electrons and holes
σ_{ion}	Partial conductivity of ions
$\sigma_{\mathrm{p}}^{\mathrm{sat.}}$, $\sigma_{n}^{\mathrm{sat.}}$	Saturation partial conductivity of holes and electrons
t_{ion}	Transference number of ions
L/A	Cell parameter used for dc polarization
p, *n*	Carrier density of holes and electrons
$\mathrm{V_{Br}^{\cdot}}$, $[\mathrm{V_{Br}^{\cdot}}]$	Bromine vacancy and its defect concentration
$\mathrm{V_{MA}^{'}}$, $\left[\mathrm{V_{MA}^{'}}\right]$	A-site vacancy and its defect concentration
$\mathrm{V_{Pb}^{''}}$, $\left[\mathrm{V_{Pb}^{''}}\right]$	B-site vacancy and its defect concentration
$\mathrm{V_{Br}^{'}}$, $[\mathrm{V_{Br}^{'}}]$	Bromine vacancy with negative charge contributed by electrons trapping, and its defect concentration

$K_{V_{Br}}$	Equilibrium constant of bromine vacancy formation
$K'_{V_{Br}}$	Equilibrium constant of electrons trapping formation
K_i	Equilibrium constant of intrinsic ionization
α_0	Defect concentration of "frozen" Schottky pair in $MAPbBr_3$ materials
μ_{Br_2}	Chemical potential of Bromine
η_{Br^-}	Electrochemical potential of Br^- ion
η_n, η_p	Electrochemical potential of electrons and holes
emf	Electromotive force of concentration cell
$a^{\theta}_{Br_2}$	Br activity of pure liquid Br_2
$\gamma^{0}_{Br_2}$	Activity coefficient of Br_2 in ideal solution
c_{Br_2}	Concentration of Br_2 in diluted solutions for annealing
E_a	Activation energy of ion migration
F	Faraday constant
R	Gas constant
T	Temperature in Kelvin
i_{total}	Total current contributed by ions and electrons
m^*_e, m^*_h	Effective mass of the electrons and holes at conduction band maximum and valence band minimum
E_C, E_V	Conduction band and valence band
E_F	Fermi level
$\alpha_n, \alpha_p,$	Pre-exponential factors for μ_n and μ_p in free gas approximation
α'_n, α'_p	Pre-exponential factors for μ_n and μ_p in large polaron approximation
ΔG^o_f	Standard Gibbs formation energy of the Br_2 concentration cell using $MAPbBr_3$ as electrolyte

$E_{\oplus}$	*Emf* represents transition from ion dominant to holes dominant domain
$E_{\ominus}$	*Emf* represents transition from ion dominant to electrons dominant domain
σ_{j}	Partial conductivity of charge carrier j in materials
Z_{j}	The valence of charge carrier j
η_{j}	Electrochemical potential of charge carrier j
$\mu_{\mathrm{H_2}}$	Chemical potential of H_2
$\gamma^{0}_{\mathrm{I_2}}$	Activity coefficient of I_2 in ideal solution
$c_{\mathrm{I_2}}$	Concentration of I_2 in diluted solutions for annealing
$\mathrm{V_I^{\cdot}}$, $[\mathrm{V_I^{\cdot}}]$	Iodine vacancy and its defect concentration
$\mathrm{V_I^{'}}$, $[\mathrm{V_I^{'}}]$	Iodine vacancy with negative charge contributed by electrons trapping, and its defect concentration
β_0	Defect concentration of "frozen" Schottky pair in $MAPbI_3$ materials
$K_{\mathrm{V_I}}$	Equilibrium constant of iodine vacancy formation
$K^{'}_{\mathrm{V_I}}$	Equilibrium constant of electrons trapping formation
τ	Relaxation time
$E^{\mathrm{D}}_{\mathrm{open}}$	Open circuit voltage in dark condition
$E^{\mathrm{I}}_{\mathrm{open}}$	Open circuit voltage under illumination
R_{ion}	Resistance of ions
R_{eon}	Resistance of electrons

List of Figures

List of Tables

Acknowledgements

I would like to express my deepest gratitude to my supervisor, Prof. Shu Yamaguchi, for his generous intellectual and constant encouragement. I am very grateful for the vast knowledge and insightful guidance he offered, and without his consistent and illuminating instruction, this thesis could not have reached present form. I really learned a lot of from him, such as, self-confidence, logical reasoning ability, enthusiasm for scientific research and strong creativity. It is a great pleasure to work in his group.

I'd like to appreciate sincerely to Dr. Kobayashi and Dr. Miyoshi for the very useful technical support on dc polarization measurements. I would also like to thank Mr. Tanaka for his valuable support and useful advices on technology. I'm also thankful to Dr. Yajima for the discussion about Hall-effect measurements to estimate the carrier concentration and mobility.

I'd like to appreciate all the committee members of my thesis for their insightful comments and constructive criticisms that help me improve the quality of the whole thesis.

I am really grateful to all of my fellow mates: Mr. Yamasaki, Mr. Sato, Mr. Hara, Mr. Osugi, Mr. Kuzuya and Mr. Uehara. You all made my experience in our lab more enjoyable.

Finally I would like to thank my family for their constant encouragement and support. Their love and care allowed me to overcome many challenges.

Kai Wang

June 2018